Politecnico di Torino

ThalesAlenia Space
a Thales / Leonardo company

POLITECNICO DI TORINO

Master Degree course in Aerospace Engineering - Aerogasdynamics

Master Degree Thesis

Optimization and Validation of a CFD Code for Hypersonic Regime Applications

Supervisors
Prof. Domenic D'Ambrosio
Ing. Vincenzo Mareschi

Candidate
Raffaele Vallese

Academic Year 2024-2025

Acknowledgements

I would like to extend my sincere gratitude to my thesis supervisor, Prof. Domenic D'Ambrosio, and to my company tutor at Thales Alenia Space - Italia, Ing. Vincenzo Mareschi, for their invaluable mentorship throughout this project.

Working under their supervision has been a defining experience in my academic path. I am deeply indebted to Prof. D'Ambrosio for his scientific rigor and for teaching me how to approach complex fluid dynamic problems with method and critical thinking. His guidance was essential in navigating the theoretical challenges of this work and in ensuring the robustness of the results presented.

Equally, I am grateful to Ing. Mareschi for his constant support and for sharing his extensive technical knowledge. His insight into the practicalities of CFD development and his ability to troubleshoot the most intricate coding issues were instrumental in bringing this project to completion.

Beyond their technical guidance, what I value most is the example they have set. Having had the opportunity to work on the code they helped shape, I have gained a profound appreciation for the ingenuity required to build such tools. It is my sincere hope that, through experience and dedication, I may one day achieve a similar level of mastery and capability to develop advanced computational solvers from scratch, following in their footsteps.

Thank you both for your trust, your patience, and for inspiring me to aim for excellence.

Abstract

This thesis presents the optimization and development of a proprietary Computational Fluid Dynamics (CFD) code for hypersonic flow applications, carried out in collaboration with Thales Alenia Space - Italia.

The initial phase of the work focused on restoring and modernizing the existing FORTRAN code to ensure full functionality for both two-dimensional and three-dimensional geometries.

The solver was then parallelized using Windows MPI to enhance computational efficiency and scalability across multiple processors.

The final stage involved the validation of the code through simulations of benchmark hypersonic configurations, representative of typical experimental and numerical test cases available in literature. Particular attention was devoted to assessing the influence and accuracy of the implemented physical models, including those governing high-temperature effects and shock interactions. The outcomes demonstrate the robustness and reliability of the developed CFD tool, providing a solid foundation for future hypersonic aerothermodynamics research and industrial applications.

Contents

List of Figures

List of Tables

Chapter 1

Introduction

The human aspiration to fly faster and higher has been a driving force in aerospace engineering since the early days of aviation. The Wright Brothers' first powered flight (1.1) in 1903 achieved speeds of approximately 35 mph at sea level, marking the beginning of an exponential growth trajectory in both velocity and altitude capabilities [4]. This relentless pursuit of higher speeds has defined the evolution of aeronautical technology throughout the twentieth and twenty-first centuries.

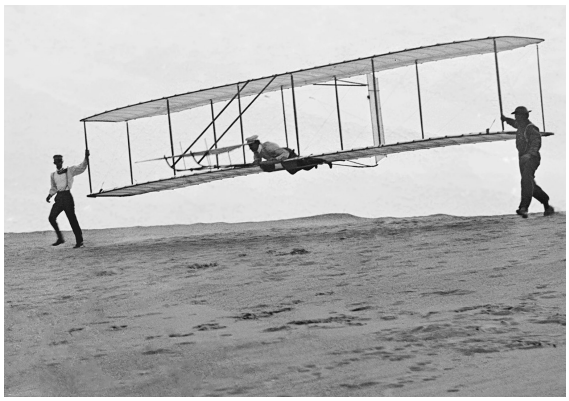

Figure 1.1. Wright Flyer, 1903[11].

The term "hypersonic" entered the aerospace lexicon as a distinct classification when practical applications demanded a departure from traditional supersonic design philosophies. While supersonic flight, defined by Mach numbers greater than unity, had been extensively studied and implemented in military aircraft such as the Lockheed F-104, the emergence of even higher speeds presented fundamentally different aerodynamic challenges[4].

The first human-made object to achieve hypersonic flight was the two-stage Bumper rocket (1.2), consisting of a V-2 first stage with a WAC Corporal second stage. On February 24, 1949, at White Sands Proving Ground in New Mexico, this vehicle reached a velocity of approximately 5,150 mph, roughly Mach 6.7, marking the inaugural achievement of hypersonic flight [4].

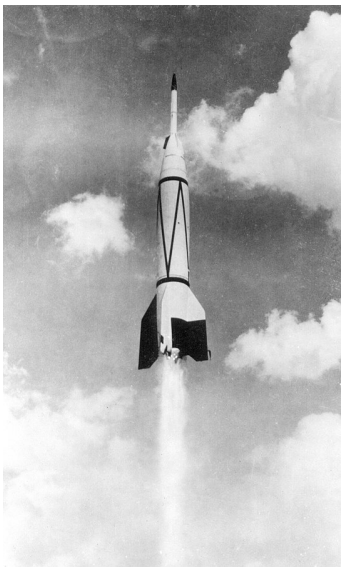

Figure 1.2. RTV-G-4 Bumper, 1949[40].

Following this initial milestone, the ensuing decades witnessed rapid development in hypersonic technology. In 1961, a pivotal year for manned spaceflight, Yuri Gagarin (1.3) became the first human to experience hypersonic flight during his orbital mission aboard Vostok I, re-entering Earth's atmosphere at speeds exceeding Mach 25[4].

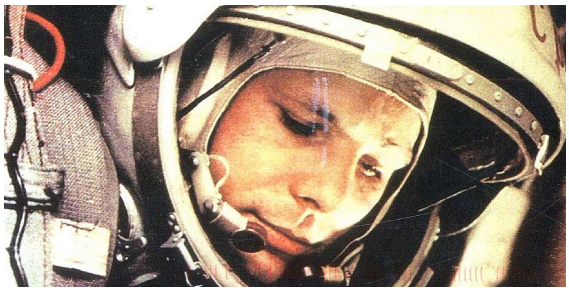

Figure 1.3. Yuri Gagarin before the Vostok I launch, 1961[38].

In 1962 test pilot Robert White flew the experimental X-15 (1.4) research aircraft at Mach 5.3, achieving the first hypersonic flight in a manned, powered aircraft [4]. These events not only demonstrated technical capability but also revealed that hypersonic aerodynamics fundamentally differed from the supersonic regime.

The motivation for studying hypersonic flows extends beyond historical achievement. The space race of the 1960s and 1970s necessitated the development of vehicles capable of returning from orbit at velocities exceeding Mach 20 and beyond.

The Apollo (1.5) command and service modules, designed to return astronauts from the Moon, entered Earth's atmosphere at the extreme hypersonic speed of Mach 36,

Figure 1.4. North American X-15[42].

representing a pinnacle of human spaceflight thermal engineering challenges [4]. These missions employed single-use ablative thermal protection systems that dissipated heat by charring and ablating away during reentry, a design philosophy consistent with the non-reusable nature of Apollo capsules.

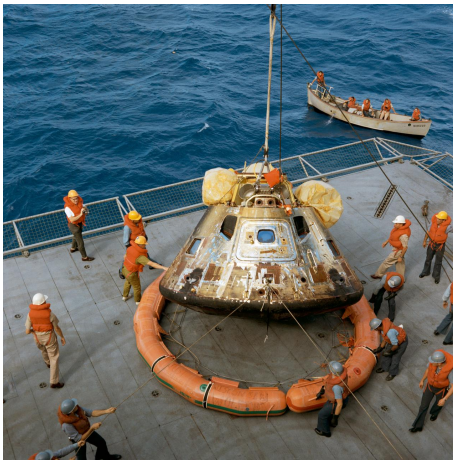

Figure 1.5. Apollo 11 Command Module being lowered to the deck of the U.S.S. Hornet[39].

The subsequent development of the Space Shuttle (1.6) represented a paradigm shift in hypersonic vehicle design: it was conceived as the world's first reusable spacecraft, demanding innovations in thermal protection technology [4]. Rather than employing ablative shields, NASA engineers developed an advanced reusable thermal protection system consisting of high-purity silica fiber-based ceramic tiles designed for repeated use, establishing new paradigms for spacecraft design and demonstrating that hypersonic vehicles could be engineered for repeated use rather than single-mission expendability [4].

Modern applications continue to drive research in hypersonics, including the development of hypersonic cruise vehicles, hypersonic missiles, and sustained atmospheric flight

Figure 1.6. Space Shuttle Discovery landing after its first mission[41].

systems such as the NASA X-43A experimental scramjet-powered vehicle, which demonstrated hypersonic cruise flight capabilities in the early 2000s [4]. Contemporary reentry technology has evolved significantly with the introduction of advanced reentry vehicles that combine aerothermodynamic efficiency with sophisticated thermal management systems.

The Intermediate eXperimental Vehicle (IXV)(1.7), developed by Thales Alenia Space under the auspices of the ESA, represents a modern approach to hypersonic reentry technology. The IXV served as a technology demonstrator for lifting-body reentry concepts, featuring advanced thermal protection systems and aerodynamic design optimized for controlled hypersonic flight and precision landing capabilities. Such developments reflect the modern paradigm where hypersonic reentry vehicles are engineered to maximize payload recovery, minimize thermal protection system mass through improved design, and enable sophisticated guidance and control during the extreme conditions of atmospheric reentry[1].

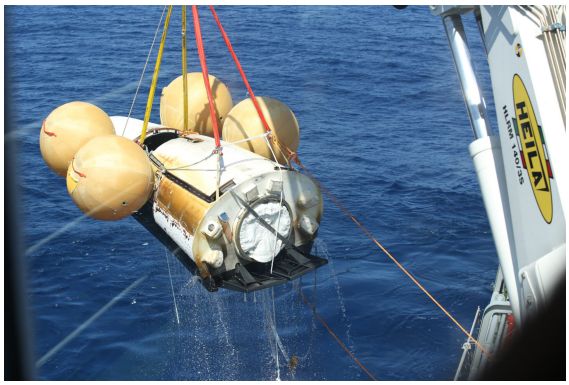

Figure 1.7. Recovery of IXV[18].

Understanding hypersonic flows is therefore not merely an academic exercise; it remains a critical frontier in aerospace engineering, with implications for national defense,

space exploration, and future transportation systems. The physical phenomena that characterize hypersonic flight are sufficiently distinct from those of lower-speed regimes that they warrant dedicated theoretical treatment and experimental investigation.

1.1 Definition and Boundary of the Hypersonic Regime

The Mach number, denoted as M, is a dimensionless quantity defined as the ratio of the flow velocity V to the local speed of sound a.

$$\mathrm{M} = \frac{V}{a}$$

It serves as a fundamental parameter in compressible flow that determines the flow regime around a body. Aerodynamic behavior changes significantly across different Mach number ranges:

- **Subsonic regime:** $M < 0.8$. Flow velocities are less than the speed of sound.
- **Transonic regime:** $0.8 < M < 1.2$. Complex flow phenomena appear with coexistence of subsonic and supersonic flows; shock waves start to form.
- **Supersonic regime:** $1.2 < M < 5$. The entire flow field moves faster than sound; shock waves are present, but thermal and chemical effects are limited.
- **Hypersonic regime:** $M \geq 5$. This range is conventionally accepted as the onset of hypersonic flow, characterized by extremely strong shock waves, high temperature effects, aerodynamic heating, and often chemical reactions in the flowfield [4].

The definition of hypersonic flight presents an interesting challenge in aerodynamics, as the transition from supersonic to hypersonic behavior is not sharply demarcated by a single Mach number M. However, a practical threshold of Mach 5 has been conventionally adopted as the beginning of the hypersonic regime [4]. This classification is not arbitrary; rather, it reflects the emergence of unique physical phenomena that become increasingly pronounced as the Mach number increases beyond this value.

The hypersonic regime is more precisely characterized by the physical phenomena that dominate the flow rather than by a specific numerical threshold. As defined by Anderson, "hypersonics is the study of flight at speeds where aerodynamic heating dominates the physics of the problem" [4]. This definition captures the essential distinction: at hypersonic speeds, the kinetic energy of the incoming freestream air becomes sufficiently large that when the flow is decelerated near the vehicle surface, this kinetic energy is transformed into internal energy, resulting in extremely high temperatures. These elevated temperatures produce phenomena such as molecular dissociation, vibrational excitation, ionization, and chemical reactions that fundamentally alter the thermodynamic and aerodynamic characteristics of the flow [4].

Furthermore, at very high altitudes, where the number density of molecules becomes low, the continuum assumption underlying traditional fluid mechanics begins to fail. This

leads to the low-density flow regime, in which kinetic theory must replace the classical continuum approach.

The Knudsen number Kn, defined as the ratio of the mean free path λ to a characteristic length scale of the body L, plays a crucial role in demarcating the continuum flow regime.

$$\mathrm{Kn} = \frac{\lambda}{L}$$

While low-density effects become increasingly important at hypersonic speeds, particularly for vehicles operating at high altitudes, the present discussion focuses primarily on the continuum regime where classical fluid mechanics remains valid.

1.2 Characteristic Phenomena of Hypersonic Flows

Hypersonic flows exhibit several distinctive characteristics that set them apart from their supersonic counterparts. These phenomena are intimately related to the physical mechanisms that govern flow behavior at extremely high Mach numbers, and understanding them is essential for the analysis and design of hypersonic vehicles.

1.2.1 Thin Shock Layers

One of the most distinctive features of hypersonic flow is the formation of thin shock layers. As the Mach number increases, oblique shock theory predicts that the shock wave angle decreases, approaching the flow deflection angle asymptotically. This means that the shock wave becomes increasingly aligned with the body surface. Consequently, the region between the shock wave and the body surface, termed the shock layer, becomes progressively thinner as the Mach number increases [4]

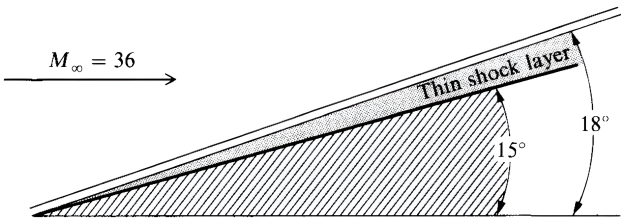

Figure 1.8. Example of hypersonic thin shock layer.[4].

The physical implication of this thinning is profound. The density increase across the shock wave results in extremely high mass fluxes being squeezed through correspondingly small flow areas. This compression creates regions of high pressure immediately downstream of the shock and introduces complex flow interactions. Moreover, since the shock layer thickness becomes comparable to or even smaller than the viscous boundary layer thickness, the shock and boundary layer are no longer independent features but instead become tightly coupled. This shock-boundary layer interaction constitutes one of the

most complex aspects of hypersonic flow analysis and directly influences aerodynamic forces, heat transfer rates, and flow separation characteristics [4].

1.2.2 Entropy Layers and Vorticity Generation

A second characteristic phenomenon unique to hypersonic flows is the formation of entropy layers. In contrast to isentropic flow, the process of crossing a curved shock wave is inherently non-isentropic. The entropy change across a shock depends on the shock's strength, which varies along its length for curved geometries. At the nose of a blunt body, where the bow shock is highly curved, stronger portions of the shock produce larger entropy increases than weaker portions. This spatial variation in entropy rise creates an entropy layer: a region of concentrated entropy gradients that extends downstream from the shock and persists along the body surface [4].

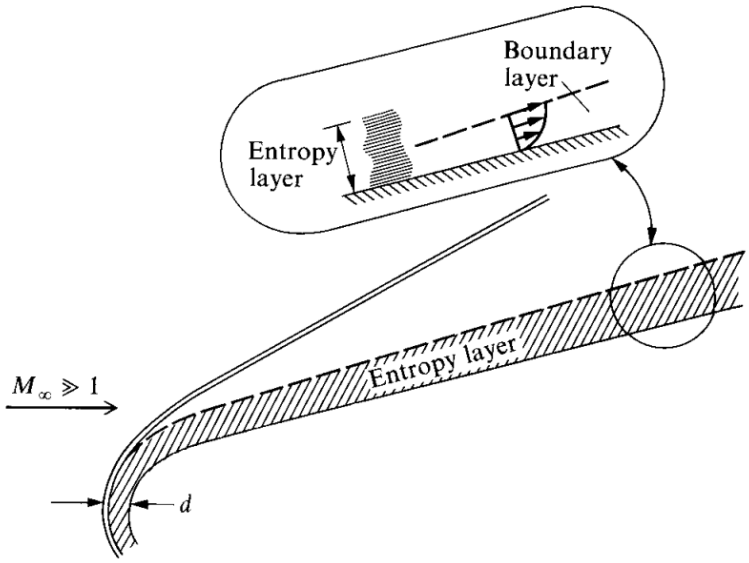

Figure 1.9. Entropy layer [4].

By Crocco's theorem (1.1), entropy gradients are inextricably linked to vorticity generation. The terms in Eq. 1.1 are:

- T: temperature,
- s: entropy,
- $\mathbf{v}$: velocity vector,
- h_0: stagnation enthalpy.

$$T\nabla s = \frac{\partial \mathbf{v}}{\partial t} - \nabla h_0 - \mathbf{v} \times (\nabla \times \mathbf{v}) \tag{1.1}$$

Therefore, entropy layers give rise to significant regions of vorticity in an otherwise inviscid flow. At higher Mach numbers, the entropy gradients become steeper and more pronounced, leading to increased vorticity magnitudes. This vorticity interacts with the viscous boundary layer through a process known as vorticity interaction, complicating the prediction of boundary layer properties and creating additional challenges in the analysis of viscous effects [4].

1.2.3 Viscous Interaction Effects

Hypersonic flows are characterized by a complex interplay between inviscid and viscous regions, a phenomenon referred to as viscous interaction. The viscous interaction in hypersonic flows differs fundamentally from that observed at lower Mach numbers. As the boundary layer develops along a surface, it displaces the inviscid flow, effectively "thickening" the body shape seen by the external flow. This displacement causes a reorganization of the shock wave structure and produces pressure gradients that profoundly influence the boundary layer development itself.

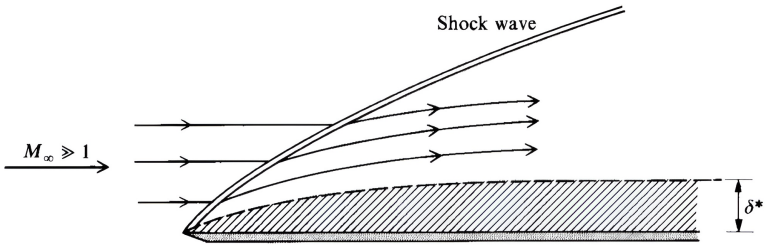

Figure 1.10. Hypersonic flow on a flat plate [4].

The mutual influence between the shock wave and the boundary layer creates strong viscous interactions characterized by significant pressure gradients and flow separation phenomena. In some cases, the interaction becomes strong enough to induce shock detachment or shock-induced separation, fundamentally altering the aerodynamic characteristics of the vehicle [4].

1.2.4 High-Temperature Effects and Thermochemical Phenomena

The extreme temperatures generated by compression and deceleration of the freestream air at hypersonic speeds introduce thermochemical effects that are absent or negligible in lower speed flows. As the temperature rises, molecular degrees of freedom become increasingly excited, beginning with vibrational modes and progressing to molecular dissociation and ionization of the constituent atoms.

In air at hypersonic speeds, oxygen and nitrogen molecules dissociate into atomic species, beginning at temperatures around 2,000 K and becoming increasingly significant at temperatures above 4,000 K [4]. At even higher temperatures, recombination reactions and ionization become important.

These chemical processes are far from instantaneous; the rate at which chemical species transform depends on molecular collision frequencies, local temperature, and pressure. Regions of the flow may therefore exist in chemical non-equilibrium, wherein the composition does not reflect the equilibrium composition that would prevail if sufficient time had elapsed for all reactions to reach completion [4].

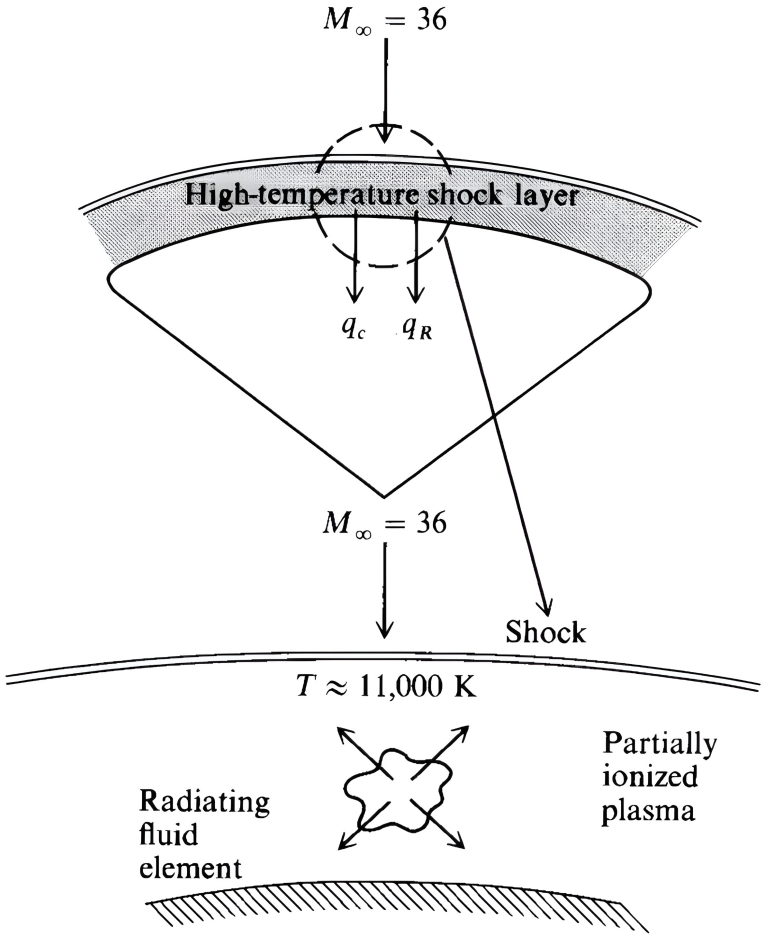

Figure 1.11. High-temperature shock layer [4].

These high-temperature effects have profound implications for aerodynamic heating, vehicle material selection, and the overall design philosophy for hypersonic vehicles. The intense heating at the stagnation point and along shock-attached surfaces necessitates advanced thermal protection systems or active cooling mechanisms.

1.2.5 Boundary Layer Characteristics

Hypersonic boundary layers exhibit distinct characteristics that differentiate them from their subsonic and supersonic counterparts. One notable feature is the relatively extended region of laminar flow that persists at hypersonic speeds. Whereas transition from laminar

to turbulent flow typically occurs at Reynolds numbers around 5×10^5 in incompressible flow over a flat plate, transition Reynolds numbers at hypersonic speeds can reach values on the order of 10^8 or higher [4]. This dramatic increase in transition Reynolds number, driven by increased viscous damping at high Mach numbers and compressibility effects, provides a significant practical advantage, as laminar flows generate considerably lower skin friction and heat transfer rates than their turbulent counterparts.

Additionally, the hypersonic boundary layer displays increased thickness relative to lower-speed conditions, particularly when strong adverse pressure gradients induce separation. The high temperatures within the hypersonic shock layer also increase the viscosity coefficient through power-law relationships, further thickening the boundary layer. The boundary layer thickening can become sufficiently pronounced that the boundary layer merges with the thin shock layer, creating the aforementioned shock-boundary layer interaction phenomenon [4].

1.3 Vehicle Design and Aerodynamic Analysis

The distinctive characteristics of hypersonic flows necessitate design approaches that differ substantially from those employed for supersonic vehicles. Whereas supersonic aircraft typically feature sharp noses, thin wings, and slender fuselages to minimize wave drag, hypersonic vehicles often employ blunt shapes to manage aerodynamic heating, broad delta wings to provide pressure-based lift, and integrated airframe-propulsion configurations wherein the vehicle itself functions as part of the propulsion system.

Modern hypersonic vehicle concepts, such as scramjet-powered aerospace planes and hypersonic cruise missiles, exemplify this integrated approach. In these designs, the sharp-edged, slender configuration of a traditional supersonic aircraft would prove inadequate or even dangerous. Instead, designers leverage the unique characteristics of hypersonic flow, particularly the thin shock layer and shock-attached pressure field, to achieve efficient lift generation while managing thermal and structural constraints.

Furthermore, the complex phenomena characterizing hypersonic flows necessitate sophisticated analysis techniques. Classical analytical methods, though still valuable for preliminary design, must be supplemented with computational fluid dynamics (CFD), and insights from fundamental theory are essential for interpreting results and making engineering decisions.

The present thesis addresses these considerations through detailed treatment of the governing equations, analysis methodologies, and physical phenomena that characterize hypersonic flow. Subsequent chapters will examine the fundamental fluid mechanics of inviscid and viscous hypersonic flows, the effects of high temperature and chemical reactions, and applications to vehicle design and analysis.

Chapter 2

Physical Model

The computational analysis of hypersonic aerothermodynamic flows requires a rigorous mathematical and physical foundation that bridges the fundamental phenomena occurring at different scales of the flowfield. This chapter establishes the theoretical framework upon which the numerical simulations of hypersonic vehicle configurations are constructed.

Hypersonic flight regimes are characterized by distinctive physical phenomena that emerge when the freestream Mach number significantly exceeds unity. Unlike supersonic flows, where compressibility effects are primarily governed by isentropic relations and shock dynamics, hypersonic flows exhibit additional layers of complexity arising from the interplay between shock waves, viscous effects, and high-temperature chemical processes. A comprehensive understanding of these coupled phenomena is essential for the development and validation of Computational Fluid Dynamics (CFD) solvers capable of accurately predicting aerothermodynamic loads on entry vehicles and propelled hypersonic systems.

The hierarchical approach adopted in this chapter progressively introduces the physical and mathematical models underlying CFD simulations. This structure reflects the fundamental decomposition of hypersonic flows into three complementary regimes, each introducing successive levels of physical complexity. The progression from inviscid to viscous to thermochemically reacting flows provides a logical framework that mirrors both the historical development of hypersonic aerodynamics theory and the practical implementation of modern CFD codes.

The first regime addressed is inviscid hypersonic aerodynamics, governed by the Euler equations. Within this framework, shock waves represent discontinuities in the flow properties, characterized by the Rankine-Hugoniot relations. In the hypersonic limit, these shock relations exhibit distinctive mathematical properties that simplify analysis while retaining physical accuracy for engineering applications. Phenomena such as entropy layer formation behind oblique shocks and the thin shock layer approximation become analytically tractable in this regime and provide insights that remain qualitatively valid when viscous effects are subsequently introduced.

The viscous regime extends the inviscid analysis by incorporating friction and thermal conduction through the full Navier-Stokes equations. In this domain, boundary layers become a dominant feature of the flowfield structure. For hypersonic vehicles, the high

Reynolds numbers characteristic of the flight trajectory justify the implementation of the boundary layer approximation, which reduces the computational dimensionality while capturing the essential mechanisms of skin friction and convective heat transfer. The interaction between the outer inviscid flow and the boundary layer, a phenomenon of critical importance, necessitates careful treatment of the pressure gradients and entropy effects that arise from shock-boundary layer interactions.

The third regime, high-temperature aerothermodynamics, introduces the complexities arising from chemical dissociation, ionization, and vibrational excitation of air molecules. At temperatures exceeded during planetary entry, the assumption of a chemically inert, calorically perfect gas becomes invalid. The internal energy is partitioned among multiple degrees of freedom (translational, rotational, vibrational, and electronic modes) each characterized by its own temperature scale and relaxation time. These effects dramatically alter the thermodynamic properties and transport coefficients of the working fluid, subsequently affecting the pressure distribution, heating rates, and aerodynamic forces on the vehicle.

The coupling of these three regimes defines the complete physical model required for hypersonic aerothermodynamic analysis. Each regime contributes distinct physical mechanisms that must be properly represented in the governing equations and boundary conditions. The CFD solver developed for this work must therefore be capable of simultaneously resolving:

- **Shock waves and expansion fans**, which govern the pressure distribution over the vehicle surface and generate the entropy layers that subsequently affect the boundary layer development;
- **Boundary layer development and viscous interaction effects**, which control skin friction and convective heat transfer and which can profoundly modify the pressure field in hypersonic regimes;
- **Chemical reactions and internal energy modes**, which influence both the thermodynamic properties and the transport coefficients, thereby affecting the temperature field and the energy fluxes at the vehicle surface.

The mathematical formulation of these physical processes requires a hierarchy of equations, starting from the conservation laws of mass, momentum, and energy, supplemented by thermodynamic constitutive relations and transport models. The following sections present this framework in a structured manner, beginning with the inviscid flow equations and progressively incorporating viscous and thermochemical effects.

It is important to note that while this chapter provides a comprehensive treatment of the physical models, it does not attempt to derive the governing equations from first principles. Instead, each equation set is presented directly, accompanied by a detailed explanation of each term's physical significance and its role within the CFD implementation. This approach is intentional: a CFD code must treat these equations as mathematical objects to be discretized and solved numerically, and the physical interpretation of each term guides the design of robust numerical algorithms and appropriate mesh resolution strategies.

The numerical solution techniques that discretize and solve these equations are the subject of subsequent chapters. However, a clear understanding of the physical processes encoded in these equations is prerequisite to the development of algorithms that accurately represent these processes at the finite grid resolution available in practical computations.

2.1 Inviscid Hypersonic Aerodynamics

The foundation of hypersonic aerothermodynamic analysis rests upon the governing equations for inviscid flows, where the effects of friction and thermal conduction are neglected. While this approximation is necessarily incomplete for predicting phenomena such as skin friction and convective heating, it provides an accurate estimate of the pressure distribution along a vehicle surface and captures the essential shock dynamics that characterize hypersonic flight regimes [4]. In this section, the Euler equations governing inviscid compressible flows are presented, followed by the fundamental shock relations and expansion processes that define hypersonic aerodynamics.

2.1.1 Governing Equations: Euler Equations

The motion of an inviscid compressible fluid is governed by the Euler equations, which express conservation of mass, momentum, and energy. These equations form the mathematical foundation upon which the design and operation of hypersonic CFD solvers rests [60].

Integral Form

In integral conservative form, the unsteady Euler equations for a fixed control volume Ω with surface $\partial\Omega$ are:

$$\frac{\partial}{\partial t}\int_{\Omega} \mathbf{W}\, d\Omega + \oint_{\partial\Omega} \mathbf{F}\cdot\mathbf{n}\, dS = 0 \tag{2.1}$$

where the conservative variable vector is:

$$\mathbf{W} = \begin{pmatrix} \rho \\ \rho u \\ \rho v \\ \rho w \\ E \end{pmatrix} \tag{2.2}$$

and the inviscid flux tensor is:

$$\mathbf{F} = \begin{pmatrix} \rho\mathbf{v} \\ p\mathbf{I} + \rho\mathbf{v}\mathbf{v}^T \\ (E+p)\mathbf{v} \end{pmatrix} \tag{2.3}$$

Here, ρ denotes the fluid density, $\mathbf{v} = (u, v, w)^T$ is the velocity vector, p is the static pressure, E is the total energy per unit volume, and $\mathbf{n}$ is the outward-pointing surface normal. The integral form directly reflects the physical principle of conservation: the rate of change of a conserved quantity within a control volume plus the net flux through the surface equals zero.

Differential Form

Expanding the integral form and applying the divergence theorem yields the differential conservation form of the Euler equations [9]:

$$\frac{\partial \rho}{\partial t} + \nabla \cdot (\rho \mathbf{v}) = 0 \tag{2.4}$$

$$\frac{\partial (\rho \mathbf{v})}{\partial t} + \nabla \cdot (\rho \mathbf{v}\mathbf{v}) + \nabla p = 0 \tag{2.5}$$

$$\frac{\partial E}{\partial t} + \nabla \cdot [(E + p)\mathbf{v}] = 0 \tag{2.6}$$

Equation (2.4) represents **mass conservation**: the local time rate of change of density plus the divergence of the mass flux equals zero. Equation (2.5) expresses **momentum conservation** in vector form. Equation (2.6) is the **energy balance**: the total energy (kinetic plus internal) evolves as the flow does work against pressure forces and transports enthalpy.

Thermodynamic Closure

The Euler equations contain more unknowns (ρ, u, v, w, p, e_{int}) than equations. To close the system, a thermodynamic relation connecting pressure to density and internal energy is required. For an ideal gas:

$$p = (\gamma - 1)\rho e_{\text{int}} \tag{2.7}$$

where $\gamma = c_p/c_v$ is the specific heat ratio. For diatomic gases such as O_2 and N_2 in air at moderate temperatures, $\gamma \approx 1.4$. The total energy per unit volume is related to internal energy and kinetic energy through:

$$E = \rho e_{\text{int}} + \frac{1}{2}\rho(\mathbf{v} \cdot \mathbf{v}) \tag{2.8}$$

These relations allow the pressure to be computed from the conservative variables, thereby closing the system of equations for solution by CFD methods.

2.1.2 Shock Wave Relations

Shock waves are discontinuities in the flow field where the governing equations transition from one continuous solution on one side to a different continuous solution on the other. While shock waves involve thin regions where viscous effects are present, their thickness is typically of order 10^{-6} m for air at atmospheric conditions and is negligible compared to vehicle dimensions. The shock can therefore be treated as a mathematical discontinuity satisfying the Rankine-Hugoniot conditions [4, 50, 27].

Normal Shock Relations

For a normal shock wave perpendicular to the flow direction, the Rankine-Hugoniot relations relate properties downstream of the shock (subscript 2) to those upstream (subscript 1) [9]:

$$\rho_1 V_1 = \rho_2 V_2 \tag{2.9}$$

$$p_1 + \rho_1 V_1^2 = p_2 + \rho_2 V_2^2 \tag{2.10}$$

$$h_1 + \frac{V_1^2}{2} = h_2 + \frac{V_2^2}{2} \tag{2.11}$$

where V denotes the velocity perpendicular to the shock and $h = e_{\text{int}} + p/\rho$ is the specific enthalpy. For an ideal gas with constant specific heats, these relations yield dimensionless ratios of density, pressure, temperature, and Mach number across the shock.

In the hypersonic limit where $M_1 \gg 1$, the normal shock relations between pre and post-shock variables simplify dramatically:

$$\frac{\rho_2}{\rho_1} = \frac{V_1}{V_2} = \frac{(\gamma+1)M_1^2}{(\gamma-1)M_1^2+2} \to \frac{\gamma+1}{\gamma-1} \tag{2.12}$$

$$M_2^2 = \frac{(\gamma-1)M_1^2+2}{2\gamma M_1^2-\gamma+1} \to \frac{\gamma-1}{2\gamma} \tag{2.13}$$

$$c_{p_2} = \frac{4(M_1^2-1)}{(\gamma+1)M_1^2} \to \frac{4}{\gamma+1} \tag{2.14}$$

$$\frac{p_2}{p_1} = \frac{2\gamma M_1^2-(\gamma-1)}{\gamma+1} \to \frac{2\gamma}{\gamma+1}M_1^2 \tag{2.15}$$

$$\frac{s_2-s_1}{c_v} \to \log\left[\frac{2}{\gamma+1}M_1^2\right] \tag{2.16}$$

For air with $\gamma = 1.4$, Equation (2.12) gives $\rho_2/\rho_1 \approx 6$. The Mach number behind the shock approaches zero, the velocity approaches zero, and the pressure ratio becomes proportional to M_1^2.

Oblique Shock Relations

When a shock wave is inclined to the flow direction, the shock angle β and deflection angle δ are related through the oblique shock relations. For small deflection angles and large Mach numbers characteristic of hypersonic flows, the shock becomes nearly parallel to the flow (weak shock), and the oblique shock relations relate the normal Mach number to the post-shock conditions [9].

Relations are mostly the same as for normal shocks, but applied to the normal component of the Mach number.

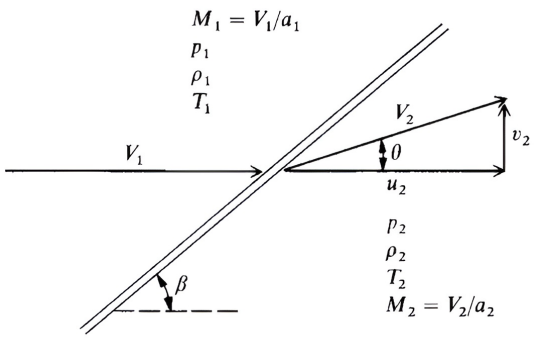

Figure 2.1. Oblique shock geometry [4].

There's a difference for the pressure coefficient behind an oblique shock, that is given by:

$$c_{p_2} \to \frac{4\sin^2\beta}{\gamma+1} \tag{2.17}$$

where β is the shock angle.

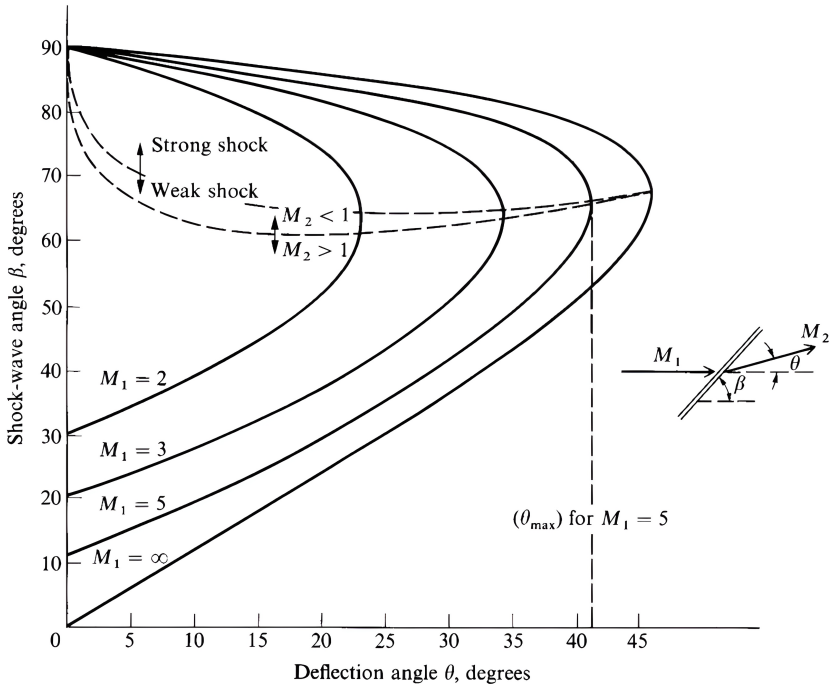

Figure 2.2. $\theta - \beta - M$ diagram [4].

Shock-Expansion Theory

The **shock-expansion theory** provides a practical framework for computing pressure distributions on hypersonic vehicle surfaces. The theory asserts that the flow over a body surface experiencing a deflection δ can be represented as [4]:

1. A shock wave with deflection angle δ for convex surface deflections (compression);
2. A Prandtl-Meyer expansion fan with deflection angle δ for concave surface deflections (expansion).

The oblique shock relations applied to the incident freestream flow provide the post-shock conditions downstream of a compression surface, while isentropic relations applied to the external flow provide the conditions downstream of an expansion surface. This method remains the foundation of preliminary design calculations for hypersonic vehicles.

2.1.3 Hypersonic Similarity and Mach Number Independence

A fundamental principle in hypersonic aerodynamics is the **Mach number independence principle**, formulated by Oswatitsch [43]. This principle states that for sufficiently large Mach numbers, certain nondimensional flow properties become independent of the freestream Mach number [4, 9].

Mathematically, if the freestream density ρ_∞ and velocity V_∞ are held fixed, and the characteristic Mach number $M_\infty \to \infty$ (which requires $a_\infty \to 0$), then the flow field structure, including shock shapes and streamline patterns, becomes independent of M_∞. In this limit:

- Shock wave shapes become independent of M_∞;
- Streamline patterns become independent of M_∞;
- Pressure coefficient distributions become independent of M_∞;
- Mach line orientations approach limiting values.

This principle has profound implications for hypersonic vehicle design: at sufficiently high Mach numbers, pressure-based aerodynamic coefficients depend primarily on body geometry and freestream flow direction, not on the magnitude of the Mach number itself. For practical hypersonic vehicles, Mach numbers exceeding $M \approx 5$ often lie in a regime where this principle provides accurate predictions[4].

2.1.4 Bow Shock Structure and the Thin Shock Layer Approximation

The flow about a blunt-nosed hypersonic vehicle exhibits a distinctive feature: a detached curved bow shock with a subsonic pocket immediately behind it [9]. This configuration arises because the normal component of the Mach number normal to the shock exceeds unity almost everywhere, causing the post-shock flow to be subsonic except in the oblique shock portion far from the nose where $M_n \approx 1$.

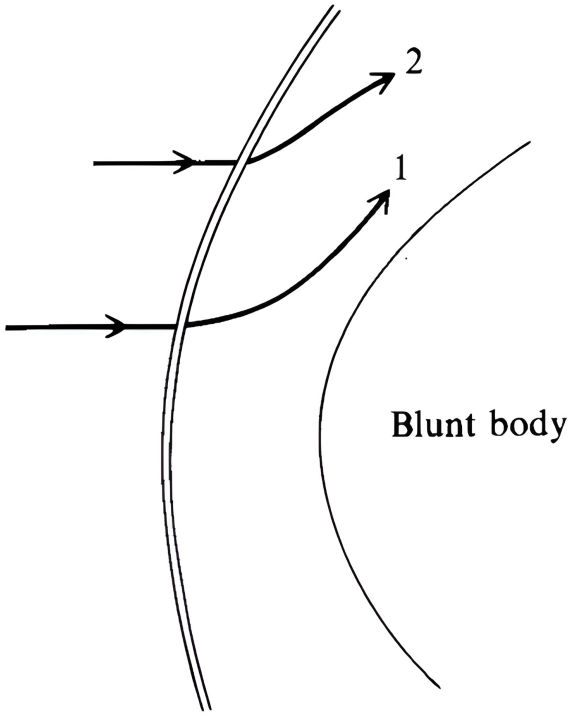

Figure 2.3. Bow shock structure around a blunt body [4].

For a perfect gas undergoing a normal shock, the post-shock Mach number $M_2 < 1$ for any upstream Mach number $M_1 > 1$. Therefore, a region of subsonic flow exists immediately downstream of the shock near the nose, bounded by a sonic line that separates the subsonic nose region from the supersonic flow further downstream.

The **thin shock layer** approximation exploits the observation that the shock thickness is negligible compared to vehicle dimensions. Within the shock layer bounded by the body surface and the shock wave, the normal pressure gradient is negligible and pressure remains approximately constant, while the flow direction changes discontinuously across the shock [4, 9]. This approximation significantly simplifies the analysis of the flow field within the shock layer and has been validated extensively through comparisons with detailed analyses.

2.1.5 Boundary Conditions for Inviscid Flows

Specification of boundary conditions at the domain boundaries is essential for proper CFD formulation. For inviscid flows over hypersonic vehicles, the typical boundary conditions are [9]:

- **Wall boundary condition:** the velocity component normal to the wall surface must be zero, $\mathbf{v} \cdot \mathbf{n} = 0$. This enforces impermeability of the solid surface.
- **Far-field (inflow) boundary:** when shock-capturing is employed, the freestream

conditions are applied far upstream. When shock-fitting is used, the post-shock conditions from oblique shock relations are prescribed at the shock-aligned outer boundary.

- **Outflow boundary:** if the computational domain extends to a region where flow is everywhere supersonic, standard supersonic outflow conditions are applied.
- **Symmetry boundary:** when the vehicle geometry and angle of attack permit, symmetry planes can be exploited to reduce computational cost.

These boundary conditions, combined with the conservation equations and thermodynamic relations, define a well-posed initial boundary value problem suitable for numerical solution.

2.2 Viscous Hypersonic Aerodynamics

The inviscid analysis presented in Section 2.1, while providing a first-order estimate of pressure distributions and shock structures, is fundamentally incomplete for practical hypersonic vehicle design. Two critical phenomena absent from inviscid theory, skin friction and convective heat transfer, dominate the structural design of hypersonic vehicles and determine thermal protection system requirements [9]. These effects arise from the interaction between the bulk hypersonic flow and the thin boundary layer adjoining the vehicle surface, where viscous stresses and thermal conduction become dominant [4, 64]. This section formulates the governing equations for viscous hypersonic flows and develops the asymptotic approximations that render practical analysis feasible at high Reynolds numbers.

2.2.1 Navier-Stokes Equations for Compressible Viscous Flows

The full set of governing equations for a viscous, compressible, thermally conducting fluid is the system of Navier-Stokes equations, which augment the Euler equations by including the effects of viscous stress and thermal diffusion [9]. In integral form for a control volume Ω with surface $\partial\Omega$:

$$\frac{\partial}{\partial t}\int_{\Omega} \mathbf{W}\, d\Omega + \oint_{\partial\Omega} (\mathbf{F}_{\text{conv}} + \mathbf{F}_{\text{visc}}) \cdot \mathbf{n}\, dS = 0 \tag{2.18}$$

where $\mathbf{F}_{\text{conv}}$ is the convective (inviscid) flux from Equation (2.3), and $\mathbf{F}_{\text{visc}}$ is the viscous flux:

$$\mathbf{F}_{\text{visc}} = \begin{pmatrix} 0 \\ \boldsymbol{\tau} \\ \boldsymbol{\tau} \cdot \mathbf{v} + \mathbf{q} \end{pmatrix} \tag{2.19}$$

Here, $\boldsymbol{\tau}$ is the viscous stress tensor and $\mathbf{q}$ is the heat flux vector. Applying the divergence theorem yields the differential form [9]:

$$\frac{\partial \rho}{\partial t} + \nabla \cdot (\rho \mathbf{v}) = 0 \tag{2.20}$$

$$\frac{\partial (\rho \mathbf{v})}{\partial t} + \nabla \cdot (\rho \mathbf{v}\mathbf{v}) + \nabla p = \nabla \cdot \boldsymbol{\tau} \tag{2.21}$$

$$\frac{\partial E}{\partial t} + \nabla \cdot [(E + p)\mathbf{v}] = \nabla \cdot (\boldsymbol{\tau} \cdot \mathbf{v}) + \nabla \cdot \mathbf{q} \tag{2.22}$$

The viscous stress tensor for a Newtonian fluid, employing the Stokes hypothesis (which sets the bulk viscosity to zero), is [4, 9]:

$$\boldsymbol{\tau} = \mu \left[\nabla \mathbf{v} + (\nabla \mathbf{v})^T - \frac{2}{3}(\nabla \cdot \mathbf{v})\mathbf{I} \right] \tag{2.23}$$

where μ is the dynamic viscosity. The heat flux is given by Fourier's law:

$$\mathbf{q} = -k\nabla T \tag{2.24}$$

where k is the thermal conductivity. The closure is provided by the ideal gas law and thermodynamic relations as in Section 2.1.1.

The physical interpretation of Equations (2.20)–(2.22) reflects the balance of momentum and energy including dissipative processes. The stress tensor term $\nabla \cdot \boldsymbol{\tau}$ in Equation (2.21) represents the divergence of viscous forces, while the energy equation includes both viscous dissipation ($\boldsymbol{\tau} \cdot \mathbf{v}$) and thermal conduction ($\mathbf{q}$). These terms are negligible in thin shock layers but become increasingly important as one approaches the vehicle surface where velocity gradients are extreme.

2.2.2 The Boundary Layer Concept and Approximations

At high Reynolds numbers characteristic of hypersonic flight, viscous effects are confined to a thin region adjacent to solid surfaces, the **boundary layer**, where velocity changes from zero at the wall to the external flow value over a distance $\delta \ll L$, where L is a characteristic body dimension. This fundamental insight, introduced by Prandtl in 1904 [49], allows dimensional analysis of the Navier-Stokes equations to yield reduced equations valid within this thin layer [9, 64].

For a hypersonic flow with freestream Mach number M_∞, unit Reynolds number $\mathrm{Re}_u = \frac{\rho_\infty a_\infty}{\mu_\infty}$, and characteristic length L, the Reynolds number is $\mathrm{Re}_L = \frac{\rho_\infty V_\infty L}{\mu_\infty}$. The boundary layer thickness scales as:

$$\frac{\delta}{L} \sim \frac{1}{\sqrt{\mathrm{Re}_L}} \tag{2.25}$$

Within the boundary layer, stretched coordinates $\eta = \frac{y}{\delta(x)}$ reveal order-of-magnitude relationships. Specifically, if $u \sim V_\infty$ (order unity in normalized form), $x \sim L$ (order unity), and $y \sim \delta$ (order δ), then from mass conservation, $v \sim \frac{V_\infty \delta}{L}$ (order δ) [9].

Substituting these scalings into the momentum equation and requiring that viscous terms remain at order unity yields the constraint:

$$\mathrm{Re}_L = O\left(\frac{1}{\delta^2}\right) \tag{2.26}$$

Under this constraint, the normal pressure gradient $\frac{\partial p}{\partial y}$ becomes negligible compared to the streamwise gradient, yielding:

$$\frac{\partial p}{\partial y} \approx 0 \tag{2.27}$$

This critical result permits the use of external inviscid pressure distributions within boundary layer calculations.

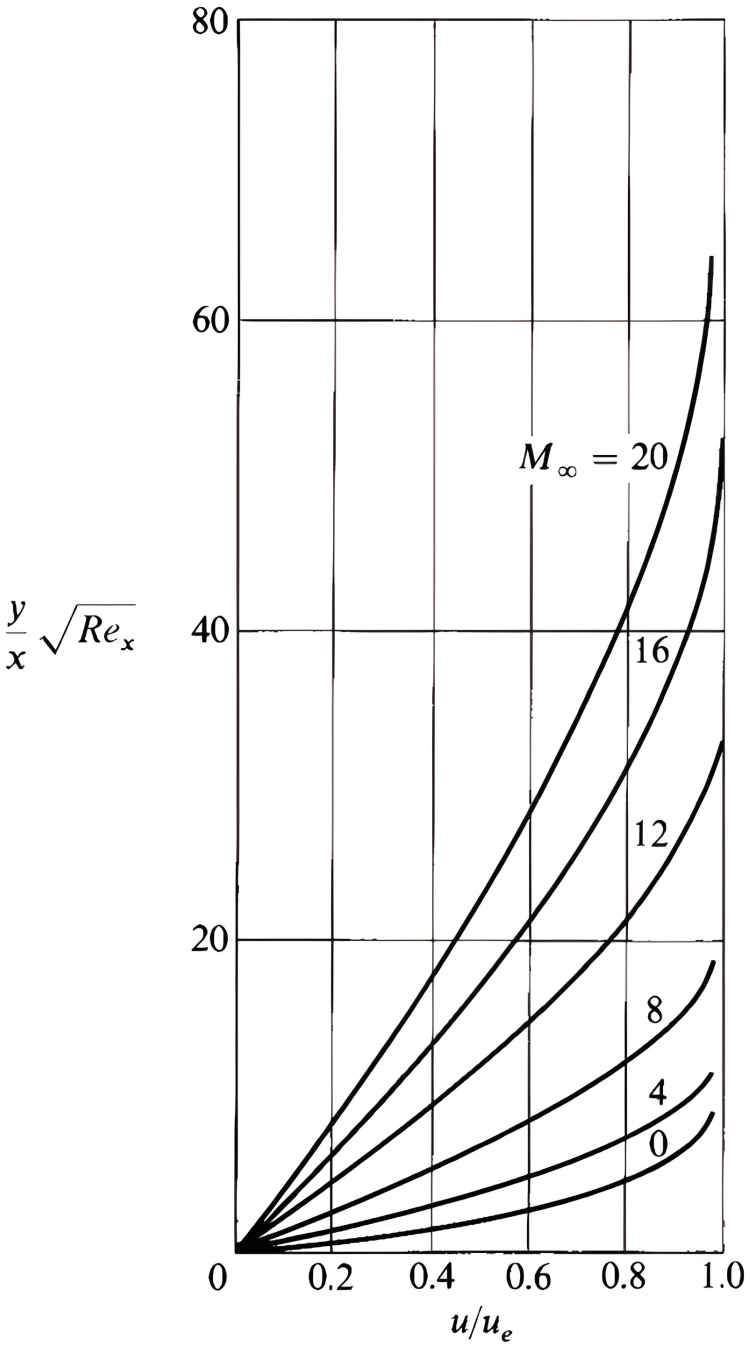

Figure 2.4. Velocity profiles in a compressible laminar boundary layer over a flat plate [4].

2.2.3 Compressible Boundary Layer Equations

The reduced Navier-Stokes equations valid within the boundary layer for steady, two-dimensional flow are [9, 64]:

$$\frac{\partial(\rho u)}{\partial x} + \frac{\partial(\rho v)}{\partial y} = 0 \tag{2.28}$$

$$\rho u \frac{\partial u}{\partial x} + \rho v \frac{\partial u}{\partial y} = -\frac{dp_e}{dx} + \frac{\partial}{\partial y}\left(\mu \frac{\partial u}{\partial y}\right) \tag{2.29}$$

$$\rho u \frac{\partial h}{\partial x} + \rho v \frac{\partial h}{\partial y} = \frac{\partial}{\partial y}\left(k \frac{\partial T}{\partial y}\right) + \mu \left(\frac{\partial u}{\partial y}\right)^2 \tag{2.30}$$

where h is specific enthalpy and $p_e(x)$ is the external pressure prescribed by the inviscid flow solution. Equation (2.29) reveals that the streamwise pressure gradient, which drives adverse or favorable conditions for boundary layer development, comes from the external inviscid analysis. The last term in Equation (2.30) represents viscous dissipation, which becomes significant at high Mach numbers.

Boundary layer analysis requires conditions at both the wall surface and at the boundary layer edge [9]:

Wall Boundary ($y = 0$)

$$u = 0, \quad v = 0 \quad \text{(no-slip condition)} \tag{2.31}$$

Temperature at the wall is specified as either:

$$T = T_w \qquad \text{or} \qquad -k\left(\frac{\partial T}{\partial y}\right)_w = q_w \tag{2.32}$$

Boundary Layer Edge ($y = \delta$)

$$u \to u_e(x), \quad T \to T_e(x) \tag{2.33}$$

where subscript e denotes external inviscid flow values obtained from the external pressure distribution [9].

2.2.4 Transport Properties in Compressible Flows

The viscosity $\mu(T)$ and thermal conductivity $k(T)$ are strong functions of temperature in hypersonic flows. For air at moderate temperatures (below ≈ 1000 K where dissociation is negligible), classical kinetic theory predicts viscosity according to Chapman-Enskog theory [7]:

$$\mu = \frac{f(T)\sqrt{m_{\text{mol}} k_B T}}{\sigma^2} \tag{2.34}$$

where m_{mol} is molecular mass, k_B is Boltzmann's constant, σ is collision diameter, and $f(T)$ is a temperature-dependent collision integral. Practical approximations include the Sutherland law, historically formulated by Sutherland in 1893 [58]:

$$\mu(T) = \mu_0 \left(\frac{T}{T_0}\right)^{3/2} \frac{T_0 + S}{T + S} \tag{2.35}$$

where $S \approx 110$ K for air, and μ_0 is a reference viscosity. Alternatively, a power-law approximation is sometimes used [9]:

$$\mu(T) = \mu_{\text{ref}} \left(\frac{T}{T_{\text{ref}}}\right)^n \tag{2.36}$$

with $n \approx 0.666$ for air.

Thermal conductivity is related to viscosity and specific heat through Chapman-Enskog theory. For polyatomic gases, the Eucken formula, originally derived by Eucken in 1913 [17], provides a useful approximation:

$$k = \frac{\mu c_p}{\text{Pr}} \tag{2.37}$$

where the Prandtl number $\text{Pr} = \frac{\mu c_p}{k}$ is generally $\text{Pr} \approx 0.72$ for air at moderate temperatures. The Hansen law provides an alternative form similar to the Sutherland law for viscosity, specifically designed for hypersonic applications [9].

2.2.5 Skin Friction and Heat Transfer Coefficients

The primary outputs of boundary layer analysis are the **wall shear stress** and **wall heat flux**, which determine structural loading and thermal protection requirements. The shear stress at the wall is:

$$\tau_w = \mu_w \left(\frac{\partial u}{\partial y}\right)_w \tag{2.38}$$

where subscript w denotes wall conditions. This is nondimensionalized as the skin friction coefficient:

$$C_f = \frac{\tau_w}{q_\infty} = \frac{\tau_w}{\frac{1}{2}\rho_\infty V_\infty^2} \tag{2.39}$$

The wall heat flux is given by Fourier's law:

$$q_w = -k_w \left(\frac{\partial T}{\partial y}\right)_w \tag{2.40}$$

This is nondimensionalized using the Stanton number:

$$C_H = \frac{q_w}{\rho_\infty V_\infty (h_{aw} - h_w)} \tag{2.41}$$

where h_{aw} is the **adiabatic wall enthalpy**, defined as the enthalpy reached by the flow if brought to rest adiabatically. For an ideal gas, $h_{aw} = h_e + r\frac{V_e^2}{2}$, where r is the recovery factor ($r \approx \text{Pr}^{1/3} \approx 0.89$ for air) [9, 64].

Stagnation Point Heating and Nose Radius Dependence

The peak surface heating in hypersonic flows occurs at the **stagnation point**, the point on the vehicle nose where the freestream flow is brought to rest [9]. At this location, the entire kinetic energy of the freestream is converted into thermal energy and pressure rise. Understanding the scaling of stagnation point heat flux with geometric parameters is essential for reentry vehicle design.

Classical laminar stagnation point theory, validated extensively by experiment and computation, predicts that the convective heat flux at the stagnation point depends explicitly on the nose radius of curvature R through a relation of the form [19, 4]:

$$q_{w,0} \propto \frac{1}{\sqrt{R}} \tag{2.42}$$

This scaling is perhaps the most consequential relationship in hypersonic vehicle design: the stagnation point heat flux **decreases as the inverse square root of the nose radius**. Physically, a larger nose radius creates a thicker shock layer, increases the density gradient, and permits more gradual momentum accommodation. All effects that reduce the concentration of heat flux at a single point.

Design implication: Increasing the nose radius R by a factor of 4 reduces stagnation point heating by a factor of 2. This fundamental scaling explains why space reentry capsules (Apollo, Soyuz, Crew Dragon, etc.) employ large, hemispherical or blunt conical nose geometries: they minimize peak heating despite accepting higher aerodynamic drag. In contrast, hypersonic cruise missiles or advanced reconnaissance aircraft may employ more pointed noses to reduce drag, accepting elevated heating as a trade-off. The relationship in Equation (2.42) is robust across entry conditions and flight regimes, remaining valid even with real gas effects and radiative cooling corrections [9, 4].

2.2.6 Reference Temperature Method

A practical engineering approach to account for the strong temperature variations in compressible boundary layers is the **reference temperature method**, which employs incompressible boundary layer formulas evaluated at a reference temperature T^* representative of conditions within the boundary layer. Various empirical expressions exist for T^*; a commonly used form, based on the Lees-Dorodnitsyn transformation [13, 32, 52], is:

$$T^* = T_w + \alpha(T_e - T_w) + \beta(T_{aw} - T_e) \tag{2.43}$$

Where α and β are empirical coefficients dependent on the Prandtl number. A typical choice is $\alpha = 0.5$ and $\beta = 0.22$ for air, values that yields good agreement across a wide range of Mach numbers and pressure ratios [15].

With the Lees-Dorodnitsyn transformation, the incompressible Blasius solution for flat-plate skin friction becomes applicable in compressible flows, with Reynolds number and Prandtl number evaluated at T^*. This method is widely used in preliminary design because it avoids solving the full boundary layer equations while capturing the dominant effects of compressibility.

2.2.7 Hypersonic Viscous Interactions

A distinctive feature of hypersonic flows is the strong coupling between the boundary layer and the external inviscid flow, a phenomenon that becomes increasingly important as Mach number increases and Reynolds number decreases. The boundary layer removes mass from the inviscid stream through the displacement effect and displaces streamlines outward by a distance approximately equal to the displacement thickness $\delta^*(x)$. At hypersonic speeds, even this modest deflection produces a significant pressure rise that modifies the pressure field felt by the boundary layer itself. This interaction between the shock structure and the thick boundary layer can substantially alter heating rates, skin friction, and pressure distributions compared to isolated boundary layer or inviscid predictions [9, 4].

The governing parameter for characterizing the strength of hypersonic viscous interaction is the **viscous interaction parameter**:

$$\bar{\chi} = \sqrt{\frac{C}{Re_x}} M_\infty^3 \tag{2.44}$$

where $C = rho_w \mu_w / \rho_e \mu_e$ is a constant, $Re_x = \rho_\infty V_\infty x / \mu_\infty$ is the local Reynolds number based on distance x from the leading edge, and M_∞ is the freestream Mach number. This parameter arises naturally from scaling analysis of the compressible boundary layer equations and compares the magnitude of pressure gradients induced by boundary layer displacement to the dynamic pressure of the freestream [4].

Two regimes are distinguished based on $\bar{\chi}$ [9, 4]:

Weak interaction ($\bar{\chi} < 3$): The boundary layer develops nearly independently, and pressure perturbations from the interaction are small. Standard boundary layer methods apply with good accuracy. The external pressure distribution from inviscid flow theory can be used with minimal correction.

Strong interaction ($\bar{\chi} > 3$): The shock-induced pressure rise is comparable to or exceeds the freestream dynamic pressure. The boundary layer and inviscid flow must be solved coupled. Pressure-driven phenomena dominate, and simple boundary layer assumptions break down. The boundary layer can separate, creating recirculation regions with very high heating.

At high Mach numbers (exceeding approximately 5) combined with low unit Reynolds numbers (characteristic of high-altitude reentry), strong interaction effects can increase local pressure by 50-100% and heating rates by factors of 2-5 above isolated boundary-layer predictions. Such effects have historically caused material failures and aerodynamic surprises in hypersonic flight test programs [9, 4].

In strong interaction regions, the viscous displacement causes a shock deflection that increases the local shock strength. This feedback loop can produce shock-induced separation, where the adverse pressure gradient reverses the boundary layer flow, creating a separation bubble with recirculating flow. Inside such regions, temperatures reach extreme values and heating concentrates over small areas, creating critical design challenges for thermal protection systems [9].

2.2.8 Shock-Boundary Layer Interactions and Aerodynamic Heating

When an external shock wave impinges upon a boundary layer, the shock-induced pressure jump can cause boundary layer separation if the external pressure rise is sufficiently steep. In separated regions, recirculating flow with low velocities but high temperatures can produce extreme localized heating. These **shock-boundary layer interactions** (SBLI) are classified into families identified by Edney [16], and certain types (particularly Edney Type III and IV) produce heating rates exceeding baseline predictions by one to two orders of magnitude [9].

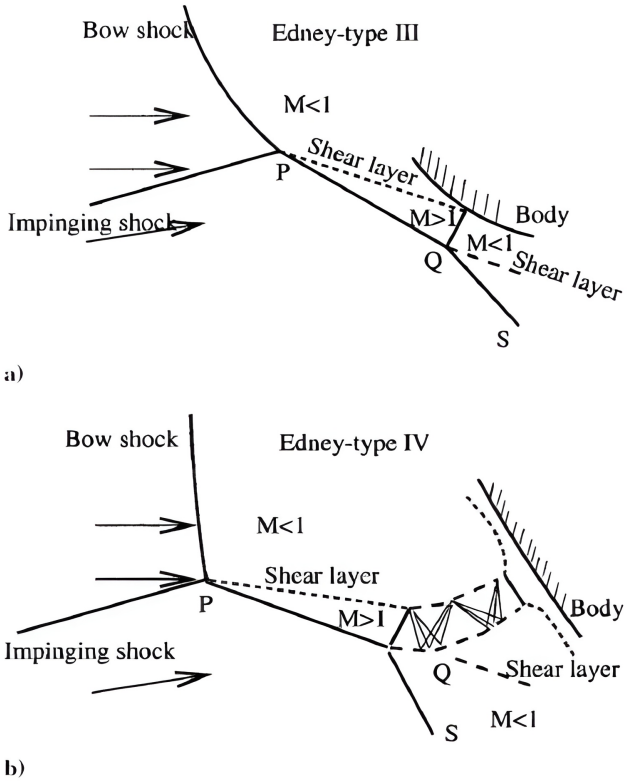

Figure 2.5. Edney type III (a) and Edney type IV (b) SBLI [9].

The classical example of SBLI consequences occurred during a final flight test of the X-15 research aircraft at Mach 6.72 in 1967, when an impinging shock from a dummy ramjet burned a hole through the pylon structure, nearly causing loss of the vehicle [12]. Modern hypersonic vehicle design must account for SBLI effects through detailed CFD analysis or empirical correlations based on seminal heating correlations such as the Fay-Riddell correlation [19], and control surface deflections or inlet designs must be managed to avoid such interactions [9].

2.2.9 Low-Density Effects and Slip Flow

At sufficiently high altitudes and extreme Mach numbers, the number density of air molecules becomes small enough that the continuum assumption breaks down. The relevant nondimensional parameter is the **Knudsen number**:

$$\mathrm{Kn} = \frac{\lambda}{L} \tag{2.45}$$

where:

$$\lambda = \frac{k_B T}{\sqrt{2}\pi d^2 p} \tag{2.46}$$

is the mean free path and L is a characteristic length. At $\mathrm{Kn} \ll 0.01$, continuum theory is valid. At $\mathrm{Kn} \geq 0.1$, rarefied gas effects become important [9].

In the **slip flow regime** ($0.01 < \mathrm{Kn} < 0.1$), the continuum equations remain approximately valid but boundary conditions must be modified. Specifically, the no-slip condition gives way to finite slip velocities proportional to the velocity gradient at the wall:

$$u_{\mathrm{slip}} = \lambda \left(\frac{\partial u}{\partial y} \right)_w \tag{2.47}$$

Similarly, a temperature slip develops. These effects reduce skin friction and heat transfer compared to continuum predictions.

Modern hypersonic vehicle analysis at reentry altitudes above 80 km must account for such rarefied gas effects, typically through the addition of slip boundary conditions or the use of direct simulation Monte Carlo (DSMC) methods for highly rarefied flows. Comprehensive treatments of rarefied gas dynamics and their application to hypersonic vehicle design are provided by Vincenti and Kruger [63].

2.3 High-Temperature Hypersonic Aerothermodynamics

The fundamental rationale for studying high-temperature gas dynamics in hypersonic flows is that regions of very high temperature exist where thermochemical processes dissociation, vibrational excitation, ionization, and chemical reactions are sufficiently intense to influence or even dominate the flowfield characteristics [9]. During atmospheric entry of hypersonic vehicles, the large kinetic energy of the bulk flow is converted through the strong shock wave in front of the blunt body into internal energy, creating very high temperatures in the shock layer region, especially near the nose [9]. Downstream of the nose, the flow expands and cools, but within the boundary layer where frictional dissipation is significant, temperatures remain sufficiently high to produce chemically reacting flow [9, 4]. This section develops the thermodynamic properties of reacting gas mixtures and formulates governing equations valid in equilibrium and non-equilibrium conditions.

2.3.1 Thermally Perfect and Calorically Imperfect Gases

At hypersonic flight conditions, air can no longer be treated as a calorically perfect gas, a gas with constant specific heats. Instead, a **thermally perfect gas** model is employed, wherein the constituents obey the perfect gas law $p = \rho RT$ but possess specific heats that are functions of temperature only [9]. Such temperature-dependent specific heats arise from the quantum mechanical quantization of internal energy modes: translational, rotational, vibrational, and electronic energy levels.

For a mixture of thermally perfect gases, the composition variables y_i, x_i, q_i relate the mass fractions, mole fractions, and mole-mass ratios through:

$$x_i = \frac{y_i}{M_i}\left(\sum_j \frac{y_j}{M_j}\right)^{-1}, \quad q_i = \frac{x_i}{\sum_j x_j} = \frac{x_i}{1} \tag{2.48}$$

where M_i is the molar mass of species i. The mixture molecular weight is:

$$M_{\text{mix}} = \left(\sum_i \frac{y_i}{M_i}\right)^{-1} \tag{2.49}$$

The specific gas constant for the mixture is:

$$R_{\text{mix}} = \frac{R_u}{M_{\text{mix}}} \tag{2.50}$$

where $R_u = 8.314\ \text{J/(mol} \cdot \text{K)}$ is the universal gas constant.

2.3.2 Internal Energy Modes and Partition Functions

The total internal energy of a molecule consists of four quantized contributions:

$$e'_{\text{total}} = e'_{\text{trans}} + e'_{\text{rot}} + e'_{\text{vib}} + e'_{\text{el}} \tag{2.51}$$

where trans, rot, vib, and el denote translational, rotational, vibrational, and electronic modes, respectively. Each mode contributes to the specific heat according to quantum mechanics and statistical thermodynamics [9, 4].

For a diatomic molecule at a given temperature in equilibrium conditions, statistical thermodynamics provides expressions for the contribution of each energy mode:

$$\begin{aligned} e_{\text{trans}} &= \frac{3}{2}RT, \\ e_{\text{rot}} &= RT, \\ e_{\text{vib}} &= \frac{R\Theta_v^i}{e^{\Theta_v^i/T}-1}, \\ e_{\text{el}} &\approx 0 \quad \text{(at moderate temperatures)} \end{aligned} \tag{2.52}$$

where $\Theta_v^i = h\nu_i/k_B$ is the characteristic vibrational temperature of species i, with h Planck's constant and ν_i the fundamental vibrational frequency [9]. Typical values for air constituents are $\Theta_v^{O_2} \approx 2240$ K, $\Theta_v^{N_2} \approx 3354$ K, and $\Theta_v^{NO} \approx 2740$ K.

2.3.3 Chemical Equilibrium and the Equilibrium Constant

In equilibrium conditions, chemical reactions reach a balance state governed by the equilibrium constant $K_p(T)$, which is a function of temperature alone. For a generic reaction:

$$\sum_i n_i A_i = 0 \tag{2.53}$$

where n_i are stoichiometric coefficients (positive for products, negative for reactants), the equilibrium constant is defined through the law of mass action:

$$K_p(T) = \prod_i p_i^{n_i} \tag{2.54}$$

where p_i are partial pressures. The equilibrium constant can be computed from statistical thermodynamics and zero-point energies of reactants and products [9]:

$$K_p(T) = \prod_i \left(\frac{Q_i(T)}{p_{\text{ref}}V}\right)^{n_i} \exp\left(-\frac{\Delta e_0^{(0)}}{k_B T}\right) \tag{2.55}$$

where $Q_i(T)$ is the partition function of species i and $\Delta e_0^{(0)}$ is the change in zero-point energy across the reaction. The equilibrium composition at given temperature and pressure is determined by solving the system of equilibrium constant equations combined with elemental mass conservation constraints [9].

For air at various temperature ranges, the following dissociation and formation processes dominate:

$T < 2500$ K: Composition essentially unchanged from room temperature (N_2 and O_2 only).

$2500 < T < 4000$ K: Oxygen dissociation regime; $O_2 \rightleftharpoons 2O$, some NO formation.

$4000 < T < 8000$ K: Nitrogen dissociation regime; O_2 fully dissociated, $N_2 \rightleftharpoons 2N$ becomes significant.

$T > 8000$ K: Ionization begins; O^+, N^+, NO^+, and electrons appear. At these extreme temperatures, plasma effects and radiation become significant contributors to the overall energy balance [14].

2.3.4 Thermodynamic Properties of Equilibrium Reacting Mixtures

The enthalpy per unit mass of an equilibrium chemically reacting mixture is composed of sensible enthalpy and heat of formation:

$$h = \sum_i y_i \left[h_i^s(T) + h_{f,i}^0 \right] \tag{2.56}$$

where $h_i^s(T)$ is the sensible enthalpy of species i (energy above zero-point), and $h_{f,i}^0$ is the heat of formation per unit mass. The sensible enthalpy of each species is computed from its internal energy and the equation of state [9, 4].

The specific heat at constant pressure for the mixture is:

$$c_p = \sum_i y_i c_{p,i}(T) \tag{2.57}$$

For an equilibrium chemically reacting gas where the composition is a function of temperature and pressure only, the mixture specific heat must account for the energy required to change the chemical composition, a contribution often exceeding the individual species contributions. This is captured through **frozen** and **total** specific heats: the frozen specific heat holds composition constant, while the total specific heat allows composition to vary with temperature [24].

2.3.5 Vibrational and Chemical Non-Equilibrium

At hypersonic flight conditions, the timescales for achieving vibrational equilibrium and chemical equilibrium can exceed the flow residence time through the vehicle, resulting in **non-equilibrium** conditions. The collision dynamics governing equilibration are characterized by the **Damköhler number**:

$$\mathrm{Da} = \frac{\tau_c}{\tau_f} \tag{2.58}$$

where τ_c is the characteristic time for chemical or vibrational relaxation and $\tau_f = L/V$ is the fluid residence time. Three regimes are distinguished [9]:

Da $\ll 1$: Frozen flow; composition and vibrational energy remain essentially constant.

Da ≈ 1: Non-equilibrium flow; composition and vibrational energy change gradually.

Da $\gg 1$: Equilibrium flow; composition and vibrational energy equilibrate locally.

For vibrational relaxation, the vibrational energy of species i evolves according to [9]:

$$\frac{De_i^v}{Dt} = \frac{e_i^{v,\mathrm{eq}}(T) - e_i^v}{\tau_i^{\text{V-T}}} \tag{2.59}$$

where $e_i^{v,\mathrm{eq}}(T)$ is the equilibrium vibrational energy at the current temperature and $\tau_i^{\text{V-T}}$ is the vibrational relaxation time.

For highly excited vibrational states, non-Boltzmann distributions can occur, as documented by Treanor et al. [61].

Common relaxation time expressions, such as the Millikan-White formula [36], relate $\tau_i^{\text{V-T}}$ to temperature, pressure, and collision partners:

$$\tau_i^{\text{V-T}} = \sum_j \frac{p_j}{p} \tau_{ij}^{\text{V-T}} \tag{2.60}$$

where the sum is over all species j that collide with species i.

2.3.6 Chemical Kinetics and Reaction Mechanisms

In non-equilibrium flows, the time rate of change of species concentrations is governed by elementary chemical reactions. For an elementary reaction, the forward and backward reaction rates follow the Arrhenius form:

$$k_f = A T^n \exp\left(-\frac{E_a}{RT}\right) \tag{2.61}$$

where A is the pre-exponential factor, n is the temperature exponent, and E_a is the activation energy [9, 4]. For dissociation reactions, the activation energy equals the dissociation energy of the molecule.

The rate of change of concentration $[X_i]$ for species i participating in elementary reaction r is:

$$\left.\frac{d[X_i]}{dt}\right|_r = (n_i'' - n_i') \left[k_f \prod_j [X_j]^{n_j'} - k_b \prod_j [X_j]^{n_j''} \right] \tag{2.62}$$

where n_i' and n_i'' are stoichiometric coefficients for reactants and products. The backward rate is related to the forward rate and equilibrium constant through $k_b = k_f / K_c$ [9].

For air at reentry conditions, chemical kinetics models range from simplified three-reaction mechanisms (the Zeldovich [69] process for NO formation) to comprehensive 11-species models [23, 4, 44, 46]. Modern models account for dissociation of O_2 and N_2, formation and dissociation of NO, atomic species reactions, and at high temperatures, ionization processes [23].

2.3.7 Governing Equations for High-Temperature Flows

For inviscid equilibrium flows, the Euler equations remain valid but with modified closure relations accounting for chemical composition changes and temperature-dependent thermodynamic properties:

$$\frac{\partial \rho}{\partial t} + \nabla \cdot (\rho \mathbf{v}) = 0 \tag{2.63}$$

$$\frac{\partial (\rho \mathbf{v})}{\partial t} + \nabla \cdot (\rho \mathbf{v}\mathbf{v}) + \nabla p = 0 \tag{2.64}$$

$$\frac{\partial E}{\partial t} + \nabla \cdot [(E + p)\mathbf{v}] = 0 \tag{2.65}$$

The total energy now incorporates the heat of formation through the total enthalpy:

$$E = \rho \left[e_{\text{sens}}(T) + h_f(T, p) + \frac{1}{2}|\mathbf{v}|^2 \right] \tag{2.66}$$

For non-equilibrium flows, species conservation equations are added:

$$\frac{\partial (\rho y_i)}{\partial t} + \nabla \cdot (\rho y_i \mathbf{v}) = -\nabla \cdot \mathbf{J}_{m,i} + W_i^{\text{ch}} \tag{2.67}$$

where $\mathbf{J}_{m,i}$ is the species diffusive flux and W_i^{ch} is the chemical production rate per unit volume from reaction kinetics. If vibrational non-equilibrium is significant, energy equations for each vibrating species must be added [9].

2.3.8 Transport Properties at High Temperature

Transport properties (viscosity, thermal conductivity, and diffusion coefficients) must be computed at each point accounting for the local mixture composition. For viscosity, Chapman-Enskog kinetic theory provides accurate expressions, though empirical modifications are often necessary at high temperatures [9]. The mixture viscosity is computed from the individual species viscosities through relationships such as Wilke's rule or by solving linearized transport equations [9].

The thermal conductivity of a reacting mixture includes contributions from conduction through the gas and enthalpy transport by species diffusion. For a chemically reacting mixture:

$$\mathbf{q} = -k_{\text{mix}} \nabla T + \sum_i h_i \mathbf{J}_{m,i} \tag{2.68}$$

The second term represents energy transport by diffusing species, which can significantly enhance the effective heat transfer in the presence of strong concentration gradients [9].

2.3.9 Shock-Wave Structure in Reacting Gases

Normal shock waves in high-temperature air exhibit structure dramatically different from calorically perfect gas shocks. The density ratio across a shock can exceed values predicted by perfect gas theory because energy is absorbed into internal excitation modes and chemical reactions. Across a stationary normal shock, conservation laws give:

$$\begin{aligned} \rho_1 V_1 &= \rho_2 V_2 \\ p_1 + \rho_1 V_1^2 &= p_2 + \rho_2 V_2^2 \\ h_1 + \frac{1}{2} V_1^2 &= h_2 + \frac{1}{2} V_2^2 \end{aligned} \tag{2.69}$$

where subscripts 1 and 2 denote upstream and downstream conditions. At high temperatures, chemical equilibrium is typically assumed across the shock, so the post-shock composition is determined from the equilibrium constant equations applied at the post-shock temperature. The classical treatment of shock waves in high-temperature gases is provided by Zeldovich and Raizer [69], with modern computational approaches detailed by Gupta and Srinivasan [55, 24].

A key result is that the shock standoff distance (the distance between the body and shock surface) is noticeably smaller in dissociating flows than in perfect gas flows, because the higher density downstream of the shock (due to internal energy absorption) compresses the shock layer [9, 4]. Similarly, oblique shock angles are reduced, affecting pressure distributions and aerodynamic coefficients [9].

2.3.10 Boundary Layer Effects and Surface Chemistry

In the boundary layer of hypersonic vehicles, temperatures can remain high enough for continued chemical reactions. The boundary conditions at a solid surface depend critically on whether the surface is **catalytic**, promoting chemical recombination, or **non-catalytic**, inert to chemical reactions [9, 4]. For a catalytic wall, atomic species recombine, releasing dissociation energy to the surface as heat. For a non-catalytic wall, atoms remain uncombined, reducing the heat flux. The heat flux at a fully catalytic wall significantly exceeds that at a non-catalytic surface, often by factors of 2–4, dramatically affecting vehicle thermal loads and ablation rates [9].

2.4 Radiation Heating in Hypersonic Flows

At sufficiently high temperatures during atmospheric entry, thermal radiation becomes a significant energy transport mechanism and contributes substantially to the total heat flux incident on the vehicle surface [9]. The total aerothermal heating is thus composed of two components:

$$q_{\text{total}} = q_c + q_r \tag{2.70}$$

where q_c is the convective heating due to conduction and diffusion across the boundary layer, and q_r is the radiative heating from the shock layer and surrounding atmosphere. At entry velocities exceeding approximately 11 km/s and at low altitudes where shock layer temperatures exceed ~ 5000 K, radiative heating can equal or exceed convective heating, fundamentally altering vehicle thermal protection design [9, 4]. This section develops the governing equations for radiative transfer and quantifies radiation heating contributions to hypersonic vehicle design.

2.4.1 Fundamental Concepts: Radiative Intensity and Blackbody Radiation

The foundation of radiative transfer analysis rests on two fundamental quantities: the **specific radiative intensity** and the **radiative flux** [9]. The specific radiative intensity I_ν is defined as the radiative energy emitted per unit area, per unit solid angle $d\omega$, per unit frequency $d\nu$, per unit time. Mathematically:

$$dE = I_\nu \cos\theta \, dA \, d\Omega \, d\nu \, dt \tag{2.71}$$

where θ is the angle between the emission direction and the surface normal. The radiative flux is obtained by integrating the intensity over all directions and frequencies:

$$q = \int_0^\infty \int_\omega I_\nu \cos\theta \, d\omega \, d\nu \tag{2.72}$$

For a **blackbody**, an idealized surface that absorbs all incident radiation and emits according to Planck's law, the radiative intensity is given by the **Planck function** [48]:

$$B_\nu(T) = \frac{2h\nu^3}{c^2} \frac{1}{e^{h\nu/k_B T} - 1} \tag{2.73}$$

where h is Planck's constant, ν is frequency, c is the speed of light, k_B is Boltzmann's constant, and T is temperature. Integration of the Planck function over all frequencies yields the **Stefan-Boltzmann law**:

$$q_{\text{bb}} = \sigma T^4 \tag{2.74}$$

where $\sigma = 5.67 \times 10^{-8}$ W/(m$^2 \cdot$ K^4) is the Stefan-Boltzmann constant [9]. The strong temperature dependence (T^4) explains why radiative heating becomes dominant at very high temperatures.

2.4.2 Kirchhoff's Law and the Radiative Transfer Equation

For a real gas (non-blackbody) in local thermodynamic equilibrium, **Kirchhoff's law of thermal radiation** [31] relates the emission and absorption properties:

$$\frac{\varepsilon_\nu}{\alpha_\nu} = B_\nu(T) \tag{2.75}$$

where ε_ν is the monochromatic emissivity and α_ν is the monochromatic absorptivity. For a body in thermal equilibrium with its surroundings, $\varepsilon_\nu = \alpha_\nu$, meaning the emissivity equals the absorptivity. A result with profound implications for energy balance.

When radiation propagates through a volume element of absorbing and emitting gas, the radiative intensity changes according to the **radiative transfer equation**:

$$\frac{dI_\nu}{ds} = J_\nu - k_\nu I_\nu \tag{2.76}$$

where J_ν is the emission coefficient (energy emitted per unit volume, solid angle, frequency, and time) and k_ν is the absorption coefficient [9]. Invoking Kirchhoff's law, the emission and absorption coefficients are related:

$$J_\nu = k_n u B_\nu(T) \tag{2.77}$$

allowing the transfer equation to be rewritten as:

$$\frac{dI_\nu}{ds} = k_\nu[B_\nu(T) - I_\nu] \tag{2.78}$$

Comprehensive treatments of this fundamental equation governing radiative transport are provided by [53, 37].

2.4.3 Optical Thickness and Limiting Cases

The **optical thickness** or **optical depth** τ_ν along a path of length L is defined as:

$$\tau_\nu = \int_0^L k_\nu(s)\, ds \tag{2.79}$$

This dimensionless quantity governs the behavior of radiation in different regimes [9]:

$\tau_\nu \ll 1$ **(optically thin):** Most radiation emitted at any point escapes the gas without being absorbed. The gas is transparent.

$\tau_\nu \approx 1$ **(optically intermediate):** Partial absorption and re-emission occur.

$\tau_\nu \gg 1$ **(optically thick):** Radiation cannot escape and the medium approaches blackbody behavior.

For a transparent gas emitting but not absorbing radiation, the solution to the transfer equation is:

$$I_\nu(s) = I_\nu(0)\exp(-\tau_\nu) \tag{2.80}$$

For an absorbing gas with constant properties, the solution is:

$$I_\nu(s) = I_\nu(0)e^{-k_\nu L} + B_\nu(T)(1 - e^{-k_\nu L}) \tag{2.81}$$

For a general gas with variable properties that both emits and absorbs, the solution becomes:

$$I_\nu(s_1) = I_\nu(0)e^{-\tau_\nu(s_1)} + \int_0^{\tau_\nu(s_1)} B_\nu(s(\tau))e^{-[\tau_\nu(s_1)-\tau]}d\tau \tag{2.82}$$

This equation shows that the received intensity is a superposition of the attenuated initial intensity and radiation emitted at all points along the path, each attenuated according to the distance traveled to the observer [9].

2.4.4 Self-Absorbing versus Transparent Gas Models

In hypersonic shock layers, two limiting approximations are commonly employed [9]:

Self-absorbing gas: the gas both emits and absorbs radiation. Radiation emitted at any point can influence any other region, introducing elliptic mathematical behavior. Even in supersonic flows, information propagates upstream through radiation. This model is accurate when the shock layer is optically thick.

Transparent gas: the gas emits radiation but does not absorb it. All emitted energy escapes to the surroundings. Radiation effects are purely local (hyperbolic behavior). This model applies when the shock layer is optically thin, as is often the case at low-pressure, high-altitude reentry conditions.

For a thin, high-temperature shock layer approximated as a slab of uniform properties, the radiative heat flux incident at the wall is derived from integrating the Planck function over the shock layer volume [9]. For the transparent gas assumption:

$$q_r = E_e \tag{2.83}$$

where $E_e = 4\pi \int_0^\infty J_\nu d\nu$ is the emissive power per unit volume, the total energy emitted in all directions per unit time per unit volume [9].

2.4.5 Shock Standoff Distance and Radiative Blunting

A significant consequence of radiation in the shock layer is modification of the shock standoff distance. Classical shock-fitting analyses show that the shock standoff distance Δ at the stagnation point varies as [9]:

$$\frac{\Delta}{R} \propto \frac{\rho_1}{\rho_2} \tag{2.84}$$

where R is the nose radius of curvature, ρ_1 the freestream density and ρ_2 is the post-shock density. The effects of radiative cooling on shock layer structure and standoff distance have been extensively studied by Goulard [21]. In equilibrium dissociating air,

the post-shock density is higher than in perfect gas flows because energy is absorbed into internal excitation modes rather than thermal motion. However, at extremely high temperatures where significant ionization occurs, the post-shock temperature rise is moderated due to energy absorption into ionization, reducing the post-shock density and *increasing* the shock standoff distance compared to a perfect gas [9].

Importantly, the radiative heat flux scaling differs fundamentally from convective heating. The radiative heat flux at the wall is found to be proportional to the body curvature:

$$q_r \propto R \tag{2.85}$$

This contrasts sharply with convective heating, which scales inversely with $\sqrt{R}$. Consequently, for blunt-nosed entry vehicles, there is an optimal nose radius that minimizes the sum of convective and radiative heating, a critical design consideration for lunar return and interplanetary entry missions [9].

2.4.6 Spectral Properties and Absorption Coefficients

Real hypersonic flows involve complex mixtures of molecules, atoms, and ions over a wide range of temperatures. The absorption coefficient k_ν depends critically on the shock layer composition and spectral region [9]. Major radiative processes include:

Continuum absorption: free-free transitions (bremsstrahlung), free-bound transitions (photoionization), and bound-free absorption.

Line radiation: atomic and molecular electronic transitions, yielding discrete spectral lines.

Band radiation: electronic bands of diatomic molecules and radicals (N_2, O_2, NO), significant at intermediate temperatures ($\sim$ 4000–10,000 K).

At entry temperatures below $\sim$ 5000 K, molecular band radiation (particularly from NO) dominates. At higher temperatures, atomic line emission and continuum radiation become important. These radiative processes have been characterized in detail for hypersonic reentry conditions by Dunn and Kang [14]. At temperatures exceeding $\sim$ 10,000 K, ionization processes produce bound-free radiation and line radiation from ions.

Modern computational approaches employ spectral models (narrow-band or statistical) to efficiently integrate the transfer equation across the full spectrum without resolving individual spectral lines. These models use precalculated opacity tables or inline spectroscopic calculations to determine k_ν at each point in the flowfield [37].

2.4.7 Coupling of Radiation to Flow Dynamics

In the energy conservation equation, the divergence of the radiative heat flux appears as a volumetric energy source:

$$\nabla \cdot \mathbf{q}_r = \int_0^\infty \int_{4\pi} J_\nu \, d\omega \, d\nu - \int_0^\infty \int_{4\pi} k_\nu I_\nu \, d\omega \, d\nu \tag{2.86}$$

The first term represents energy lost through emission, while the second represents energy gained through absorption. When radiative energy losses are large, the temperature throughout the shock layer is reduced below the adiabatic value predicted by inviscid theory. This **radiative cooling** can reduce shock layer temperatures by 10–20% or more, depending on the entry conditions [9, 4].

The coupling of radiation to the governing equations requires simultaneous solution of the radiative transfer equation together with the continuity, momentum, and energy equations, as described from Candler and MacCormack [6]. This fully coupled approach is essential for accurate prediction of shock layer structure and surface heating at very high entry speeds [9].

2.4.8 Engineering Correlations and Design Implications

For preliminary design and feasibility studies, engineering correlations are often employed to estimate radiative heating without solving the full transfer equation. A commonly used approach employs the **integral hemispherical emissivity** ϵ_0 of the shock layer at a representative temperature and composition [9]:

$$q_r \approx \epsilon_0 \sigma T_{\text{shock}}^4 \tag{2.87}$$

where T_{shock} is a characteristic shock layer temperature. The integral emissivity ϵ_0 (typically 0.1–0.8 depending on composition and temperature) must be determined from spectroscopic data or computational codes [9].

The importance of radiation heating is quantified by the **radiation parameter** or **Boltzmann number**, which compares radiative to convective heating scales. For lunar return trajectories and beyond-Earth missions, radiative heating can dominate and requires high-fidelity modeling to ensure thermal protection system adequacy and vehicle structural integrity [9].

Chapter 3

Computational Fluid Dynamics for Hypersonic Regime

Following the presentation of the physical models for hypersonic flows in Chapter 2 (encompassing inviscid and viscous compressible flows, high-temperature effects, and radiative heating) the discretization of these governing equations into algebraic systems suitable for digital computation represents the essential bridge between theory and practical simulation [4]. The compressible Navier-Stokes equations, supplemented by a real gas equation of state, form a coupled system of hyperbolic-parabolic conservation laws whose solution demands carefully designed numerical methods [60].

Unlike incompressible flows, where the continuity equation is a constraint (leading to pressure-Poisson methods), or purely inviscid flows where only convective fluxes matter, the compressible regime presents both challenges: the flow is governed by a hyperbolic system (Euler equations) with added parabolic terms (viscous and diffusive fluxes) [3]. The numerical methodology must therefore:

- **Preserve conservation in discrete form:** mass, momentum, and energy must be conserved exactly within the computational domain.
- **Capture shock discontinuities with minimal smearing**, employing upwind methods and shock-capturing techniques derived from hyperbolic theory.
- **Resolve boundary layers with adequate precision**, requiring fine grid spacing near walls and careful discretization of viscous terms.
- **Handle real gas effects**, where density, viscosity, and thermal conductivity vary nonlinearly with temperature and composition.
- **Maintain stability and accuracy** across the wide range of Mach numbers and temperatures encountered in hypersonic applications.

This chapter develops the discretization framework starting from the continuous equations, through spatial approximation via the finite volume method, temporal advancement via explicit forward Euler schemes, and implementation of boundary conditions specific

to hypersonic flows. The treatment unifies the upwind methodology for convective terms (developed on the mathematical foundation of the Riemann problem and characteristic analysis) with the central differencing approach for viscous terms, yielding a practical and robust numerical algorithm suitable for hypersonic aerothermodynamic predictions [60, 33].

3.1 Mathematical Structure of Compressible Navier-Stokes Equations

3.1.1 Conservative Form and Physical Variables

The compressible Navier-Stokes equations in conservative form, as presented in Chapter 2, are written as:

$$\frac{\partial \mathbf{U}}{\partial t} + \nabla \cdot (\mathbf{F}_c - \mathbf{F}_v) = \mathbf{S} \tag{3.1}$$

where:

- $\mathbf{U} = [\rho, \rho u, \rho v, \rho w, \rho E]^T$ is the vector of conservative variables (density, momentum components, total energy),
- $\mathbf{F}_c$ are the convective (inviscid) fluxes, functions of pressure and velocity,
- $\mathbf{F}_v$ are the viscous fluxes, depending on gradients of velocity and temperature,
- $\mathbf{S}$ represents source terms (radiative heating, chemical reactions, etc.).

The coupling between the five conservation equations arises from the following dependencies [4]:

- Equation of state: for real gases, the pressure is not simply $p = (\gamma - 1)\rho e$ but requires evaluation through thermodynamic tables or correlations. Similarly, dynamic viscosity $\mu(T)$, thermal conductivity $\kappa(T)$, and second viscosity $\lambda(T)$ depend on the local temperature.
- Internal energy and temperature: the specific internal energy e is related to temperature through enthalpy $h = c_p(T)T$, where $c_p(T)$ is the temperature-dependent specific heat at constant pressure. The total energy is then $E = e + \frac{1}{2}(u^2 + v^2 + w^2)$.
- High-temperature nonequilibrium: in hypersonic regimes, vibrational excitation and molecular dissociation occur. The internal energy comprises translational, rotational, vibrational, and electronic contributions, each evolving on different time scales.

These interdependencies are encoded in a *thermodynamic model* specific to the gas composition, ranging from calorically-perfect gas models (sufficient at moderate temperatures) to complex multitemperature models (essential for reentry conditions).

3.1.2 Hyperbolicity and Characteristic Structure

The convective part of the Navier-Stokes system, obtained by setting viscous fluxes to zero, forms a hyperbolic system whose eigenstructure determines the propagation of disturbances [60]. For a one-dimensional flow in the x-direction, the Jacobian matrix of the convective flux admits three real eigenvalues:

$$\lambda_1 = u - a, \quad \lambda_2 = u, \quad \lambda_3 = u + a \tag{3.2}$$

where $a = \sqrt{\gamma p/\rho}$ is the local sound speed. Each eigenvalue corresponds to a wave family:

- Acoustic waves: eigenvectors λ_1 (leftward) and λ_3 (rightward), carrying pressure and density perturbations.
- Material surface (or contact discontinuity): eigenvalue λ_2, across which density and entropy may jump but pressure and normal velocity remain continuous.

The existence of real, distinct eigenvalues ensures hyperbolicity [10]. This mathematical structure is essential: it justifies the application of upwind methods (which exploit characteristic speeds) and ensures that the Riemann problem is well-posed. The viscous terms, while parabolic in character, do not affect hyperbolicity; they are responsible for entropy increase and represent physical diffusion of momentum and heat [3].

3.2 The Riemann Problem in Hypersonic Flows

3.2.1 Riemann Problem Formulation

The Riemann problem for the Navier-Stokes equations is, strictly speaking, not well-defined because the system contains parabolic (diffusive) terms. However, the practical relevance of the Riemann problem comes from its role in discretizing the *convective fluxes* at cell interfaces [60]. At each interface, one solves a piecewise-constant Riemann problem for the hyperbolic part:

$$\frac{\partial \mathbf{U}}{\partial t} + \nabla \cdot \mathbf{F}_c(\mathbf{U}) = 0 \tag{3.3}$$

with initial data:

$$\mathbf{U}(x,0) = \begin{cases} \mathbf{U}_L & x < 0 \\ \mathbf{U}_R & x > 0 \end{cases} \tag{3.4}$$

The solution $\mathbf{U}^{\mathrm{RP}}(\xi; \mathbf{U}_L, \mathbf{U}_R)$, where $\xi = x/t$, is self-similar and consists of three wave structures as discussed in earlier sections. The key observation is that this solution correctly represents the inviscid limit of the Navier-Stokes equations: for sufficiently coarse grids (where viscous effects within a cell are negligible), the Riemann solution dominates the flow evolution across interfaces.

3.2.2 Shock Structure and Viscous Effects

In the continuous Navier-Stokes equations, shocks have finite thickness determined by the balance between convection (steepening the gradient) and viscous diffusion (smoothing it) [4]. The shock thickness is of order $\mathcal{O}(\mu/(\rho a))$, which for hypersonic flows is extremely small (typically microns for atmospheric entry).

In the discrete setting, the mesh resolution is typically much coarser than the physical shock thickness, so the shock appears as a numerical discontinuity captured over several grid cells. The numerical method must [60]:

- Use the exact (or nearly-exact) Riemann solution to the convective part to determine the flux at the interface, ensuring correct shock speed and intermediate state.
- Include sufficient artificial dissipation (from either upwinding or TVD limiting) to prevent spurious oscillations across the captured shock.
- Avoid explicit modeling of the thin viscous layer (which would require mesh refinement to μ scale), but instead use the entropy condition from thermodynamics to select the physically correct shock.

The Riemann solver thus serves as a shock-capturing mechanism: it enforces the correct jump conditions and entropy increase without resolving the inner structure [67].

3.3 Finite Volume Discretization

3.3.1 Cell-Centered Formulation

The finite volume method begins by integrating the conservation laws over each control volume V_i bounded by surfaces ∂V_i [33]:

$$\frac{d}{dt}\int_{V_i} \mathbf{U}\, dV + \oint_{\partial V_i} (\mathbf{F}_c - \mathbf{F}_v)\cdot \hat{\mathbf{n}}\, dS = \int_{V_i} \mathbf{S}\, dV \tag{3.5}$$

Assuming the solution is approximated by cell-center values $\mathbf{U}_i$, which represent the spatial average over the cell:

$$\mathbf{U}_i \approx \frac{1}{V_i}\int_{V_i} \mathbf{U}\, dV \tag{3.6}$$

the discrete evolution equation becomes [10]:

$$V_i \frac{d\mathbf{U}_i}{dt} = \sum_{\text{faces } j} [(\mathbf{F}_{c,j} - \mathbf{F}_{v,j})\cdot \hat{\mathbf{n}}_j A_j] + V_i \mathbf{S}_i \tag{3.7}$$

where the sum is over all faces bounding cell i, A_j is the face area, and $\hat{\mathbf{n}}_j$ is the outward normal. The crucial step is the evaluation of the numerical fluxes ($\mathbf{F}_{c,j}$) and ($\mathbf{F}_{v,j}$) at each face using only the cell-average values from neighboring cells. These two contributions are treated separately: the convective flux via upwind methods (Riemann solvers), and the viscous flux via central differencing.

3.3.2 Convective Flux Discretization

Upwind Principle and Characteristic-Based Methods

The convective part of the system is hyperbolic, and information propagates along characteristic lines at speeds determined by the local eigenvalues [60]. The upwind principle states that the numerical flux at an interface should depend on the direction of information propagation: waves moving rightward carry information from the left cell, while leftward-moving waves carry information from the right cell.

For a scalar linear advection equation $\frac{\partial u}{\partial t} + a\frac{\partial u}{\partial x} = 0$ with $a > 0$, the upwind flux is simply:

$$F_{i+1/2} = a\, u_i \tag{3.8}$$

For nonlinear systems like Navier-Stokes, the principle extends: at each interface, multiple characteristic families coexist, each with its own speed and direction. The numerical flux must synthesize contributions from all waves in a way that respects the underlying hyperbolic structure [3].

The NSA code implements two distinct approaches: Flux Difference Splitting via the Osher method, and Flux Vector Splitting via the Van Leer method, both of which are detailed in the following sections.

Flux Difference Splitting: Osher Approximate Riemann Solver

Flux Difference Splitting (FDS) provides a systematic framework for constructing convective fluxes from the characteristic structure of hyperbolic systems. Rather than solving the Riemann problem exactly, which requires iterative nonlinear root-finding at each cell interface, the NSA code employs the Osher approximate FDS method, which offers a computationally efficient alternative while maintaining entropy satisfaction and shock-capturing accuracy.

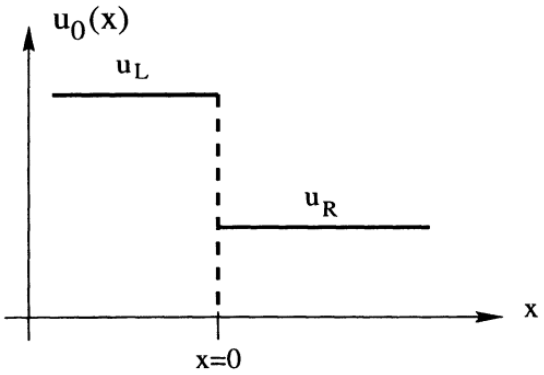

Figure 3.1. Starting point for $t = 0$ [60].

Given left and right states $\mathbf{U}_L$ and $\mathbf{U}_R$ at a cell interface, the jump in conservative variables is decomposed into contributions from characteristic waves:

$$\Delta \mathbf{U} = \mathbf{U}_R - \mathbf{U}_L = \sum_{k=1}^{m} \alpha^k \mathbf{r}^k \tag{3.9}$$

where $\mathbf{r}^k$ are the right eigenvectors of the flux Jacobian and α^k are the wave strengths (characteristic amplitudes). The wave strengths are computed from the jump using the left eigenvectors:

$$\alpha^k = (\mathbf{l}^k)^T \cdot \Delta \mathbf{U} \tag{3.10}$$

The key characteristic of the Osher method is the fundamental approximation: shock waves are treated as isentropic compression waves, rather than as discontinuous jumps. This ensures smooth flux evaluation at sonic and transonic points without requiring explicit entropy-correction procedures. Specifically, the method enforces that Riemann invariants are conserved across all characteristic families:

$$dR_1 = 0 \quad ; \quad dR_3 = 0 \tag{3.11}$$

This permits the calculation of the intermediate states using explicit, closed-form expressions, avoiding the iterative procedures required by exact solvers.

The numerical flux is then constructed by upwinding contributions based on characteristic direction:

$$F_{i+1/2} = F(\mathbf{U}_L) + \sum_{k:\lambda^k>0} \lambda^k \alpha^k \mathbf{r}^k \tag{3.12}$$

where λ^k are the eigenvalues (characteristic speeds). This ensures information propagates correctly: fast-moving (positive eigenvalue) disturbances are contributed from the left state, while slower (negative eigenvalue) features are upwinded from the right state.

The Osher method possesses several desirable properties:

1. entropy satisfaction: by treating shocks as compression waves, the method automatically satisfies the entropy inequality without explicit entropy fixes, preventing convergence to non-physical solutions at transonic rarefactions;

2. smoothness: the flux is continuously differentiable across sonic boundaries, eliminating numerical artifacts;

3. conservativity, the scheme conserves global mass, momentum, and energy through the use of conservative form;

4. computational efficiency, no iterative root-finding is required, as intermediate states and flux components are computed explicitly.

In the NSA solver, the Osher method is implemented at every cell interface by computing the left and right eigenvectors and eigenvalues from the local flow state, decomposing the jump into characteristic components, evaluating the flux contribution from each wave based on the sign of its eigenvalue, and summing contributions to construct the interface flux. This provides the convective flux component of the full spatial residual in the temporal integration scheme.

Flux Vector Splitting Framework: Van Leer Method

While Flux Difference Splitting (FDS) decomposes the jump in conservative variables into characteristic waves, an alternative approach is provided by **Flux Vector Splitting (FVS)**, which decomposes the flux vector itself rather than the conservative variable jump [62]. This framework offers distinct numerical properties and computational characteristics.

In FVS, the convective flux is decomposed into positive and negative contributions based on the sign of the characteristic speeds:

$$\mathbf{F}(\mathbf{U}) = \mathbf{F}^+(\mathbf{U}) + \mathbf{F}^-(\mathbf{U}) \tag{3.13}$$

where $\mathbf{F}^+$ represents the flux contribution from right-moving waves (positive eigenvalues) and $\mathbf{F}^-$ represents the flux contribution from left-moving waves (negative eigenvalues). The key property is that the Jacobians of the split fluxes have eigenvalues of definite sign:

$$\frac{\partial \mathbf{F}^+}{\partial \mathbf{U}} \text{ has only positive eigenvalues}, \quad \frac{\partial \mathbf{F}^-}{\partial \mathbf{U}} \text{ has only negative eigenvalues} \tag{3.14}$$

The numerical flux is then constructed using the split fluxes evaluated at the left and right cell states:

$$\mathbf{F}_{i+1/2} = \mathbf{F}^+(\mathbf{U}_L) + \mathbf{F}^-(\mathbf{U}_R) \tag{3.15}$$

This formulation ensures that information propagates in the correct characteristic direction: the positive-speed contribution comes from the left cell, while the negative-speed contribution comes from the right cell. The consistency condition is automatically satisfied:

$$\mathbf{F}_{i+1/2}(\mathbf{U}, \mathbf{U}) = \mathbf{F}^+(\mathbf{U}) + \mathbf{F}^-(\mathbf{U}) = \mathbf{F}(\mathbf{U}) \tag{3.16}$$

Among FVS schemes, the **Van Leer method** [62] is particularly noteworthy. It constructs the split fluxes using polynomial functions of the local Mach number $M = u/a$, ensuring continuous differentiability even at sonic and stagnation points. This smoothness property eliminates numerical artifacts that can arise from non-smooth transitions in the Jacobian eigenstructure [62].

For the mass flux, Van Leer employs a quadratic splitting:

$$M^+ = \begin{cases} 0 & M \leq -1 \\ \frac{1}{4}(M+1)^2 & -1 < M < 1 \\ M & M \geq 1 \end{cases}, \quad M^- = M - M^+ \tag{3.17}$$

The momentum and energy fluxes use cubic and quartic polynomials respectively, ensuring appropriate order of continuity across the sonic boundaries [62]. The final Van Leer flux splitting is:

$$\mathbf{F}^+ = \rho a M^+ \begin{pmatrix} 1 \\ u + \dfrac{2a}{\gamma+1} \\ h + \dfrac{(\gamma-1)u^2}{2(\gamma+1)} \end{pmatrix} \tag{3.18}$$

$$\mathbf{F}^- = \mathbf{F}(\mathbf{U}) - \mathbf{F}^+ \tag{3.19}$$

For supersonic regions Eq. 3.17 reduces to full upwinding: $M^+ = M$ if $M > 0$ and $M^+ = 0$ if $M < 0$, ensuring correct characteristic based flux evaluation [62].

Comparison of FDS and FVS

The two frameworks present complementary advantages and disadvantages:

- **Accuracy**: FDS methods (particularly Roe and Osher) are generally more accurate on contact discontinuities and entropy layers, as they directly represent the characteristic structure. FVS methods are less accurate near contacts but highly robust. [60]
- **Continuity**: FVS methods such as Van Leer are continuously differentiable through sonic and stagnation regions, eliminating potential numerical issues from discontinuous Jacobians. FDS solvers based on exact or linearized Riemann problems may have kinks at sonic points. [62]
- **Computational cost**: FVS is typically simpler to implement and faster per time step, as it requires no Riemann solver. FDS methods incur the cost of solving the Riemann problem (iteratively for Godunov, via eigendecomposition for Roe/Osher). [3]
- **Robustness and positivity**: FVS schemes, particularly Van Leer's, are provably positivity-preserving (mass, energy, entropy remain positive) under appropriate CFL constraints. FDS schemes require additional safeguards. [62]
- **Shock capturing**: FDS methods, combined with TVD limiting, produce sharper shock resolution. FVS methods require higher-order reconstruction to achieve comparable accuracy [60].

The choice between FDS and FVS depends on the specific application: FDS is preferred when shock-capturing accuracy is paramount, while FVS is attractive for robust, efficient simulations where extreme accuracy on contact surfaces is less critical.

Other Riemann Solvers

While the NSA code implements the Osher and Van Leer methods described above, other Riemann solvers exist in the literature and are used in alternative CFD codes.

The fundamental challenge is computing α^k and λ^k efficiently and accurately. Several approaches are standard:

- **Godunov's method** [20]: solves the Riemann problem exactly via iterative methods (typically Newton-Raphson). All wave strengths and speeds are determined precisely. The flux is extracted from the exact solution at the interface. Exact but computationally expensive; used primarily in research codes and high-fidelity simulations.
- **Roe solver** [51]: linearizes the Riemann problem at a Roe-averaged state. Instead of solving the full nonlinear system, it solves a *linear* Riemann problem exactly. The Roe average is constructed so that the linearization is consistent with the original system. Computationally efficient and widely used in production codes; excellent for shock capturing.
- **HLL solver** [26]: an approximate solver using only the fastest left-moving (S_L) and fastest right-moving (S_R) wave speeds. Does not resolve intermediate states. Very economical and robust, but loses accuracy on contact discontinuities.
- **HLLC solver** [59]: improves HLL by restoring the contact surface with an additional intermediate wave. Excellent balance of robustness and accuracy.

Each solver makes different trade-offs between accuracy and computational cost. For reference, the Roe solver is often preferred in production CFD codes: it is robust, relatively fast, and produces accurate shock-capturing behavior. However, the Osher and Van Leer methods implemented in NSA provide superior properties for the specific hypersonic applications considered in this work.

3.3.3 Viscous Flux Discretization

Stress Tensor and Heat Flux

The viscous fluxes arise from the stress tensor and heat conduction. For a flow in the x-direction, they are written as:

$$\mathbf{F}_v = \begin{pmatrix} 0 \\ \tau_{xx} \\ \tau_{xy} \\ \tau_{xz} \\ u\tau_{xx} + v\tau_{xy} + w\tau_{xz} + \kappa \frac{\partial T}{\partial x} \end{pmatrix} \tag{3.20}$$

where the stress tensor components are defined by [4]:

$$\tau_{ij} = \mu \left(\frac{\partial u_i}{\partial x_j} + \frac{\partial u_j}{\partial x_i} \right) + \lambda \left(\nabla \cdot \mathbf{u} \right) \delta_{ij} \tag{3.21}$$

Here, μ is the dynamic viscosity, λ the second viscosity coefficient (related to bulk viscosity via the Stokes hypothesis), δ_{ij} the Kronecker delta, and κ the thermal conductivity [60]. Unlike convective fluxes, which exhibit wave-like propagation and can produce discontinuities, viscous fluxes are fundamentally diffusive in nature. They smooth gradients and dissipate kinetic energy, increasing entropy.

Gradient Computation and Face Averaging

The key challenge in finite volume discretization of viscous terms is computing gradients of velocity and temperature at cell faces from cell-average values. The standard approach uses the divergence theorem to compute gradients at cell centers, then performs arithmetic averaging at faces [33].

At each cell center, the gradient is computed via:

$$\left(\frac{\partial u_i}{\partial x_j}\right)_{\text{cell}} = \frac{1}{V} \oint_{\partial V} u_i \, n_j \, dS \tag{3.22}$$

Once gradients are known at the left and right cells bounding a face, they are averaged:

$$\left(\frac{\partial u_i}{\partial x_j}\right)_{\text{face}} = \frac{1}{2}\left[\left(\frac{\partial u_i}{\partial x_j}\right)_L + \left(\frac{\partial u_i}{\partial x_j}\right)_R\right] \tag{3.23}$$

The stress tensor and heat flux are then evaluated at the face using these averaged gradients. This approach is second-order accurate on general unstructured grids and is the standard practice in production finite volume codes [4]. The arithmetic averaging preserves the symmetry of the stress tensor and ensures stability in the diffusive step.

3.4 Spatial Reconstruction and TVD Limiting

3.4.1 Motivation and Monotonicity

Cell-centered finite volume methods with first-order (piecewise constant) reconstruction are stable and monotone but excessively diffusive, particularly for resolving boundary layers and contact discontinuities [60]. Higher accuracy requires reconstruction of primitive variables (p, u, v, w, T) (or conservative variables) at each cell face prior to flux evaluation.

The simplest higher-order approach is piecewise linear reconstruction [3]:

$$\mathbf{U}(x) = \mathbf{U}_i + (\nabla \mathbf{U})_i \cdot (x - x_i) \tag{3.24}$$

Evaluating this at the left and right boundaries of a cell gives the left and right states for the Riemann solver. However, linear reconstruction without modification is prone to creating spurious oscillations near discontinuities (Gibbs phenomenon) [60].

Total variation diminishing (TVD) schemes [68] bound the total variation:

$$\mathrm{TV}(\mathbf{U}^{n+1}) \leq \mathrm{TV}(\mathbf{U}^n) \tag{3.25}$$

preventing the growth of oscillations while maintaining accuracy in smooth regions [33].

3.4.2 Slope Limiting Techniques

TVD schemes employ limiters that reduce the slope in regions of rapid variation [68]:

$$(\nabla \mathbf{U})_i^{\text{limited}} = \phi(r_i)(\nabla \mathbf{U})_i^{\text{smooth}} \tag{3.26}$$

where r_i is a gradient ratio measuring smoothness, and $\phi(r)$ is a limiter function satisfying bounds to ensure TVD. Common choices include [60]:

- **Minmod** (most restrictive):

$$\phi(r) = \max(0, \min(1, r)) \tag{3.27}$$

- **Van Leer** (balanced):

$$\phi(r) = \frac{r + |r|}{1 + |r|} \tag{3.28}$$

- **Superbee** (least restrictive):

$$\phi(r) = \max(0, \min(1, 2r), \min(2, r)) \tag{3.29}$$

The MUSCL (Monotone Upstream-Centered Schemes for Conservation Laws) approach [62] systematically applies these limiters to reconstruct states at cell faces. For each face, left and right states are reconstructed [25]:

$$\mathbf{U}_{i+1/2}^L = \mathbf{U}_i + \frac{1}{2}\phi(r_i)(\mathbf{U}_{i+1} - \mathbf{U}_i) \tag{3.30}$$

$$\mathbf{U}_{i+1/2}^{R} = \mathbf{U}_{i+1} - \frac{1}{2}\phi(r_{i+1})(\mathbf{U}_{i+1} - \mathbf{U}_i) \tag{3.31}$$

These reconstructed states are then passed to the Riemann solver. The combination of second-order reconstruction (MUSCL) with TVD limiting and a Riemann solving yields a second-order shock-capturing scheme, the standard choice for hypersonic aerodynamic analysis [25].

3.5 Temporal Integration

3.5.1 Method of Lines and Semi-Discrete System

The finite volume discretization yields a system of ordinary differential equations:

$$\frac{d\mathbf{U}_i}{dt} = \mathcal{L}(\mathbf{U}_i) \tag{3.32}$$

where the spatial residual operator is:

$$\mathcal{L}(\mathbf{U}_i) = -\frac{1}{V_i}\sum_j \left[(\mathbf{F}_{c,j} - \mathbf{F}_{v,j}) \cdot \hat{\mathbf{n}}_j A_j\right] + \mathbf{S}_i \tag{3.33}$$

This approach, termed the **method of lines** [60], separates spatial and temporal discretization, allowing flexible time integration schemes to be applied independently of the spatial discretization order.

3.5.2 High-Resolution Temporal Integration

To achieve second-order accuracy in both space and time while maintaining stability near discontinuities, the NSA solver employs a **high-resolution scheme** based on piecewise linear reconstruction and time extrapolation. This approach is superior to simple forward Euler because it captures shock-dominated features without introducing spurious oscillations.

The method consists of three stages at each time step, following the Reconstruct-Evolve-Average (REA) paradigm:

Stage 1: Piecewise Linear Reconstruction

At the beginning of each time step, primitive variables are reconstructed using piecewise linear functions within each cell:

$$\mathbf{U}^{\text{lin}}(x, t^n) = \mathbf{U}_i^n + (\mathbf{U}_x)_i(x - x_i) \tag{3.34}$$

where $(\mathbf{U}_x)_i$ are slope estimates computed using **slope limiters**, which are discussed above. This reconstruction provides second-order spatial accuracy while preserving monotonicity.

Stage 2: Time Extrapolation at Cell Interfaces

To achieve second-order temporal accuracy, the reconstructed solution is evolved in time by a half time step $\Delta t/2$ before evaluating interface values. The time-evolved left and right states at interface $i + 1/2$ are:

$$\mathbf{U}_L^{n+1/2} = \mathbf{U}_i^n + (\mathbf{U}_x)_i \frac{\Delta x}{2} + \mathcal{L}(\mathbf{U}_i^n)\frac{\Delta t}{2} \tag{3.35}$$

$$\mathbf{U}_R^{n+1/2} = \mathbf{U}_{i+1}^n - (\mathbf{U}_x)_{i+1} \frac{\Delta x}{2} + \mathcal{L}(\mathbf{U}_{i+1}^n)\frac{\Delta t}{2} \tag{3.36}$$

The time-derivative $\mathcal{L}(\mathbf{U})$ is obtained from the quasi-linear form of the governing equations, using the limited slopes. These extrapolated states define the Riemann problem at each interface and ensure that the overall scheme achieves second-order temporal accuracy.

Stage 3: Riemann Problem Solution and Flux Evaluation

At each cell interface, an approximate Riemann problem is solved using the left and right extrapolated states $\mathbf{U}_L^{n+1/2}$ and $\mathbf{U}_R^{n+1/2}$. The resulting interface flux $\mathbf{F}_{i+1/2}$ is then used in the conservative update formula to advance the solution to time t^{n+1}.

3.5.3 The Courant-Friedrichs-Lewy (CFL) Condition

Stability of explicit time integration is governed by the **Courant-Friedrichs-Lewy (CFL) condition** [8, 33]. This condition emerges from the requirement that the numerical domain of dependence must contain the physical domain of dependence of the PDE. For a hyperbolic system, information propagates at maximum characteristic speed $\lambda_{\max} = \max_k |\lambda^k|$. For the compressible Navier-Stokes equations, the acoustic eigenvalue dominates:

$$\lambda_{\max} = \max(|\mathbf{u}| + a) \tag{3.37}$$

where $|\mathbf{u}|$ is the flow velocity magnitude and a is the speed of sound.

For explicit schemes with three-point spatial stencils, stability requires:

$$\lambda_{\max} \frac{\Delta t}{\Delta x} \leq \text{CFL} \tag{3.38}$$

where CFL is a scheme-dependent constant.

For first-order explicit schemes, CFL ≤ 1 [60]. Viscous terms introduce an additional diffusive constraint:

$$\Delta t \leq \frac{\Delta x^2}{\nu} \tag{3.39}$$

where $\nu = \mu/\rho$ is kinematic viscosity. However, for hypersonic flows with moderate grid resolution, the convective CFL constraint is typically much more restrictive, making the diffusive constraint non-binding.

In practice, adaptive time stepping computes:

$$\Delta t = \text{CFL} \min_i \frac{\Delta x_i}{\lambda_{\max,i}} \tag{3.40}$$

where the minimum is taken over all cells. For multidimensional hypersonic simulations, typical values are CFL $\sim$ 0.3-0.5 [3, 60]. The NSA solver computes this time step adaptively at each iteration, automatically adjusting based on local flow properties and mesh resolution.

3.5.4 Workflow for Each Time Step

At each iteration, the high-resolution TVD scheme executes:

1. Compute limited slopes $(\mathbf{U}_x)_i$ for all primitive variables using slope limiters (minmod or superbee);
2. Reconstruct piecewise linear solution within each cell (Eq. 3.34);
3. Evaluate spatial residuals $\mathcal{L}(\mathbf{U}_i^n)$ from convective, viscous, and source contributions;
4. Perform time extrapolation at all cell interfaces (Eqs. 3.35–3.36);
5. Solve Riemann problem at interfaces and compute numerical fluxes using the extrapolated states;
6. Compute stable time step Δt via the CFL constraint (Eq. 3.40);
7. Update cell-average variables;
8. Increment time $t^{n+1} = t^n + \Delta t$ and proceed to the next iteration.

This formulation achieves second-order accuracy in smooth regions, TVD stability near shocks, and efficient parallel implementation via domain decomposition, making it well-suited for hypersonic aerothermodynamic applications.

3.6 Boundary Conditions for Hypersonic Viscous Flows

3.6.1 Far-Field Conditions

At the outer boundary of the computational domain, far from the vehicle, the flow approaches the freestream state $\mathbf{U}_\infty = [\rho_\infty, \rho_\infty u_\infty, 0, 0, \rho_\infty E_\infty]^T$, where ρ_∞, u_∞, and T_∞ are prescribed based on the flight altitude, Mach number, and atmospheric model. The zeros in the momentum components indicate that the freestream is aligned with the x-axis by choice of coordinate system; for oblique flows, these would be replaced by the appropriate velocity components.

Characteristic boundary conditions are typically employed: waves approaching the boundary from the interior are computed using the Riemann solver and account for information propagating outward, while waves leaving the domain are extrapolated or set to freestream values [3]. This prevents spurious reflections of acoustic waves and maintains physical consistency at the domain boundary [60].

3.6.2 Wall Conditions

At solid surfaces, the no-slip boundary condition enforces [4]:

$$\mathbf{u}_{\text{wall}} = 0 \tag{3.41}$$

The density and temperature at the wall are determined by the specific thermal boundary condition. For an adiabatic wall, the heat flux normal to the wall is zero [4]:

$$\left.\frac{\partial T}{\partial n}\right|_{\text{wall}} = 0 \tag{3.42}$$

For an isothermal wall, the temperature is prescribed [3]:

$$T_{\text{wall}} = T_0 \tag{3.43}$$

The implementation involves ghost cells: at the first interior cell adjacent to the wall, boundary values are reconstructed to enforce the no-slip and thermal conditions [33]. The viscous stress at the wall is computed from the velocity gradient, yielding the wall shear stress (skin friction). Heat transfer is evaluated from the temperature gradient near the wall [4]. These quantities are essential for hypersonic aerothermodynamic predictions and provide crucial outputs for thermal protection system design.

3.6.3 Mesh Alignment and Near-Wall Treatment

For accurate resolution of boundary layers and shocks in hypersonic flows, the mesh topology is critical [4]. Best practices include:

- **Boundary layer padding:** fine, structured prism layers normal to the wall, with first-cell height chosen to achieve a target y^+ (dimensionless wall distance) [3]. For viscous flows, $y^+ < 1$ is necessary to resolve the viscous sublayer.
- **Shock alignment:** mesh lines aligned with shock waves reduce numerical dissipation and prevent spurious post-shock oscillations [60].
- **Growth ratios:** gradual expansion of cell sizes away from fine regions to avoid large aspect-ratio variations that introduce numerical errors [33].

These meshing considerations are implemented in the preprocessing step (geometry and mesh generation) but directly impact the accuracy of the numerical solution [4]. They are essential for the method to perform as designed and to achieve grid-independent solutions.

3.7 Integration with Real Gas Effects and Source Terms

3.7.1 Real Gas Equation of State

The system is closed by an equation of state relating pressure, density, and temperature [4]. For an ideal gas:

$$p = \rho R T \tag{3.44}$$

For real gases (prevalent in hypersonic entry regimes), corrections account for molecular interactions [4]:

$$p = \rho R T Z(T, \rho) \tag{3.45}$$

where Z is the compressibility factor, tabulated or computed from intermolecular potential models. The internal energy is also real-gas dependent [4]:

$$e = c_v(T)T + e_0(T) \tag{3.46}$$

where $e_0(T)$ represents deviations from ideal gas behavior. During the solution update, once new conservative variables $\mathbf{U}^{n+1} = [\rho, \rho u, \rho v, \rho w, \rho E]^T$ are computed, the pressure and temperature are retrieved via the equation of state and thermodynamic relations [3]:

$$T = T(e, \rho), \quad p = p(T, \rho) \tag{3.47}$$

This reversal (from E to T) must be done carefully to avoid Newton-Raphson divergence, particularly at high temperatures [4]. Thermodynamic libraries or fast lookup tables are typically employed to ensure efficiency.

3.7.2 High-Temperature Nonequilibrium Effects

In the hypersonic regime (Chapter 2.3), vibrational excitation, molecular dissociation, and ionization occur. The internal energy comprises multiple components [4]:

$$e = e_{\text{trans}} + e_{\text{rot}} + e_{\text{vib}} + e_{\text{elec}} \tag{3.48}$$

If these modes are not in thermal equilibrium, separate energy equations may be required. For the purposes of this chapter's discretization, the approach is the same [60]: each energy equation is discretized as a conservation law, with energy exchange between modes appearing as source terms in $\mathbf{S}$.

3.8 Summary: The Complete Algorithm

The practical implementation of a compressible Navier-Stokes CFD solver for hypersonic flows integrates all components in a coherent framework [60]:

1. **Initialization:** set initial flow field from freestream conditions or restart file. Compute thermodynamic properties via equation of state [4].
2. **Gradient computation:** using divergence theorem, compute velocity and temperature gradients at cell centers [33].
3. **Reconstruction:** apply TVD limiting to reconstruct conservative or primitive variables at each cell face (MUSCL) [62].
4. **Convective flux:** for each face, reconstruct left and right states and solve the Riemann problem (via Osher solver or equivalent) to extract convective fluxes [60].
5. **Viscous flux:** compute viscous fluxes via arithmetic averaging of gradients and evaluation of stress tensor and heat flux [4].
6. **Residual accumulation:** sum all face fluxes and source terms to form the right-hand-side of the ODE system [33].
7. **Time stepping:** advance solution via a second-order method with adaptive time step controlled by CFL condition [60].
8. **Convergence check:** monitor residuals. If converged (or maximum iterations reached), output solution and post-process (extract surface pressures, heat fluxes, etc.). Otherwise, repeat from step 2 [3].
9. **Source terms and boundary updates:** At each time step, update source terms (radiative heating, chemical reactions) and re-enforce boundary conditions [4].

The result is a robust, second-order accurate (in smooth regions), shock-capturing scheme suitable for hypersonic aerodynamic and aerothermal analysis [60, 4]. The methodology is independent of specific gas composition, thermodynamic model, or equation of state, making it applicable across the range of hypersonic flow regimes relevant to entry vehicle design. The separation of convective and viscous treatments allows optimization of each: convective fluxes benefit from sophisticated Riemann solvers and TVD limiting, while viscous fluxes employ stable, second-order central differencing. Together, these techniques form the foundation of modern hypersonic CFD codes.

Chapter 4

NSA - Navier-Stokes and Ablation Solver

The NSA (Navier-Stokes and Ablation Solver) CFD solver is a finite volume code developed through a long-term collaboration between the Politecnico di Torino (DIMEAS) and Thales Alenia Space Italia, a leading aerospace company specializing in reentry vehicle design and thermal protection systems. The code originated approximately 15 years ago, driven by the need to perform accurate hypersonic aerodynamic and aerothermal predictions for atmospheric entry missions, including space vehicle reentry analysis, thermal protection system design, and aerodynamic characterization in the hypersonic regime.

The NSA solver represents a mature research tool, used extensively for feasibility studies and design optimization in space missions requiring detailed hypersonic flow analysis. Its development reflected the collaborative expertise of both academic researchers (theoretical foundations, numerical methods, validation) and industrial engineers (practical applicability, robustness requirements, integration with design workflows).

This chapter describes the rehabilitation and modernization of the NSA code, undertaken in the context of the present thesis. Specifically, it covers the code's architectural overview, the implementation of distributed-memory parallelization via Message Passing Interface (MPI) and verification on canonical test cases.

4.1 The Fortran Programming Language in CFD: Historical Context

The NSA solver is implemented in Fortran 90, a choice that reflects both historical development practices and contemporary best practices in computational fluid dynamics. To understand this choice, it is instructive to examine the role of Fortran in scientific computing, particularly for high-performance codes.

Fortran was originally developed by IBM and released in 1956 as the first widely adopted high-level programming language designed specifically for scientific and numerical computing. Over decades, it became the language of choice for large-scale scientific simulations across multiple disciplines: numerical weather prediction, finite element analysis, computational fluid dynamics, plasma physics, geophysics, and computational

chemistry. This historical prominence was not accidental; rather, it reflected deliberate language design decisions and sustained compiler optimization efforts spanning more than 60 years.

The adoption of Fortran for CFD in particular became universal in both academia and industry. Major CFD codes, including OVERFLOW (NASA), VULCAN (NASA), and numerous other research and production solvers, are written in Fortran. Similarly, global weather and climate forecast models, which require simulation of incomparably larger computational domains than typical engineering applications, are predominantly implemented in Fortran. This ubiquity in mission-critical applications demonstrates both the reliability of the language for numerical work and the substantial investment in compiler optimization specifically targeting scientific computing.

When the NSA code was originally developed, Fortran (specifically Fortran 90 and later Fortran 2003) represented the standard choice for a new CFD solver targeting high-performance computing environments. This decision positioned the code favorably for deployment on university clusters and supercomputing facilities, where Fortran compiler infrastructure was mature and extensively optimized.

4.2 Workflow: From Geometry to Hypersonic Simulation

The NSA solver operates within a well-defined workflow connecting geometry definition, mesh generation, domain decomposition, numerical simulation, and post-processing. This section outlines the practical steps required to execute a hypersonic CFD analysis using the NSA code, including the supporting tools and data format conversions necessary to integrate with industry-standard software.

The complete workflow for NSA simulations comprises five main stages:

1. **Geometry and mesh generation** (GridPro)
2. **Mesh format conversion and domain decomposition** (LoadGrid)
3. **CFD simulation setup and execution** (NSA)
4. **Post-processing and visualization** (Tecplot)

Each stage is described in detail below.

4.2.1 Stage 1: Geometry and Mesh Generation via GridPro

Geometry definition and mesh generation are performed using GridPro, a commercial structured mesh generation tool widely adopted in aerospace engineering. GridPro provides an intuitive interface for:

- **Surface definition**: creation of vehicle geometry from CAD data.
- **Boundary surface assignment**: specification of boundary types and physical regions (e.g., solid walls, far-field boundaries, symmetry planes, shock-aligned surfaces).

- **Mesh topology**: definition of the mesh block structure, including number of blocks, block connectivity, and mesh distribution.
- **Mesh generation and refinement**: automatic and manual mesh refinement to achieve appropriate resolution for shock waves, boundary layers, and aerodynamic features.

The output of the GridPro mesh generation process is a structured mesh file in STARCD (STAR-CCM+) format, a widely used industry standard for unstructured and hybrid mesh representation. The STARCD format contains:

- Vertex coordinates and connectivity
- Cell definitions and boundary face markers
- Boundary condition tags
- Material region specifications

4.2.2 Stage 2: Mesh Conversion and Domain Decomposition via LoadGrid

The STARCD mesh format output from GridPro cannot be directly read by NSA. To bridge this gap, a dedicated pre-processor program, LoadGrid, has been developed in-house in Fortran to perform mesh format conversion and domain decomposition.

Mesh Format Conversion

LoadGrid reads the STARCD format mesh and converts it into the native NSA mesh format, handling:

- Vertex coordinate transformation and validation
- Cell connectivity re-indexing
- Boundary face identification and classification

This conversion ensures that geometric and topological information is preserved while adapting to NSA's internal data structures.

Domain Decomposition for Parallel Execution

For distributed-memory parallel execution (via MPI), the computational domain must be partitioned into multiple subdomains, each to be processed by a separate MPI rank (processor). LoadGrid performs this domain decomposition using domain partitioning algorithms that:

- Partition the global mesh into N_p sub-domains (where N_p is the target number of MPI processes)

- Minimize interprocess communication by grouping geometrically nearby cells
- Generate host cell regions for each process to facilitate flux computations at domain boundaries

The output of LoadGrid is a partitioned mesh in NSA format, with one mesh file per process, plus metadata files describing inter-process connectivity and ghost cell mappings. This enables the NSA solver to execute efficiently on distributed-memory HPC systems.

4.2.3 Stage 3: CFD Simulation Setup and Execution via NSA

With the partitioned mesh in hand, NSA is configured and executed. The user specifies:

- **Initial conditions**
- **Boundary conditions**
- **Physical models**
- **Numerical parameters**

NSA then advances the solution in time using the numerical methods described in Chapter 3, until steady-state (or quasi-steady-state for transient phenomena) is reached. Convergence is monitored via residual norms.

4.2.4 Stage 4: Post-Processing and Visualization via Tecplot

The PLT output from NSA is imported into Tecplot 360, a commercial post-processing and visualization suite. Tecplot enables:

- **Flow visualization**: streamlines, vector fields, iso-surfaces.
- **Surface plots**: skin friction lines, pressure distribution, heat flux maps on vehicle surface.
- **Quantitative analysis**: extraction of line/surface integrals, force and moment computation, boundary layer profiles.

This post-processing stage is critical for engineering interpretation: the raw CFD output (millions of numbers) is transformed into physically meaningful visualizations and quantitative metrics that inform vehicle design, thermal protection system sizing, and mission feasibility assessments.

4.2.5 Data Format Chain

The complete workflow involves four distinct data formats:

Stage	Format	Tool
Geometry & Meshing	STARCD (*.vrt, *.cel, *.bnd)	GridPro
Mesh Conversion	NSA Native Format	LoadGrid
CFD Simulation	NSA Native Format (in-memory)	NSA
Output & Visualization	PLT (Binary Tecplot)	NSA $\rightarrow$ Tecplot

Each format conversion preserves geometric and physical fidelity while adapting to tool-specific requirements and computational structures.

4.3 Code Rehabilitation and Development

4.3.1 Compiler Migration and Code Modernization

A significant portion of the work undertaken in this thesis was dedicated to rehabilitating the NSA code base to ensure compatibility with contemporary Fortran compiler technologies and updated library ecosystems. The original NSA code, developed circa 2010, was written to compile with compilers and libraries that have since undergone substantial evolution. This section documents the issues encountered, the solutions implemented, and the validation that confirmed the code's numerical robustness despite its dormancy.

Compiler Changes: From ifort to ifx (Windows)

On Windows platforms, the development environment historically employed Intel Fortran Compiler Classic (ifort), part of Intel's Parallel Studio. However, Intel has transitioned to a new LLVM-based compiler infrastructure, ifx (Intel Fortran Compiler), which became the default compiler in Intel oneAPI 2024 and is mandatory from oneAPI 2025 onward [28].

The transition from ifort to ifx introduced several compatibility issues:

- **Architectural constraints**: the ifx compiler only generates 64-bit binaries, eliminating support for 32-bit (IA-32) compilation. All NSA build configurations were adapted to target 64-bit architecture exclusively.
- **Floating-point model changes**: the floating-point behavior differs between ifort and ifx with respect to NaN handling. This necessitated review of code sections relying on floating-point exception handling to ensure numerical consistency.

The migration to ifx was completed successfully, with NSA now compiling and executing correctly under the new compiler.

Compiler Updates: gfortran on Linux and HPC Clusters

On Linux systems and HPC clusters, the open-source GNU Fortran compiler (gfortran) is the dominant choice. The gfortran compiler ecosystem has undergone continuous improvement and standards compliance updates since NSA's original development. The NSA code, originally developed against gfortran circa 2010, required updates to compile cleanly with modern gfortran versions:

- **Implicit interface warnings**: modern gfortran flags implicit procedure interfaces and undeclared variables more strictly than older versions. NSA required addition of explicit `IMPLICIT NONE` statements and interface blocks in several modules to satisfy these warnings.
- **Variable declaration requirements**: certain variables in the original code were not explicitly declared, relying on Fortran's implicit typing rules. While these continued to function, modern compiler standards and best practices recommend explicit declaration. Several hundreds of variable declarations were added throughout the codebase to maintain compatibility with strict compilation modes.

Code Corrections

Following compiler migration, library updates, and variable declaration additions, a thorough code review was conducted to identify and correct any latent issues that could affect numerical correctness or stability. The following categories of corrections were implemented:

- **Minor logic corrections**: in isolated locations, small corrections were made to code logic to ensure correctness (e.g., fixing loop boundary conditions or refactoring unclear conditional logic). These changes were minimal and did not alter the fundamental numerical scheme.
- **Array bounds checking**: some array accesses were modified to ensure proper indexing and prevent out-of-bounds errors, particularly in sections handling mesh data structures.
- **Consistent use of precision**: the code was audited to ensure consistent use of floating-point precision (single vs double) across all modules, reducing the risk of numerical inconsistencies.
- **General debugging**: various minor bugs (uninitialized variables, incorrect format specifiers in I/O statements) were identified and corrected.

In summary, the rehabilitation process confirmed that NSA is a robust, mathematically sound CFD solver that required modernization of its build infrastructure and compiler compatibility but no fundamental algorithmic overhaul.

4.4 MPI Implementation

The original NSA code executed serially on a single processor, but had inside the MPI call to be executed on multiple processors.

While single processor was acceptable for research and small-scale feasibility studies, modern applications involving large domains (millions to hundreds of millions of cells) and high resolution in boundary layers and shock regions demand distributed-memory parallelization. This section describes the implementation of Message Passing Interface (MPI) based parallelization [35].

4.4.1 Motivation for Distributed-Memory Parallelization

Computational fluid dynamics simulations in the hypersonic regime are characterized by:

- **Large mesh sizes**: accurate prediction of aerodynamic and aerothermal quantities requires fine resolution near the vehicle surface (boundary layers) and near shock waves. A typical 3D simulation for a reentry vehicle geometry contains 5 to 50 million cells, and research simulations may exceed 100 million cells.
- **Compute-intensive kernel**: the flux computation at each cell interface involves Riemann solver evaluation, which is numerically intensive. With explicit time stepping, the entire flux calculation must be repeated at each time step for convergence.
- **Serial performance limitations**: modern CPU clock speeds have plateaued at 3–4 GHz. Single-threaded serial execution cannot leverage multicore processors effectively. A simulation on a single core may require weeks or months to converge, making design iteration impractical.

Distributed-memory parallelization via MPI addresses these challenges by partitioning the computational domain among multiple processing elements (nodes), enabling:

- **Scalability**: computational work scales linearly (in the ideal case) with the number of processors.
- **Memory distribution**: the total memory requirement is distributed across multiple nodes, enabling simulation of problems too large for a single node's RAM.
- **Time-to-solution reduction**: a simulation that requires 1000 hours on a single core can be completed in 10 hours using 100 cores (assuming good scaling).

4.4.2 Message Passing Interface: Fundamentals and Architecture

The Message Passing Interface (MPI) is an open standard specification for distributed-memory parallel computing, first released in 1994 and continuously updated. MPI provides a portable, vendor-independent programming model for implementing parallel applications on distributed-memory systems.

MPI Machine Model

The MPI machine model assumes:

- **Distributed memory**: each processor has its own private memory address space. No shared memory exists between processors (unlike OpenMP, which assumes shared memory on a single multicore node).
- **Message passing**: data is exchanged between processors by explicit message passing-one process sends a message, another receives it. The underlying communication network (Ethernet, InfiniBand, etc.) handles message delivery.
- **Process abstraction**: each MPI process executes the same code (SPMD: Single Program, Multiple Data) and is identified by a unique rank (0 to N-1, where N is the total number of processes).

This model is general and applies to any parallel machine: from a single multicore workstation (where multiple processes run on cores connected by shared memory) to a large HPC cluster (where processes run on distributed nodes connected by a network).

MPI Communication Paradigm

MPI provides two primary communication mechanisms:

- **Point-to-point communication**: one process sends data to a specific other process. MPI provides both blocking (synchronous) and non-blocking (asynchronous) variants. In blocking communication, the sending process is suspended until the message is received; in non-blocking communication, the sender continues and checks for completion later.
- **Collective communication**: all processes in a communicator (group) participate in a coordinated operation. Examples include:
  - *Broadcast*: one process sends the same data to all others.
  - *Reduction*: data from all processes is combined (e.g., sum, max, min) and result is sent to one process.
  - *Allgather*: each process sends data to all others (each process collects data from all).

4.4.3 Domain Decomposition for CFD: Spatial Partitioning

The key to parallelizing NSA via MPI is domain decomposition: partitioning the global computational domain into N_p non-overlapping subdomains, one per MPI process. Each process computes the solution on its local subdomain and exchanges boundary data (via MPI messages) with neighboring processes.

Domain Partition Strategy

The NSA code uses a domain partitioning approach:

- **Geometric partitioning**: the computational domain is partitioned based on spatial location. Neighboring cells (those sharing a face or vertex) that belong to different processes define process boundaries.
- **Communication minimization**: the number of cell faces (interfaces) between different partitions determines inter-process communication volume. Partitions should be shaped to minimize this surface-area-to-volume ratio.
- **Load balancing**: each partition should contain approximately the same number of cells to ensure equal computational load across processes.

The LoadGrid pre-processor employs METIS [30] for domain decomposition, utilizing multilevel recursive bisection to satisfy communication minimization criteria.

Ghost Cells

At process boundaries, each process maintains ghost cells-copies of cells belonging to neighboring processes. This structure enables local, independent computation.

For a cell i in process p that requires flux computation at a face shared with a ghost cell (belonging to process q), the Riemann solver uses the local cell state and the ghost cell state. The ghost cell state must be synchronized from process q before flux computation.

The MPI communication pattern is:

1. **Pack**: each process packs primitive variables (density, pressure, velocity, temperature, etc.) from cells on its boundaries into message buffers.
2. **Send**: each process sends its boundary cell data to neighboring processes via MPI point-to-point or asynchronous (non-blocking) sends.
3. **Receive**: each process receives boundary data from neighbors into ghost cell buffers via corresponding receives.
4. **Unpack**: data from message buffers is unpacked into ghost cells.

This communication occurs at each time step, before flux computation. For efficient MPI implementations, non-blocking communication is employed: sends and receives are initiated, computation on interior cells (not requiring boundary data) proceeds, and then the process waits for communication to complete before accessing ghost cell data.

4.4.4 Parallelization Considerations

Load Balancing

If the domain decomposition is unbalanced (for example partition i has 10% more cells than others), processes with fewer cells complete their computation earlier and enter an

idle wait state, degrading parallel efficiency. For static decomposition (domain partition does not change during simulation), load imbalancing is inherent to the mesh geometry and partition algorithm.

Communication vs Computation Ratio

MPI communication has latency and bandwidth costs. For efficient parallelization, the computation time should significantly exceed communication time. This ratio is called the surface-to-volume ratio: if the partition surface (process boundaries) is large relative to the volume (cell count) in the partition, communication dominates and parallel efficiency degrades.

For large partitions (millions of cells per process), the surface-to-volume ratio is favorable, and communication overhead is minimal. For small partitions (thousands of cells per process), communication overhead can dominate, reducing efficiency.

Synchronization Points

Collective operations (global reductions for convergence monitoring, I/O synchronization) introduce synchronization points where all processes must wait for the slowest process. Frequent synchronization degrades parallel efficiency.

4.5 NSA Code Capabilities

The NSA solver is a highly modular and configurable code, designed to accommodate a wide range of hypersonic flow scenarios through compile-time preprocessing options. This section documents the principal capabilities and customization options available when building the NSA executable, enabling users to tailor the code to their specific physical and computational requirements.

4.5.1 Spatial Dimensionality and Domain Characteristics

NSA supports simulations across multiple spatial dimensions and symmetry configurations:

- **Spatial dimensionality**: one dimensional (1D), quasi one dimensional (quasi-1D), two dimensional (2D), and three dimensional (3D) simulations. Lower dimensional modes reduce memory requirements and wall-clock time, making them suitable for preliminary design studies and validation against canonical benchmarks.

- **Axisymmetric flow**: option to enforce axisymmetry (2D grid representing a 3D body of revolution). This reduces the computational domain to a 2D meridional plane while maintaining three-dimensional physics through source terms that account for the omitted azimuthal direction.

4.5.2 Numerical Discretization Methods

Spatial Accuracy

- **Reconstruction order**: first-order (piecewise constant) or second-order (MUSCL with slope limiting) spatial reconstruction. First-order reduces accuracy but enhances stability for extremely challenging flows; second-order is the standard for production simulations.

- **Wall-adjacent reconstruction**: independent selection of reconstruction order in boundary-layer regions near walls. This allows first-order treatment (minimizing oscillations) near walls while maintaining second-order accuracy in the bulk flow.

Convective Flux Schemes

- **Flux Difference Splitting (FDS) - Osher**: Riemann solver upwind method (as detailed in Section 3.3.2), providing superior shock capturing accuracy. Default choice for hypersonic applications.

- **Flux Vector Splitting (FVS) - Van Leer**: alternative upwind method (as detailed in Section 3.3.2), offering robust stability and inherent positivity preservation at the cost of slightly reduced accuracy on contact discontinuities.

Shock Instability Mitigation

- **Carbuncle correction**: optional suppression of the carbuncle instability (numerical anomalies appearing as spurious post-shock perturbations on aligned grids). When enabled, additional numerical dissipation is applied selectively in regions of normal shocks to ensure smooth shock profiles without contaminating contact discontinuities or rarefaction fans.

4.5.3 Physical Models: Inviscid and Viscous Flows

Flow Regime Selection

- **Inviscid**: pure convective transport with no viscous terms. Suitable for shock-dominated regimes where viscous effects are negligible (low-altitude hypersonic entry with thin shock layers).

- **Viscous**: full compressible Navier-Stokes equations with viscous stress tensor and heat conduction. Required for accurate boundary-layer modeling and heat-transfer prediction.

Thermodynamic Model

- **Ideal gas**: equation of state $p = \rho RT$ with constant or temperature-dependent specific heats. Adequate for moderate-altitude (subsonic and low-supersonic) entry or research studies.

- **Real gas**: nonlinear equations of state with compressibility factors and real-gas corrections to internal energy, accommodating high-temperature effects where molecular interactions become significant. Essential for space-vehicle reentry (10+ km/s entry speed, stagnation temperatures exceeding 10,000 K).

Turbulence Modeling

- **Laminar flow**: no turbulence model, solution represents laminar flow. Most common for hypersonic entry vehicles, where thin shock layers and rapid acceleration tend to suppress transition to turbulence.

- **Spalart-Allmaras turbulence model** [54]: one-equation RANS turbulence model originally designed for aerospace wall-bounded flows. Currently implemented in NSA but marked as obsolete and requiring modernization and validation. Not recommended for new production simulations without thorough validation.

4.5.4 Chemical Composition and Thermochemical Nonequilibrium

NSA provides extensive flexibility in modeling chemical reactions and excited-state populations, essential for hypersonic reentry in planetary atmospheres.

Species and Elemental Composition

- **Custom chemical mixtures**: user selection of arbitrary number of chemical species and constituent elements. The code maintains stoichiometric constraints and elemental conservation throughout the simulation.
- **Equilibrium vs nonequilibrium modes**: for each species, selection of whether the population follows local thermodynamic equilibrium (LTE) or is computed dynamically as a nonequilibrium species. Similarly, for molecular species, selection of whether vibrational or electronic states are in equilibrium or nonequilibrium.

Vibrational Models

- **Harmonic oscillator representations**:
  - *Infinite*: classical quantum harmonic oscillator with infinite energy levels; simplest and most commonly used.
  - *Truncated*: finite number of excited vibrational levels; appropriate for moderate temperatures where high-energy states become negligible. Not implement yet.
  - *Anharmonic*: corrections to harmonic model accounting for energy-level nonlinearity at extreme temperatures.

Chemical Reaction Source Terms

- **Forward reaction rate coefficient**:
  - *Arrhenius form*: standard $k_f = AT^{\beta}e^{-E_a/RT}$ temperature-dependent kinetics.
  - *Bari/CAST 2007*: empirical correlations tuned to experimental data for hypersonic air chemistry.
- **Equilibrium constant**: fitting models for $K_{eq}(T)$ include:
  - *Park 1985* [45]: classical empirical fit for air chemistry in the context of hypersonic nonequilibrium flows.
  - *Park 2001* [47]: updated Park model with improved temperature coverage for reentry flows.
  - *Bari/CAST 2007*: empirical correlations for reentry air at extreme conditions.
- **Vibrational relaxation source**:
  - *Millikan-White with Park Correction* [36]: semi-empirical model for vibrational energy transfer in molecular collisions, with Park's correction factors for improved accuracy in nonequilibrium conditions.
  - *Bari/CAST 2007*: empirical relaxation model.

Chemical-Vibrational Coupling

- **Uncoupled**: chemical and vibrational relaxation modeled independently (faster to compute, suitable for weakly-coupled regimes).
- **Coupled - Bari/CAST 2007**: empirical model accounting for coupling between chemical reactions and vibrational energy exchange.
- **Coupled - Marrone-Treanor**: advanced coupling model accounting for vibrational-chemical energy exchange via state specific kinetics; not yet fully implemented.

4.5.5 Transport Coefficients and Mixture Models

Accurate prediction of viscosity, thermal conductivity, and diffusion coefficients is critical for boundary-layer and heat-transfer analysis. NSA implements models derived from kinetic theory and empirical correlations.

Collision Integral Models

- **Gupta model**: empirical correlation for collision integrals based on molecular theory; computationally efficient and widely used in aerospace CFD [23].
- **Wright model**: Alternative collision-integral formulation providing different temperature dependence [66].

Binary Diffusion Coefficients

- $\Omega_{1,1}$**-based fitting**: diffusion coefficients fitted to collision-integral data (tabulated $\Omega_{1,1}$) via Chapman-Enskog kinetic theory [7].
- $\bar{D}$**-based fitting**: alternative model.

Diffusion Models

- **Stefan-Maxwell equation** [34]: rigorous multicomponent diffusion model accounting for interactions among all species pairs; highest fidelity but computationally expensive. Solves coupled equations for diffusive fluxes driven by concentration gradients and pressure gradients.
- **Multicomponent detailed**: simplified treatment of Stefan-Maxwell equations with approximations [5].
- **Fick's law**: Simpler approximation using an effective mixture diffusion coefficient. User selects:
  - Mass-fraction gradients (classic formulation).
  - Mole-fraction gradients (alternative, sometimes more accurate for mixtures).

Viscosity and Thermal Conductivity Models

For multicomponent mixtures, transport coefficients are assembled from single-species values and mixture combination rules:

- **Viscosity**:
  - Fitted to $\Omega_{2,2}$ collision integral via Chapman-Enskog theory [7].
  - Alternatively, directly fitted to viscosity data.
- **Thermal conductivity**:
  - Fitted to $\Omega_{2,2}$ collision integral via Chapman-Enskog theory [7].
  - Alternatively, directly fitted to conductivity data.
- **Mixture combination rules**:
  - *Wilke rule* [65]: empirical formula for mixture viscosity and thermal conductivity; standard in CFD and computationally simple.
  - *Chapman-Enskog via determinant* [7]: rigorous kinetic theory approach solving for mixture viscosity via determinant formulation of coupled binary interactions.
  - *Chapman-Enskog via linear system* [7]: alternative implementation solving a linear system for mixture transport coefficients.
  - *Bari/CAST 2007*: model for hypersonic air mixtures base on experimental data.

4.5.6 Parallelization

- **Serial execution**: single-process mode for development, debugging, and small scale problems.
- **Distributed-memory parallelization**: MPI enabled execution on multicore nodes and HPC clusters, enabling large scale simulations (as discussed in Section 4.4).

4.5.7 Ablating Surface Treatment

NSA includes preliminary infrastructure for modeling ablating thermal protection system (TPS) surfaces, where material recession, chemical reactions, and surface recession couple with the boundary-layer flow. This capability is currently incomplete and requires further development for production use.

4.5.8 Runtime Control and Simulation Restart Capabilities

Beyond compile-time and start-up configuration, NSA provides flexible runtime control features enabling mid-simulation adjustments and efficient restart workflows:

MONITOR File Runtime Parameter Control

During an active simulation, users may modify input parameters (in `input.dat`) without stopping the code execution by editing a `MONITOR.txt` file. This file is polled periodically at designated computational checkpoints, allowing:

- **Time-integration parameters**: adjustment of CFL number, maximum iteration count, and convergence tolerance targets.
- **Output frequency**: modification of solution output intervals and solution snapshot frequency without code restart.
- **Convergence monitoring**: changes to residual calculation methods and convergence criterion metrics.

This runtime flexibility is particularly valuable for long-running simulations where preliminary convergence behavior may suggest mid-course adjustments to improve efficiency or resolve numerical difficulties.

Restart from Previous Solutions

NSA supports checkpoint-restart capability, allowing simulations to be resumed from previously computed solution snapshots. The workflow is:

1. At designated intervals, NSA writes complete solution snapshots to restart files, including all primitive variable, current iteration count, and time-stepping state.
2. A simulation may be terminated at any checkpoint or upon convergence achievement.
3. A new simulation may be initialized from a restart file, resuming time integration from the checkpoint state. This enables:
    - **Checkpoint safety**: protection against hardware failures or cluster job time limits; a simulation interrupted by external factors resumes from the last checkpoint rather than restarting from scratch.
    - **Parameter variation studies**: a baseline solution computed on one set of parameters can serve as the initial condition for simulations with modified physical conditions or parameters, accelerating convergence relative to cold-start from uniform freestream.

4.5.9 Summary: Compile-Time and Runtime Configuration

The extensive configurability of NSA at both compile-time and runtime reflects its design as a research tool: different physical regimes demand different algorithmic treatments and approximations. By offering:

- compile-time selection of physical and numerical models,
- runtime parameter adjustments,
- checkpoint-restart capability for efficient simulation workflows,

NSA enables users to:

1. Build executables optimized for specific applications.
2. Reduce unnecessary computation when certain physics is unimportant.
3. Facilitate iterative refinement workflows combining coarse-mesh exploration with fine-mesh validation.
4. Maximize robustness and fault tolerance on large-scale HPC systems via checkpoint restart safety.

In the production simulations presented in next chapter, specific compile-time options and restart strategies are selected to match the physical requirements and computational constraints of each test case, ensuring maximum fidelity while maintaining efficiency.

Chapter 5

Code Validation: RAM-C II at 61 km

In this chapter the numerical solver is validated against the RAM-C II flight experiment and the numerical analysis by Surzhikov [57]. The focus is on the trajectory point at 61 km altitude, where strong thermochemical non-equilibrium and partial ionization of air occur.

Two simulations are performed and compared with Surzhikov:

1. $T_w = 550\,\mathrm{K}$, non catalytic wall for all species, no explicit electron recombination at the wall, instead of the full electron recombination used by Surzhikov.
2. $T_w = 1000\,\mathrm{K}$, Park 7 species and 20 reaction model [47] instead of the 18 reaction model [46] used by Surzhikov, again with a fully non catalytic wall and no explicit electron recombination at the wall.

The chapter is structured to follow the complete workflow from geometry definition and mesh generation, through physical modelling, up to quantitative comparison of results.

5.1 Geometry Modelling and Computational Domain

5.1.1 CAD Reconstruction of RAM-C II

The RAM-C II vehicle is a spherically blunted cone. The CAD model used in this work was built starting from the geometric data reported in the Sun et al. paper [56]:

- Nose radius: $R_n = 0.1524\,\mathrm{m}$.
- Cone half–angle: $\theta = 9°$.
- Total forebody length considered: $L \approx 1.3\,\mathrm{m}$.

The geometry is assumed axisymmetric with zero angle of attack, allowing the use of a 2D axisymmetric formulation. The CAD model includes the spherical nose and the conical frustum along the generating line up to a truncation plane, as detailed below.

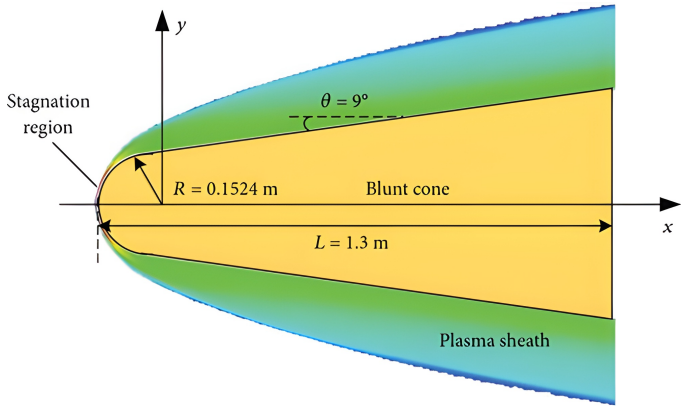

Figure 5.1. Geometry of the RAM-C II vehicle used for validation [56].

5.1.2 Truncation of the Afterbody and Wake

In the original RAM-C II configuration, the vehicle includes an aft section and a wake region downstream of the base. In the present work, the geometry is *intentionally truncated* at a plane located at the end of the conical forebody, and the wake is not modelled.

This modelling choice is motivated by the following considerations:

- At hypersonic speeds, the dominant phenomena for the present objectives (shock standoff, stagnation heating, and peak electron number density in the bow shock layer) are governed by the *forebody* flow.
- The wake region has negligible feedback on the bow shock structure and on the high-temperature, highly ionized layer in front of the vehicle, especially at the considered altitude of 61 km, where the density is low and the flow is strongly directed.
- Neglecting the wake significantly reduces the length of the computational domain and the total number of cells, thereby decreasing the computational cost without affecting the observables of interest.

This assumption is consistent with previous hypersonic studies where the wake is neglected for forebody focused analyses, provided that the outflow boundary is placed sufficiently downstream to avoid spurious reflections.

A schematic of the truncated geometry and the computational domain is reported in Fig. 5.2.

5.2 Grid Generation Strategy and Refinement Process

The generation of the computational mesh followed an iterative, physics-based strategy aimed at optimizing the resolution of flow gradients while minimizing computational cost. This process involved two distinct phases: a preliminary exploration phase and a final refinement phase.

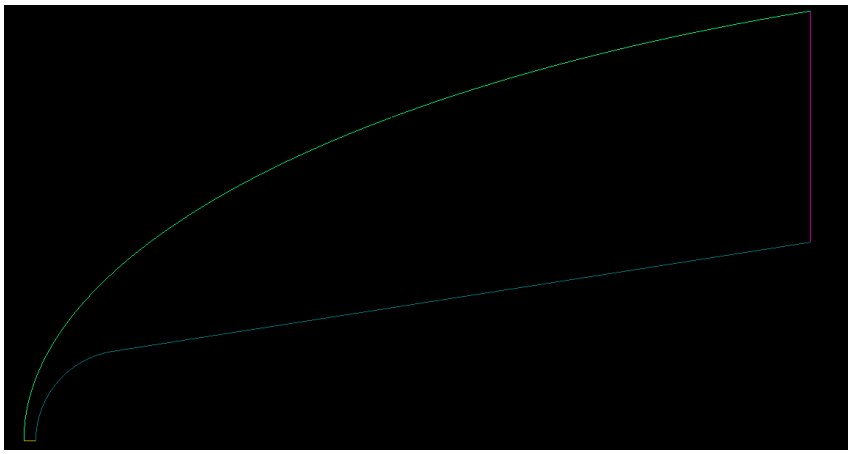

Figure 5.2. Schematic of the truncated RAM-C II computational domain, made in GridPro.

5.2.1 Preliminary Grid and Shock Identification

Initially, a preliminary coarse grid was generated over a conservatively large computational domain. The outer boundary of this domain was placed far upstream (approximately $2 \times L$ from the nose) and extended significantly in the radial direction. This choice was made to ensure that the bow shock would be fully contained within the domain regardless of the initial uncertainty about the shock standoff distance at 61 km.

A precursor simulation was run on this grid with moderate clustering parameters. The primary objectives of this step were:

1. To numerically identify the exact location and shape of the bow shock wave.

2. To obtain a first estimation of the wall shear stress τ_w distribution, necessary to calculate the required first-cell height (Δy_{wall}) for the condition $y^+ < 1$.

5.2.2 Domain Adaptation and Final Clustering

Based on the solution of the precursor simulation, the computational domain and the grid distribution were rigorously optimized for the final production runs.

Domain reduction (Shock-fitted approach): the outer boundary of the domain was explicitly repositioned to conform to the shape of the captured bow shock. The new inflow boundary was placed just a few centimeters upstream of the shock location. This "shock-fitted" domain reduction strategy allows for a significant increase in grid density within the shock layer without increasing the total number of cells, as fewer nodes are wasted in the freestream region where gradients are zero.

Wall clustering (y^+ control): using the shear stress values extracted from the preliminary run, the first-cell height was recalculated according to the standard definition of

the dimensionless wall distance:

$$\Delta y_{wall} = \frac{y^+ \mu_w}{\rho_w u_\tau} \tag{5.1}$$

where $u_\tau = \sqrt{\tau_w/\rho_w}$ is the friction velocity. The grid was regenerated with a strict constraint of $y^+ < 1$ along the entire wetted surface to fully resolve the viscous sublayer and the wall heat flux.

Shock resolution: regarding the discretization of the bow shock, explicit clustering of nodes in the vicinity of the shock wave was found to be unnecessary. Due to the high Mach number conditions, the shock standoff distance is small, placing the discontinuity in close proximity to the wall. Consequently, the high grid density already imposed in the wall-normal direction to resolve the thick thermal boundary layer provided, as a natural byproduct, sufficient spatial resolution across the entire shock layer. This background mesh density was deemed adequate to minimize numerical smearing and ensure a sharp capture of the post-shock temperature peak without the need for additional local refinement.

The final grid, resulting from this optimization process, consists of 158×91 cells and is shown in Figure 5.3.

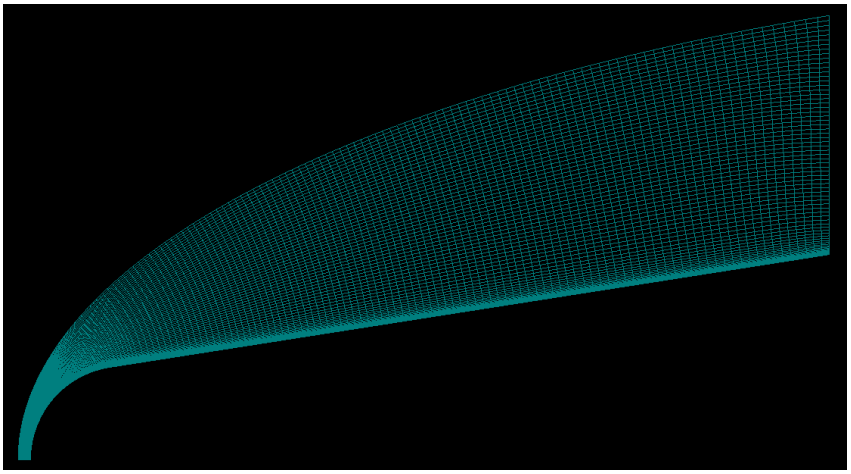

Figure 5.3. Final computational grid obtained after the refinement process.

5.3 Physical and Numerical Modelling

5.3.1 Freestream Conditions at 61 km

The freestream state for the validation point is taken from Surzhikov [57] and summarized in Table 5.1.

Table 5.1. Freestream conditions at $H = 61$ km for the RAM-C II trajectory point.

Parameter	Value
Velocity V_∞	7.50×10^3 m/s
Mach number M_∞	23.9
Temperature T_∞	244 K
Pressure P_∞	19.2 Pa

5.3.2 Thermochemical Non-Equilibrium Model

A two-temperature (T-T_v) description is adopted to model translational-rotational and vibrational-electronic energy modes separately. The gas mixture consists of seven species:

$$N_2,\ O_2,\ NO,\ N,\ O,\ NO^+,\ e^-.$$

Regarding the finite-rate chemical kinetics, two distinct reaction mechanisms were employed depending on the simulation case, in order to decouple the validation of the flow solver from the sensitivity to kinetic parameters:

- **Case 1:** the kinetic model was set to match the **18 reaction** (Table 5.2) scheme employed by Surzhikov [57]. This choice ensures consistency with the reference data, aiming to isolate the effects of the catalytic wall boundary conditions from potential discrepancies.
- **Case 2:** the chemistry was switched to an extended **20 reaction** Park mechanism (Table 5.3). The adoption of this different scheme in the sensitivity analysis allows for an assessment of the solution's robustness not only with respect to the wall temperature but also regarding the epistemic uncertainty inherent in the kinetic models, particularly for the associative ionization and recombination processes.

Table 5.2. Reaction mechanism parameters for the 18 reaction model (Case 1). Forward rate coefficients are computed as $k_f(T) = AT^n \exp(-E_a/T)$.

No.	**Reaction**	A $[(\mathrm{cm}^3/\mathrm{mol})^{n-1}/\mathrm{s}]$	n	E_a (K)
1	$O_2 + O_2 \rightleftharpoons 2O + O_2$	2.0×10^{21}	-1.5	60050
2	$O_2 + NO \rightleftharpoons 2O + NO$	2.0×10^{21}	-1.5	60050
3	$O_2 + N_2 \rightleftharpoons 2O + N_2$	2.0×10^{21}	-1.5	60050
4	$O_2 + O \rightleftharpoons 3O$	1.0×10^{22}	-1.5	60050
5	$O_2 + N \rightleftharpoons 2O + N$	1.0×10^{22}	-1.5	60050
6	$NO + O_2 \rightleftharpoons N + O + O_2$	5.0×10^{15}	0.0	76020
7	$NO + NO \rightleftharpoons N + O + NO$	1.1×10^{17}	0.0	76020
8	$NO + N_2 \rightleftharpoons N + O + N_2$	5.0×10^{15}	0.0	76020
9	$NO + O \rightleftharpoons N + 2O$	1.1×10^{17}	0.0	76020
10	$NO + N \rightleftharpoons 2N + O$	1.1×10^{17}	0.0	76020
11	$N_2 + O_2 \rightleftharpoons 2N + O_2$	7.0×10^{21}	-1.6	113900
12	$N_2 + NO \rightleftharpoons 2N + NO$	7.0×10^{21}	-1.6	113900
13	$N_2 + N_2 \rightleftharpoons 2N + N_2$	7.0×10^{21}	-1.6	113900
14	$N_2 + O \rightleftharpoons 2N + O$	3.0×10^{22}	-1.6	113900
15	$N_2 + N \rightleftharpoons 3N$	3.0×10^{22}	-1.6	113900
16	$N_2 + O \rightleftharpoons NO + N$	6.4×10^{17}	-1.0	38400
17	$NO + O \rightleftharpoons O_2 + N$	8.4×10^{12}	0.0	19450
18	$N + O \rightleftharpoons NO^+ + e^-$	8.8×10^{8}	1.0	33630

Table 5.3. Reaction mechanism parameters for the extended 20 reaction model (Case 2). Forward rate coefficients are computed as $k_f(T) = AT^n \exp(-E_a/T)$.

No.	**Reaction**	A $[(\text{cm}^3/\text{mol})^{n-1}/\text{s}]$	n	E_a (K)
1	$O_2 + O_2 \rightleftharpoons 2O + O_2$	2.0×10^{21}	-1.5	59360
2	$O_2 + NO \rightleftharpoons 2O + NO$	2.0×10^{21}	-1.5	59360
3	$O_2 + N_2 \rightleftharpoons 2O + N_2$	2.0×10^{21}	-1.5	59360
4	$O_2 + O \rightleftharpoons 3O$	1.0×10^{22}	-1.5	59360
5	$O_2 + N \rightleftharpoons 2O + N$	1.0×10^{22}	-1.5	59360
6	$NO + O_2 \rightleftharpoons N + O + O_2$	5.0×10^{15}	0.0	75500
7	$NO + NO \rightleftharpoons N + O + NO$	1.1×10^{17}	0.0	75500
8	$NO + N_2 \rightleftharpoons N + O + N_2$	5.0×10^{15}	0.0	75500
9	$NO + O \rightleftharpoons N + 2O$	1.1×10^{17}	0.0	75500
10	$NO + N \rightleftharpoons 2N + O$	1.1×10^{17}	0.0	75500
11	$N_2 + O_2 \rightleftharpoons 2N + O_2$	7.0×10^{21}	-1.6	113200
12	$N_2 + NO \rightleftharpoons 2N + NO$	7.0×10^{21}	-1.6	113200
13	$N_2 + N_2 \rightleftharpoons 2N + N_2$	7.0×10^{21}	-1.6	113200
14	$N_2 + O \rightleftharpoons 2N + O$	3.0×10^{22}	-1.6	113200
15	$N_2 + N \rightleftharpoons 3N$	3.0×10^{22}	-1.6	113200
16	$N_2 + O \rightleftharpoons NO + N$	5.7×10^{12}	0.42	42938
17	$NO + O \rightleftharpoons O_2 + N$	8.4×10^{12}	0.0	19400
18	$N + O \rightleftharpoons NO^+ + e^-$	5.3×10^{12}	0.0	31900
19	$N_2 + NO^+ \rightleftharpoons 2N + NO^+$	7.0×10^{21}	-1.6	113200
20	$O_2 + NO^+ \rightleftharpoons 2O + NO^+$	2.0×10^{21}	-1.5	59360

5.3.3 Wall Boundary Conditions

Surzhikov uses a hybrid wall model: non catalytic for neutral species, and fully catalytic (complete recombination) for charged particles. In NSA, at the moment, there is no built-in functionality to implement such a hybrid catalytic wall condition.

Therefore, both Case 1 and Case 2 use a **fully non catalytic wall** for *all* species, including ions and electrons:

$$\left.\frac{\partial Y_i}{\partial n}\right|_w = 0 \quad \forall i,$$

with fixed wall temperature T_w.

This modelling choice has two important implications:

1. It is *conservative* for blackout analysis: preventing electron recombination at the wall tends to overpredict the electron number density in the near wall region.

2. The main validation metric in this work is the *maximum* electron number density in the flow ($n_{e,\max}$) along the generatrix, which occurs in the high-temperature shock layer rather than at the wall. In that region, the solution is dominated by post shock enthalpy and finite rate chemistry, and is only weakly affected by the wall catalytic model, especially at 61 km.

5.4 Simulation Cases

5.4.1 Case 1

This case aims at reproducing as closely as possible the reference configuration of Surzhikov, apart from the wall chemistry:

- Freestream conditions as in Table 5.1.
- Wall temperature: $T_w = 550$ K.
- Park 18 reactions chemistry model.
- Fully non-catalytic wall.

5.4.2 Case 2

Case 2 is used to assess the sensitivity of the solution to the wall temperature.

- Same freestream conditions as Case 1.
- Wall temperature: $T_w = 1000$ K.
- Park 20 reactions chemistry model.
- Fully non-catalytic wall.

5.5 Results and Comparison

5.5.1 Flow Field and Shock Structure

The computed temperature and velocity fields for both cases show a detached bow shock ahead of the spherical nose, in good agreement with Surzhikov's [57] results. The truncation of the afterbody does not affect the forebody solution.

Temperature Contours

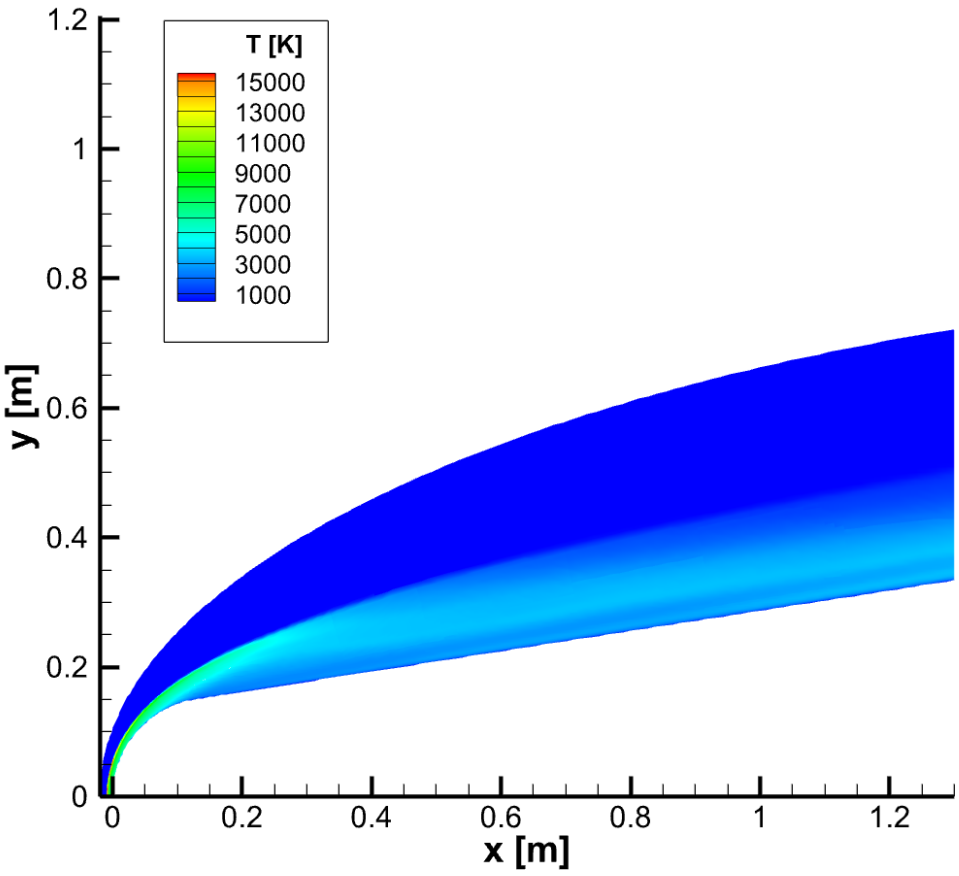

Figure 5.4. Temperature contour for Case 1.

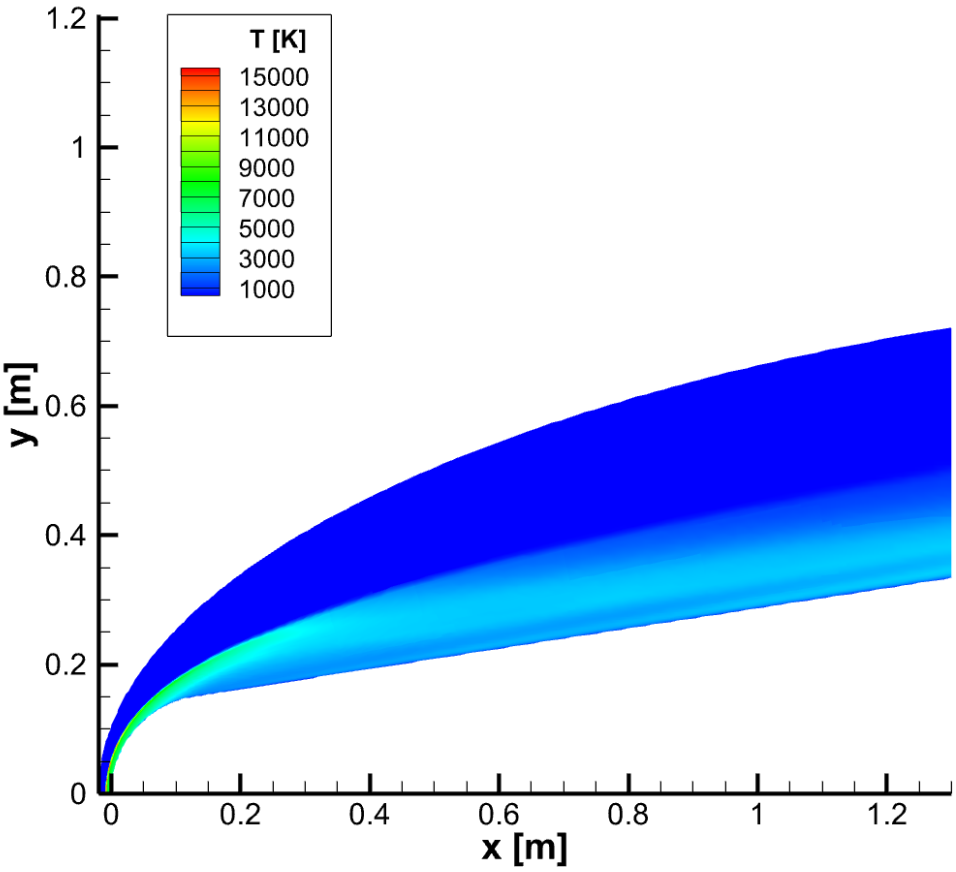

Figure 5.5. Temperature contour for Case 2.

Velocity Contours

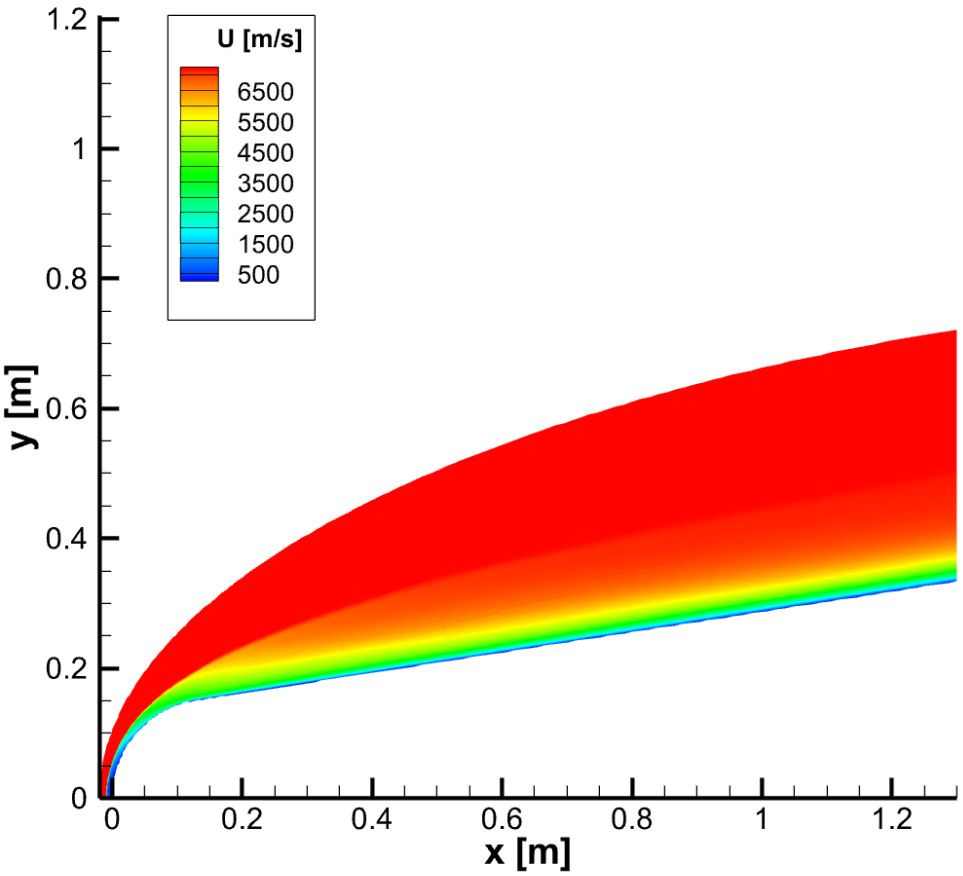

Figure 5.6. Velocity (along x) contour for Case 1.

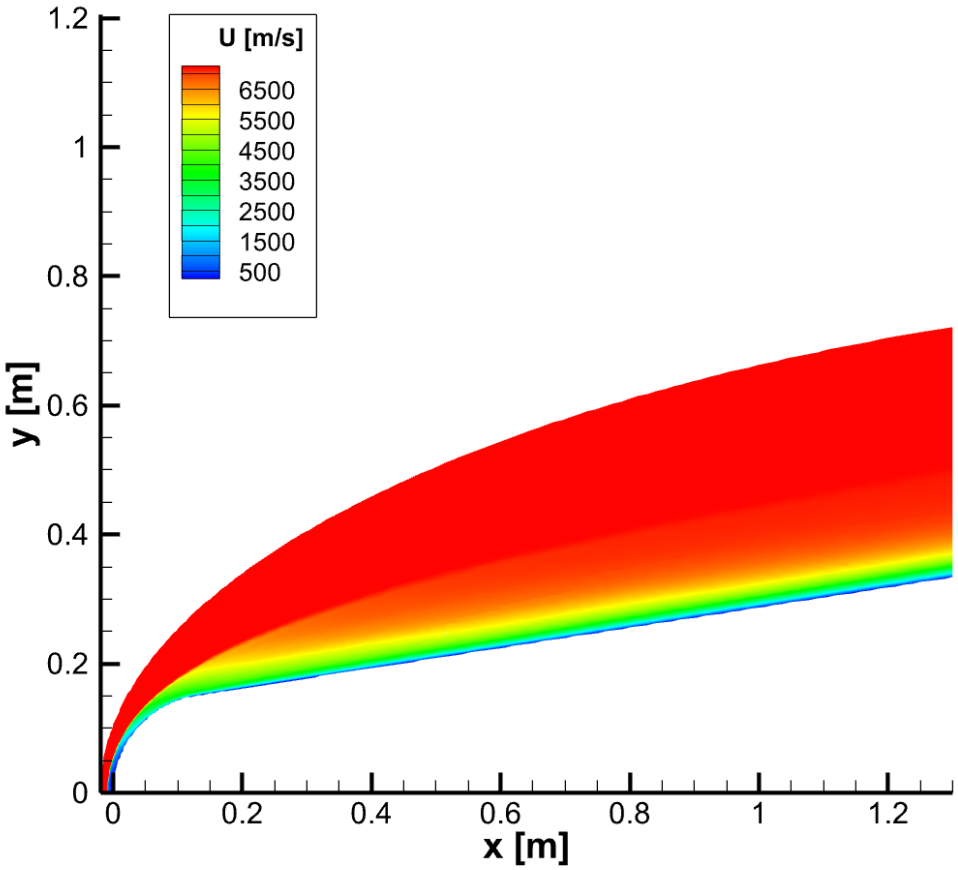

Figure 5.7. Velocity (along x) contour for Case 2.

Streamtraces

In the figures below, streamtraces are shown for both cases to illustrate the flow pattern around the forebody.

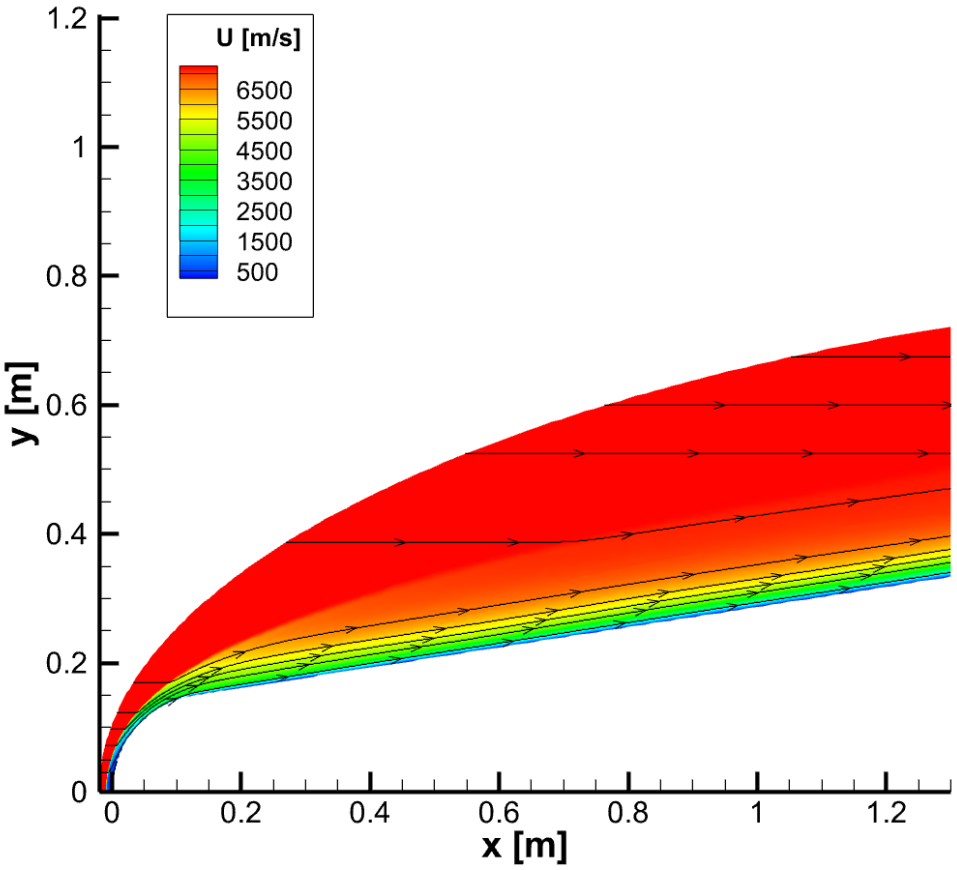

Figure 5.8. Streamtraces for Case 1.

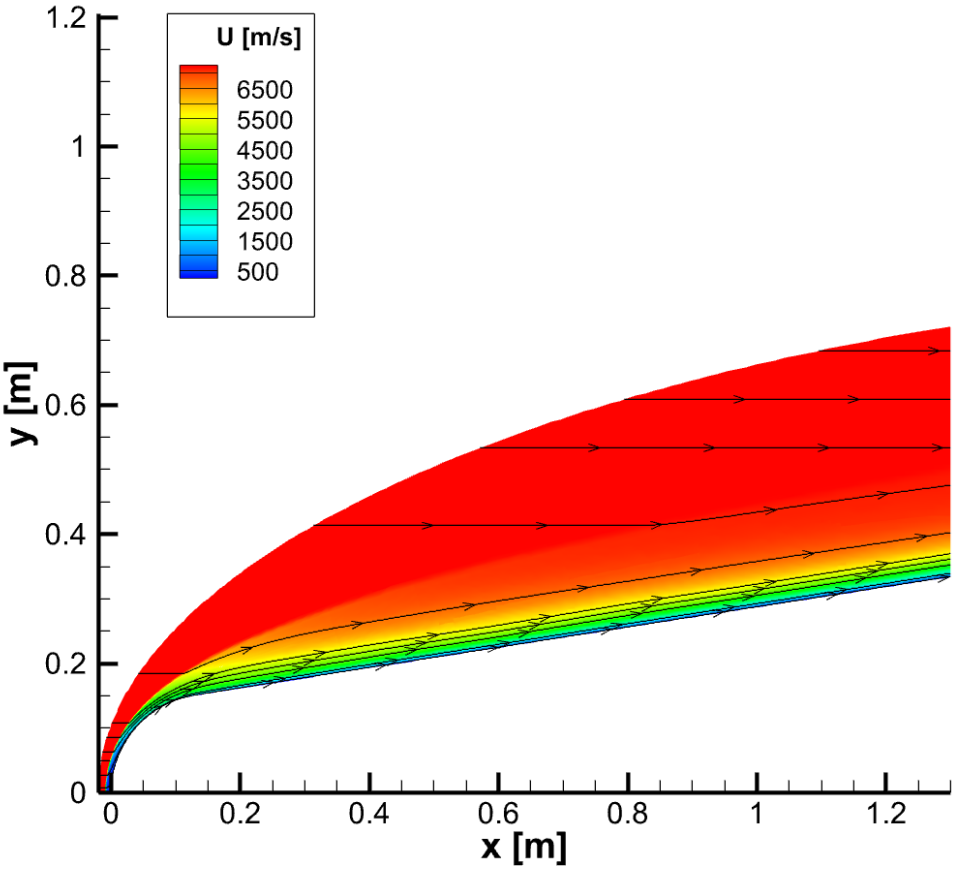

Figure 5.9. Streamtraces for Case 2.

5.5.2 Electron Number Density

The most relevant validation metric for hypersonic ionized flows is the electron number density n_e. In the figures below, the contours of n_e for both cases are shown.

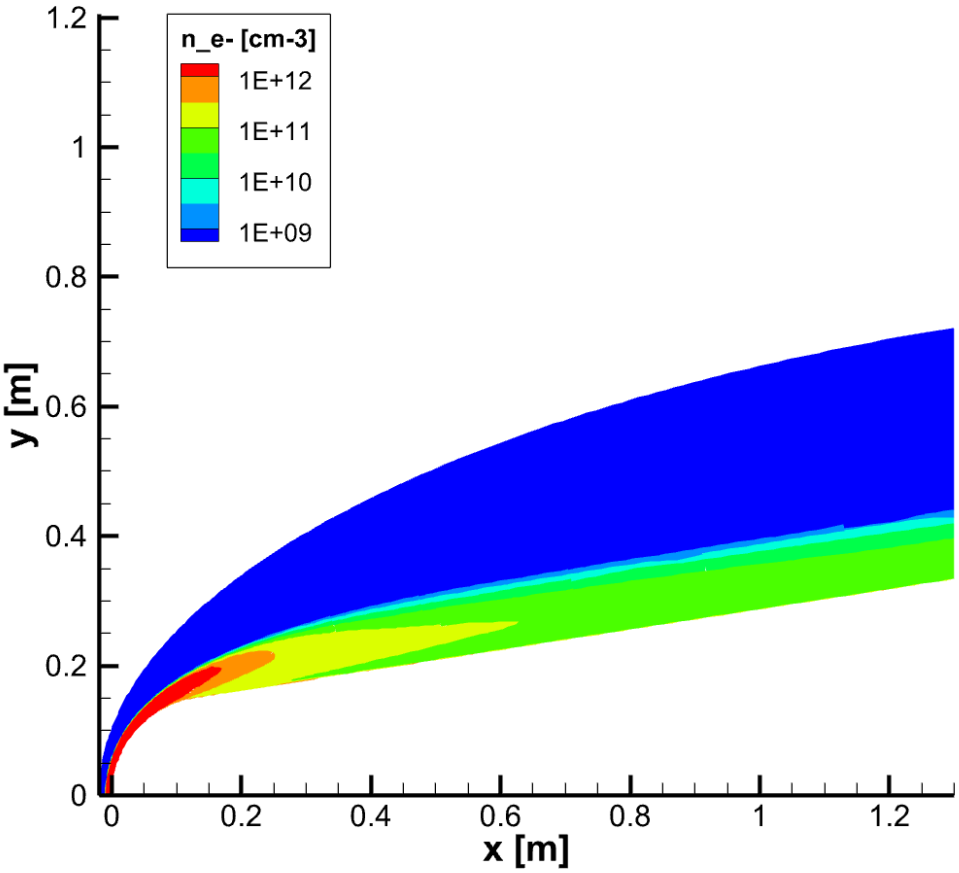

Figure 5.10. Electron number density contour for Case 1.

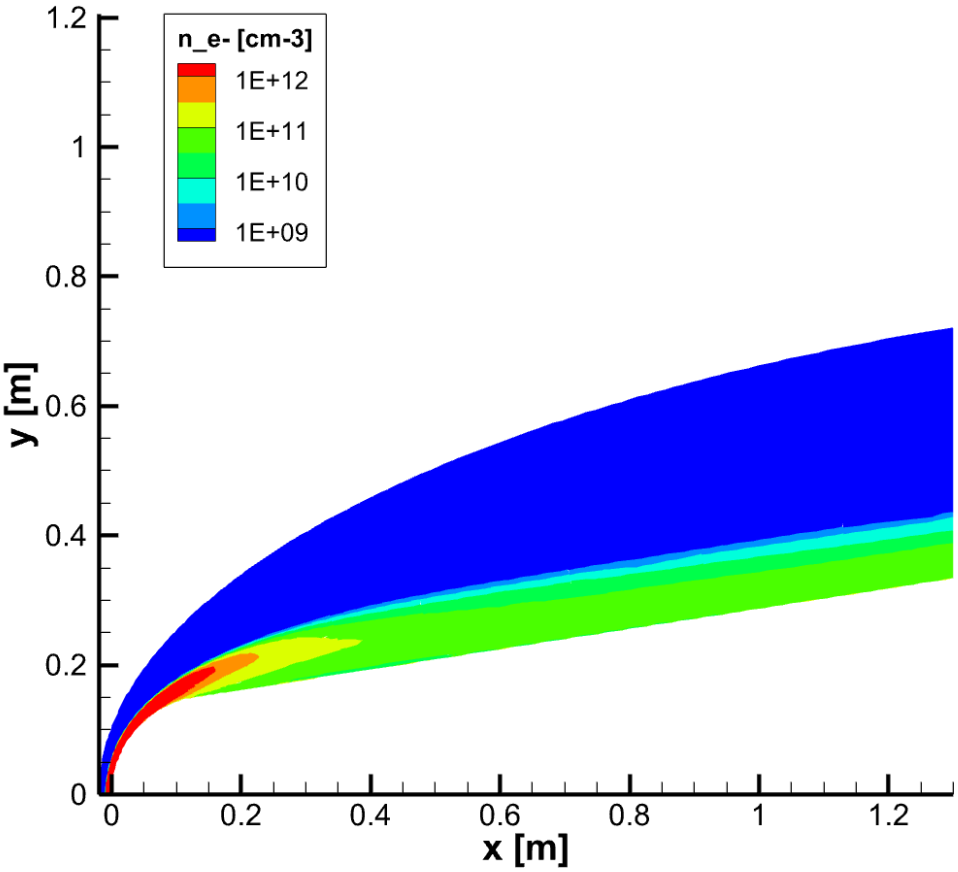

Figure 5.11. Electron number density contour for Case 2.

Following Surzhikov [57], the main validation quantity is the maximum electron number density along the generatrix. For each axial station x, the profile $n_e(x, y)$ is sampled and the maximum value is extracted:

$$n_{e,\max}(x) = \max_{y} n_e(x, y) \tag{5.2}$$

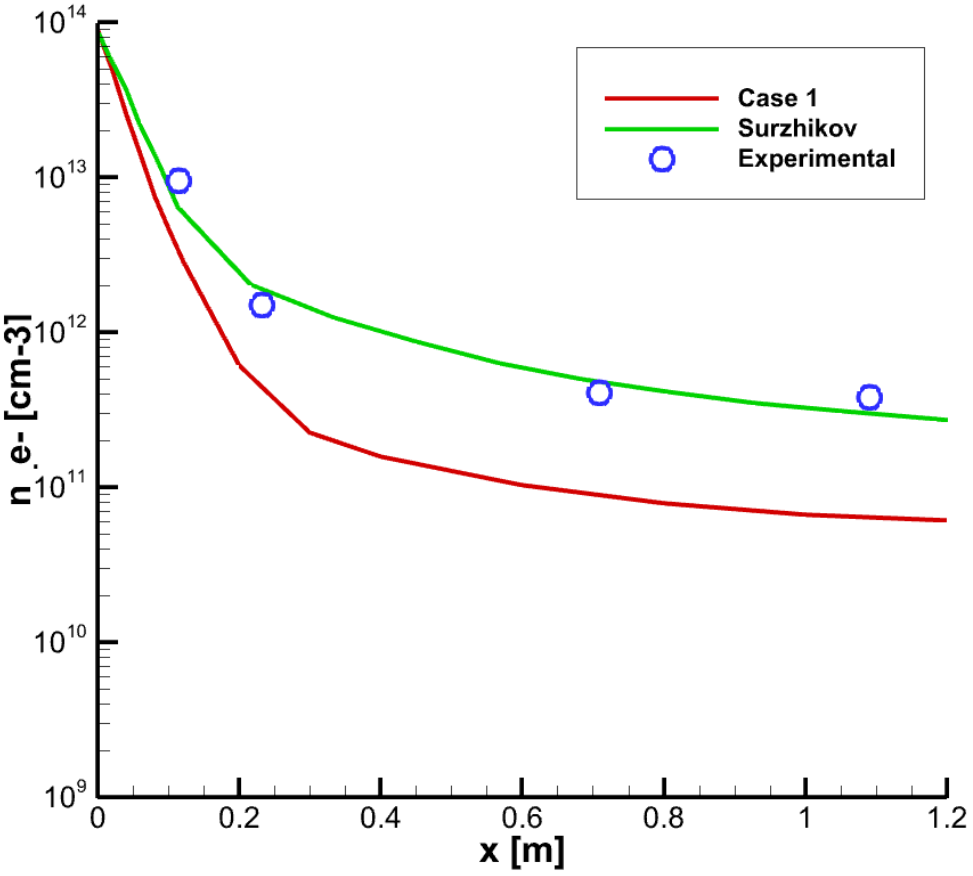

Figure 5.12. Case 1: maximum electron number density along the generatrix at 61 km.

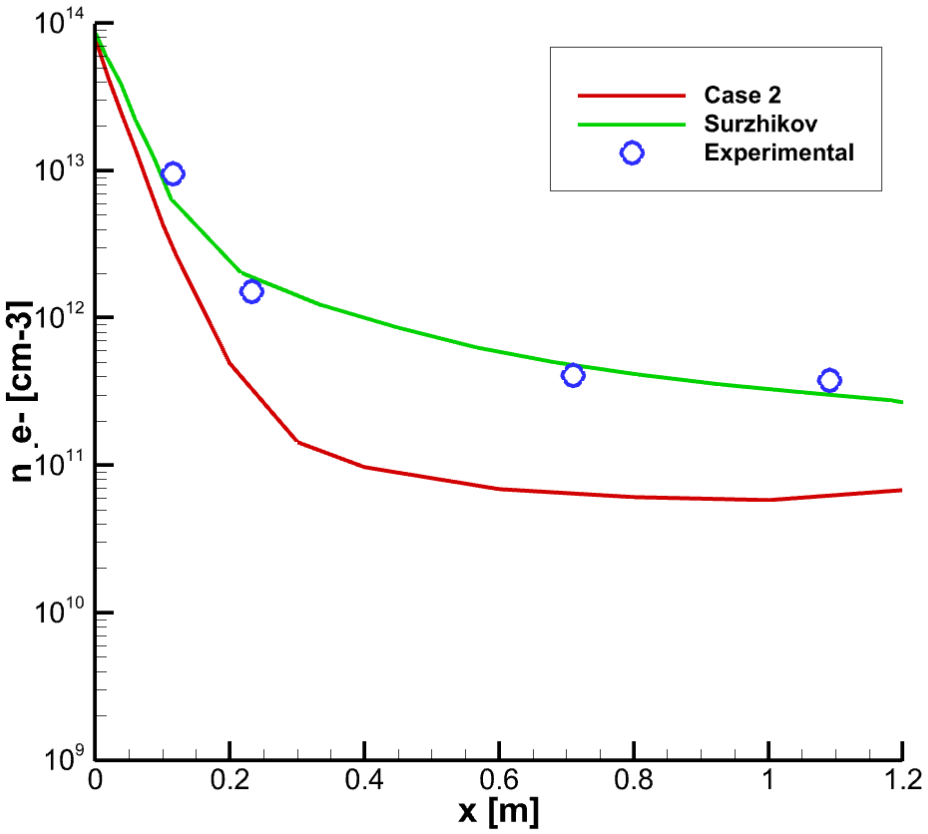

Figure 5.13. Case 2: maximum electron number density along the generatrix at 61 km.

Despite the different wall chemistry, kinetic model or wall temperature, the present solution reproduces, in both cases, Surzhikov's reference data with good accuracy. In particular, the numerical results capture:

- the correct value of the peak electron number density;
- the location and width of the region of peak ionization along the forebody;
- the decay of $n_{e,\max}$ towards the nose.

In addition to the scalar quantity $n_{e,\max}(x)$, it is instructive to compare the full electron concentration profiles with Surzhikov's reference solution to elucidate the sources of the discrepancies observed in the flow field downstream of the RAMCII nose. In Surzhikov's computations, the electron and ion fluxes at the surface are closed by imposing total recombination of charged species at the wall, which enforces a complete balance between diffusive fluxes and surface recombination and leads to a stronger depletion of n_e in the immediate vicinity of the wall [57].

In the present simulations, an equivalent forced recombination boundary condition for ions could not be prescribed in a fully consistent way, so the effective wall recombination rate is not constrained to match Surzhikov's assumption.

To show the effect on electron number density of the absence of wall recombination, in the figures below are reported the direct comparison between the cases and Surzhikov's data for the electron number density profiles at selected axial stations.

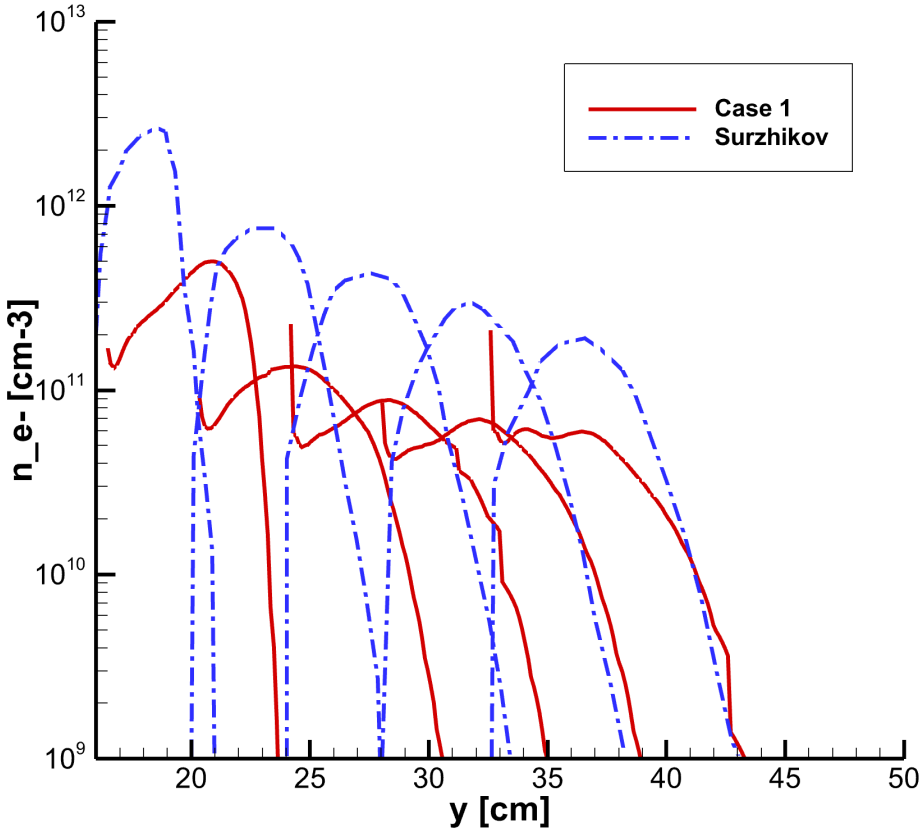

Figure 5.14. Case 1: electron number density profiles at selected axial stations (x_1 = 21.4cm, x_2 = 46cm, x_3 = 71.2cm, x_4 = 95.3cm, x_5 = 125cm) compared with Surzhikov's reference data.

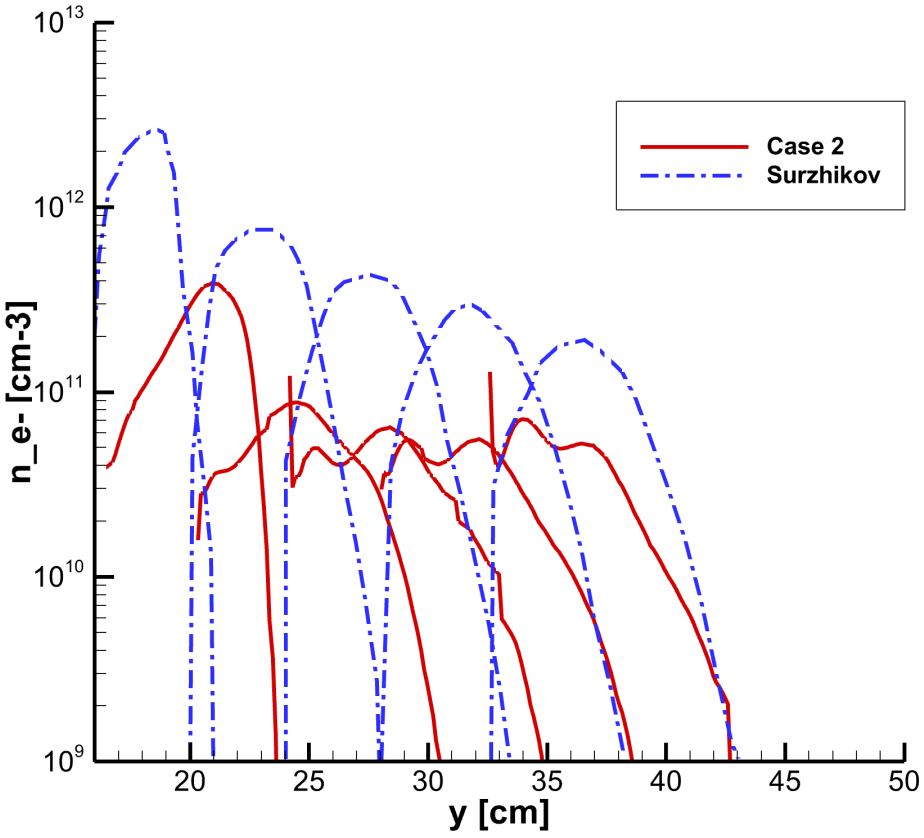

Figure 5.15. Case 2: electron number density profiles at selected axial stations (x_1 = 21.4cm, x_2 = 46cm, x_3 = 71.2cm, x_4 = 95.3cm, x_5 = 125cm) compared with Surzhikov's reference data.

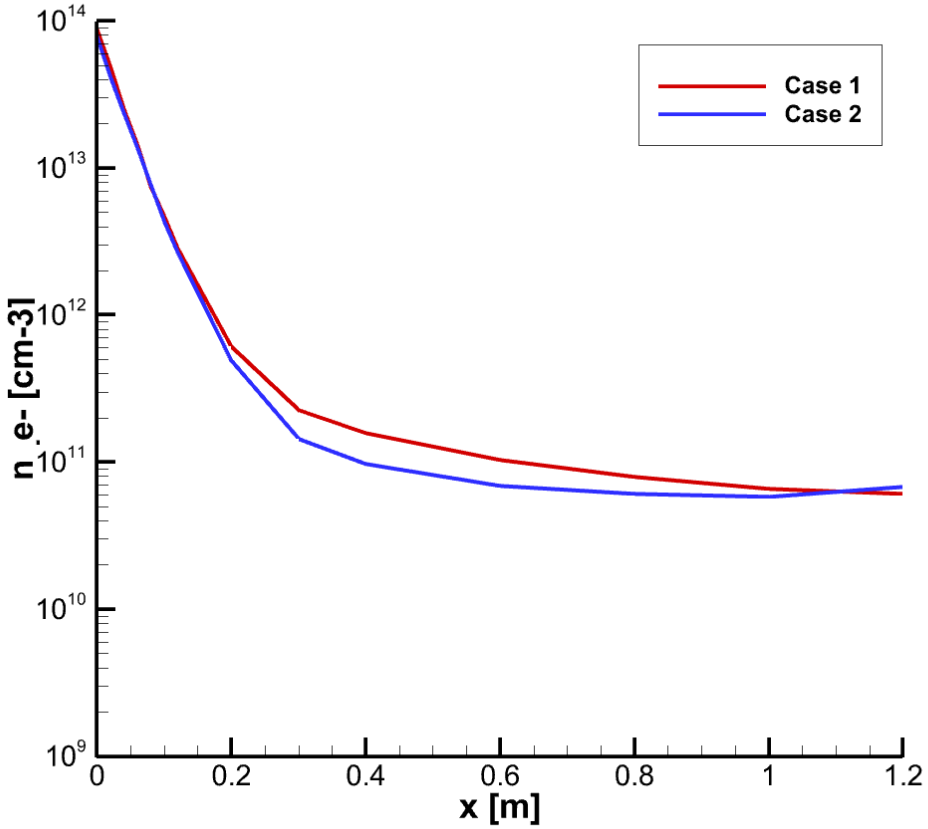

Figure 5.16. Comparison of maximum electron number density along the generatrix between Case 1 and Case 2.

About wall temperature effects, the main observations are:

- the overall shape of the $n_{e,\max}$ distribution is nearly unchanged when increasing T_w from 550 K to 1000 K;
- the relative variation of the peak value of $n_{e,\max}$ remains within the 10-15% range reported by Surzhikov as the typical sensitivity to thermal and catalytic boundary condition uncertainties;
- the bow shock and the high temperature core of the ionized layer remain essentially controlled by the freestream enthalpy, not by the wall conditions.

5.5.3 Stagnation Line Temperature Profiles and Shock Standoff

The analysis of the thermal structure along the stagnation streamline provides critical insight into the shock capturing capabilities of the solver and the thermochemical state of the post-shock gas.

Figure 5.17 and figure 5.18 compares the temperature profiles along the stagnation line for Case 1 and Case 2.

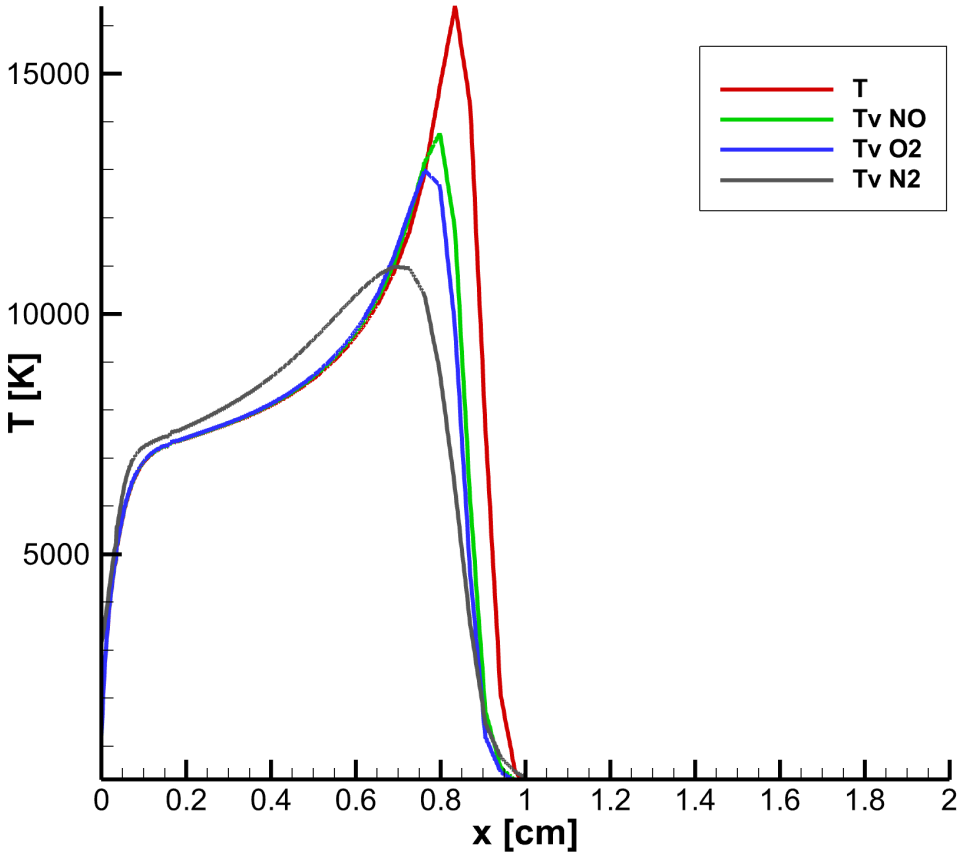

Figure 5.17. Temperature profiles along the stagnation line for Case 1.

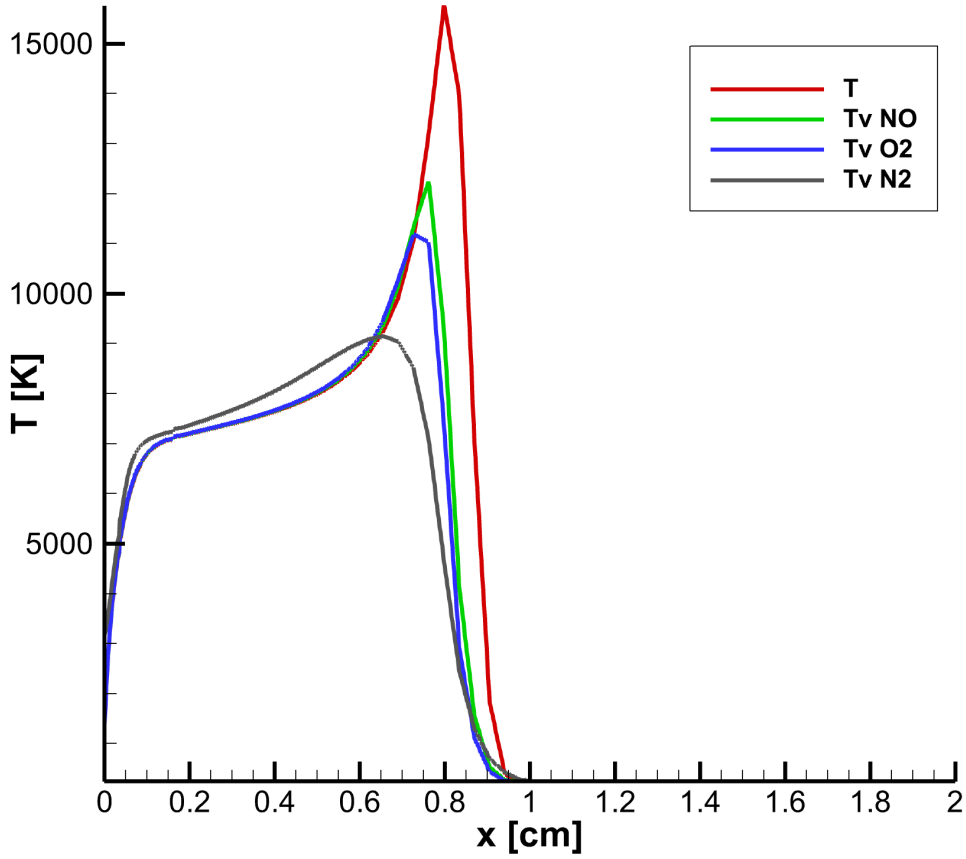

Figure 5.18. Temperature profiles along the stagnation line for Case 2.

In the next figures, both cases are compared with Surzhikov's reference data and experimental data [2, 22, 29], focusing on two key aspects: the shock standoff distance and the peak temperature behavior in the shock layer.

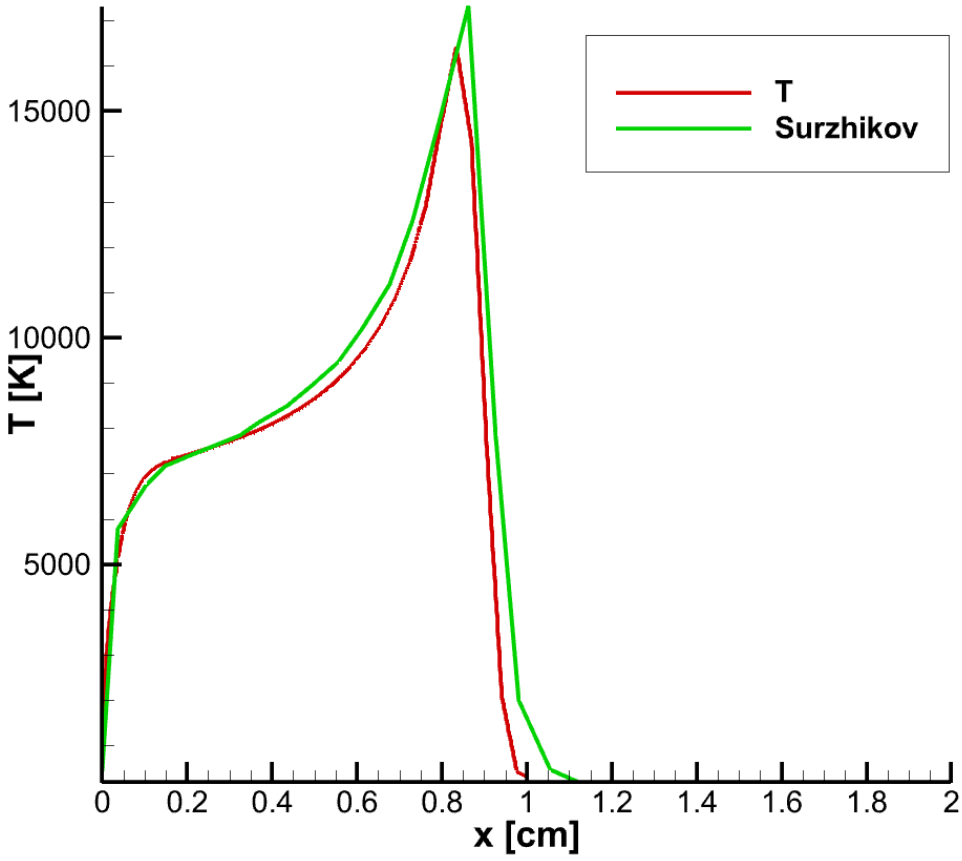

Figure 5.19. Comparison of stagnation line translational temperature profiles between Case 1 and Surzhikov's reference data.

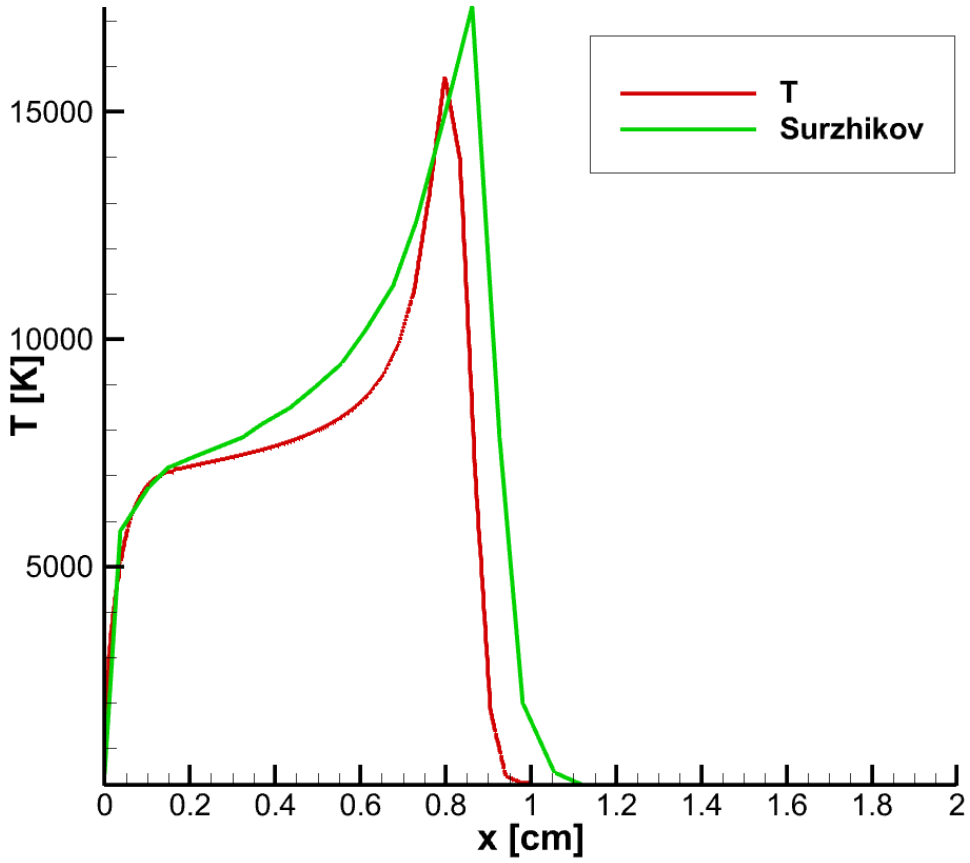

Figure 5.20. Comparison of stagnation line translational temperature profiles between Case 2 and Surzhikov's reference data.

Shock Standoff Distance

The shock standoff distance (Δ_{sh}), defined as the distance between the vehicle nose and the location of the maximum temperature gradient, is a primary validation metric for the fluid dynamic setup.

In both simulated cases, the computed shock standoff distance is approximately $\Delta_{sh} \approx 1$ cm. This value is consistent between the two kinetic models and shows excellent agreement with the numerical results reported by Surzhikov [57] for the same flight condition ($H = 61$ km, $M_\infty = 23.9$). The consistency of Δ_{sh} confirms that the grid resolution in the shock layer is adequate and that the bulk density ratio across the shock is correctly predicted regardless of the specific finite rate chemistry details.

Peak Temperature and Chemical Cooling

Both cases exhibit a sharp temperature rise across the bow shock, reaching a peak translational temperature characteristic of the frozen Rankine-Hugoniot conditions, followed by a relaxation region where energy is transferred to internal modes and consumed by endothermic chemical reactions.

A slight discrepancy in the peak and post-shock temperature profile is observed between the two cases. Specifically, the simulation employing the 20 reaction Park model (Case 2) predicts a marginally lower temperature in the non equilibrium relaxation zone compared to the 18 reaction baseline (Case 1).

This thermal behavior can be physically attributed to the extended reaction mechanism. The 20 reactions model includes additional dissociation channels involving ionic collision partners. These dissociation processes are strongly endothermic; by activating further pathways for molecular breakdown, they effectively act as an additional energy sink, absorbing a larger fraction of the flow enthalpy. Consequently, this enhanced chemical activity leads to a faster depletion of the translational energy pool, resulting in the observed reduction in local temperature compared to the simplified 18 reaction scheme.

Overall, both models correctly capture the strong thermal non equilibrium immediately behind the shock and the subsequent thermalization towards the boundary layer.

5.6 Summary and Remarks

The validation study for the RAM-C II forebody at 61 km leads to the following conclusions:

- The CAD reconstruction and the structured, body-fitted mesh provide a reliable representation of the forebody flow. The deliberate truncation of the afterbody and the omission of the wake significantly reduce computational cost without affecting the bow-shock structure or the peak ionization levels, which are confined to the forebody region.
- The solver, with a two temperature Park 20 reactions chemistry model and a fully non-catalytic wall, reproduces the maximum electron number density along the generatrix in good agreement with Surzhikov's reference data.
- The absence of explicit electron recombination at the wall is conservative for black-out assessment and has only a minor impact on the shock-layer peak electron density, which is the primary validation metric.
- The sensitivity analysis with $T_w = 1000$ K confirms that the solution for $n_{e,\max}$ is relatively insensitive to the wall temperature at 61 km, with peak variations within 10-15%, consistent with literature [57].

Overall, the comparison supports the suitability of the NSA code for predicting the ionization and electron concentration around hypersonic reentry vehicles in regimes similar to RAM-C II.

Chapter 6

Conclusions and Future Developments

This thesis work was conducted in the framework of a collaboration with Thales Alenia Space - Italia, with the primary objective of restoring, optimizing, and validating a proprietary Computational Fluid Dynamics (CFD) code for hypersonic applications. The activity addressed both the software architecture challenges, modernizing a legacy FORTRAN codebase, and the physical modeling requirements typical of high enthalpy re-entry flows.

6.1 Summary of the Work

The project was structured into three main phases:

1. **Code restoration and modernization:** the initial effort focused on recovering full functionality of the existing solver, resolving legacy compatibility issues and ensuring robust operation on modern architectures for both 2D axisymmetric and 3D geometries.

2. **Implementation:** a significant portion of the work was dedicated to enhancing computational efficiency. The solver was successfully parallelized using the Message Passing Interface (MPI) standard on Windows, enabling scalable execution on multi-core processors. This step was crucial to make the complex non equilibrium chemistry simulations computationally feasible within industrial turnaround times.

3. **Physical validation:** the modernized tool was then subjected to a targeted validation campaign using the RAM-C II flight experiment as a benchmark, specifically focusing on the prediction of thermochemical non equilibrium and plasma formation.

6.2 Key Achievements

The analysis yielded significant results on both the computational and physical fronts:

Computational Performance

The porting and parallelization of the code were successful. The solver demonstrated the capability to handle grids in a parallel environment, providing a stable platform for computationally intensive hypersonic simulations.

Aerothermodynamic Capabilities

Despite the complexity of the physics involved, the validation at the 61 km trajectory point confirmed the reliability of the implemented physical models:

- The solver correctly captures the macroscopic shock layer topology (shock standoff distance ≈ 1 cm) and the strong thermal gradients.
- The integration of finite-rate chemistry (Park 18 and 20 reactions models) allowed for an accurate prediction of the peak electron number density, a critical parameter for radio-blackout assessment.
- The sensitivity analysis confirmed the robustness of the solution against variations in wall temperature and kinetic schemes, providing confidence in the code's predictive maturity for preliminary design phases.

6.3 Limitations and Future Perspectives

The validation campaign, while successful for the identified metrics, was necessarily limited in scope due to the time constraints of the project. Furthermore, the current implementation of the wall boundary conditions adopted a conservative non-catalytic approach for plasma species.

Future developments of this tool should prioritize:

- **Extended validation:** expanding the validation matrix to include different flight regimes and more complex 3D geometries to fully stress-test the parallel architecture.
- **Enhanced chemistry models:** incorporating more sophisticated reaction mechanisms and transport properties to improve fidelity in high-enthalpy regimes
- **3D solver optimization:** while the parallelization has proven effective for standard cases, preliminary tests on complex 3D geometries have highlighted performance bottlenecks. Future work should focus on optimizing the 3D memory management and linear system solution algorithms to further reduce computational time and improve scalability for large-scale industrial configurations.

- **Full feature exploitation:** conducting a thorough testing campaign on the auxiliary physical models and boundary condition options already present in the codebase but not fully exercised during this work, ensuring their robustness for operational use.
- **Physics modules integration:** coupling the current fluid solver with material response codes (ablation) and radiation transport solvers to enable comprehensive multiphysics re-entry analysis.

In conclusion, the work accomplished in this thesis has delivered a modernized, parallelized, and physically validated CFD tool. The code now stands as a solid and efficient foundation for future research in hypersonic aerothermodynamics and for industrial applications within Thales Alenia Space.

Bibliography

[1] European Space Agency (ESA). *Intermediate eXperimental Vehicle for Reentry Technologies*. Tech. rep. European Space Agency, 2015. URL: https://www.esa.int/Enabling_Support/Space_Transportation/IXV.

[2] Norman D. Akey and Aubrey E. Cross. *Radio blackout alleviation and plasma diagnostic results from a 25,000 foot per second blunt-body reentry*. TN D-6861. National Aeronautics and Space Administration, 1970. URL: https://ntrs.nasa.gov/api/citations/19700008892/downloads/19700008892.pdf.

[3] John D. Anderson. *Computational Fluid Dynamics: The Basics with Applications*. New York: McGraw-Hill, Inc., 1995. ISBN: 0-07-001685-2.

[4] John D. Anderson. *Hypersonic and High-Temperature Gas Dynamics*. 2nd. Reston, Virginia: American Institute of Aeronautics and Astronautics, Inc., 2006. ISBN: 1-56347-609-8.

[5] R. Byron Bird. "Transport phenomena". In: *Applied Mechanics Reviews* 55.1 (2002).

[6] Graham V. Candler and Robert W. MacCormack. "Computation of Weakly Ionized Hypersonic Flows in Thermochemical Nonequilibrium". In: *Journal of Thermophysics and Heat Transfer* 5.3 (1991), pp. 266–273. DOI: 10.2514/3.260.

[7] Sydney Chapman and T. G. Cowling. *The Mathematical Theory of Non-Uniform Gases*. Third. Cambridge University Press, 1970. ISBN: 9780521408448.

[8] Richard Courant, Kurt Friedrichs, and Hans Lewy. "On the partial difference equations of mathematical physics". In: *IBM journal of Research and Development* 11.2 (1967), pp. 215–234. DOI: 10.1147/rd.112.0215.

[9] Domenic D'Ambrosio. *Aerotermodinamica ipersonica*. Appunti delle lezioni, Politecnico di Torino. 2024.

[10] Domenic D'Ambrosio. *Fluidodinamica Computazionale*. Appunti delle lezioni, Politecnico di Torino. 2023.

[11] John T. Daniels. *First Flight of the Wright Flyer with Orville Wright at the Controls*. Dec. 1903. URL: https://hdl.loc.gov/loc.pnp/ppprs.00626.

[12] Cornelius J. Dennehy et al. *A Comprehensive Analysis of the X-15 Flight 3-65 Accident*. Technical Memorandum NASA/TM-2014-218538. National Aeronautics and Space Administration, 2014. URL: https://ntrs.nasa.gov/api/citations/20140013264/downloads/20140013264.pdf.

[13] A. A. Dorodnitsyn. “Boundary Layer in a Compressible Gas”. In: *Prikladnaya Matematika i Mekhanika* 6.6 (1942), pp. 449–486.

[14] M. G. Dunn and S. W. Kang. *Theoretical and Experimental Studies of Reentry Plasmas*. CR Report 2232. National Aeronautics and Space Administration, 1973. URL: https://ntrs.nasa.gov/api/citations/19730013358/downloads/19730013358.pdf.

[15] E. R. G. Eckert. “Engineering Relations for Heat Transfer and Friction in High-Velocity Laminar and Turbulent Boundary-Layer Flow Over Surfaces With Constant Pressure and Temperature”. In: *Transactions of the ASME* 78.6 (Aug. 1956), pp. 1273–1283. DOI: 10.1115/1.4014011.

[16] B. Edney. *Anomalous Heat Transfer and Pressure Distributions on Blunt Bodies at Hypersonic Speeds in the Presence of an Impinging Shock*. FFA Report 115. Flygtekniska Försöksanstalten, 1968.

[17] Arnold Eucken. “Über das Wärmeleitvermögen, die spezifische Wärme und die innere Reibung der Gase”. In: *Physikalische Zeitschrift* 14 (1913), pp. 324–332.

[18] European Space Agency (ESA). *IXV Mission Image Gallery*. https://www.esa.int/ESA_Multimedia/Missions/IXV/(sortBy)/votes/(result_type)/images. Accessed: 2025-11-16.

[19] James A. Fay and Frank R. Riddell. “Theory of Stagnation Point Heat Transfer in Dissociated Air”. In: *Journal of the Aeronautical Sciences* 25.2 (1958), pp. 73–85. DOI: 10.2514/8.7517.

[20] Sergei Konstantinovich Godunov. “A difference scheme for numerical solution of discontinuous solution of hydrodynamic equations”. In: *Math. Sbornik* 47 (1959), pp. 271–306.

[21] R. Goulard. “The Coupling of Radiation and Convection in Detached Shock Layers”. In: *Journal of Quantitative Spectroscopy and Radiative Transfer* 1 (1961), pp. 249–257. DOI: 10.1016/0022-4073(61)90025-5.

[22] William L Grantham. *Flight results of a 25000-foot-per-second reentry experiment using microwave reflectometers to measure plasma electron density and standoff distance*. Vol. 6062. TN D-6862. National Aeronautics and Space Administration, 1970. URL: https://ntrs.nasa.gov/api/citations/19710004000/downloads/19710004000.pdf.

[23] R. N. Gupta et al. “A Review of Reaction Rates and Thermodynamic and Transport Properties for an 11-Species Air Model for Chemical and Thermal Nonequilibrium Calculations to 30000 K”. In: *NASA Reference Publication* 1232 (1990). URL: https://ntrs.nasa.gov/api/citations/19900017748/downloads/19900017748.pdf.

[24] R. N. Gupta et al. “Calculations and Curve Fits of Thermodynamic and Transport Properties for Equilibrium Air to 30000 K”. In: *NASA Reference Publication* 1260 (1991). URL: https://ntrs.nasa.gov/api/citations/19920002067/downloads/19920002067.pdf.

[25] Florian Haider, J-P Croisille, and Bernard Courbet. “Stability analysis of the cell centered finite-volume MUSCL method on unstructured grids”. In: *Numerische Mathematik* 113.4 (2009), pp. 555–600.

[26] Amiram Harten, Peter D Lax, and Bram van Leer. “On upstream differencing and Godunov-type schemes for hyperbolic conservation laws”. In: *SIAM review* 25.1 (1983), pp. 35–61. DOI: 10.1137/1025002.

[27] H Hugoniot. “Mémoire sur la propagation du mouvement dans un fluide indéfini (premiere partie)”. In: *Journal de Mathématiques Pures et Appliquées* 3 (1887), pp. 477–492.

[28] Intel. *Porting Guide for ifort Users to ifx*. URL: https://www.intel.com/content/www/us/en/developer/articles/guide/porting-guide-for-ifort-to-ifx.html.

[29] W. Linwood Jones and Aubrey E. Cross. *Electrostatic-probe measurements of plasma parameters for two reentry flight experiments at 25000 feet per second*. Vol. 6617. TN D-7261. National Aeronautics and Space Administration, 1972. URL: https://ntrs.nasa.gov/api/citations/19720011555/downloads/19720011555.pdf.

[30] George Karypis, Kirk Schloegel, and Vipin Kumar. *METIS 5.1.0: Serial Graph Partitioning and Sparse Matrix Ordering*. 2013. URL: http://glaros.dtc.umn.edu/gkhome/metis/metis/overview.

[31] Gustav Kirchhoff. “Ueber den Zusammenhang zwischen dem Emksionsoerrnogen und dern Absorptiorisoermcigen der Korper fir W´arme und Licht”. In: *Monatsberichte der Königlichen Preussischen Akademie der Wissenschaften zu Berlin* (1860), pp. 783–787.

[32] Lester Lees. “Laminar Heat Transfer over Blunt-Nosed Bodies at Hypersonic Flight Speeds”. In: *Jet Propulsion* 26.4 (1956), pp. 259–269. DOI: 10.2514/8.6977.

[33] Randall J. LeVeque. *Finite Volume Methods for Hyperbolic Problems*. Cambridge Texts in Applied Mathematics 31. Cambridge University Press, 2002. ISBN: 978-0-521-88094-6. DOI: 10.1017/CBO9780511791253.

[34] James Clerk Maxwell. “IV. On the dynamical theory of gases”. In: *Philosophical transactions of the Royal Society of London* 157 (1867). Maxwell developed this for gas diffusion; Stefan independently derived equivalent equations for liquids in 1871; the combined model is now called the Stefan-Maxwell equation, pp. 49–88. DOI: 10.1098/rstl.1867.0004.

[35] Microsoft. *Microsoft MPI (MS-MPI)*. URL: https://learn.microsoft.com/en-us/message-passing-interface/microsoft-mpi.

[36] R. C. Millikan and D. R. White. “Systematics of Vibrational Relaxation”. In: *The Journal of Chemical Physics* 28.3 (1963), pp. 542–546. DOI: 10.1063/1.1734182.

[37] Michael F. Modest. *Radiative Heat Transfer*. Third. Academic Press, 2013. ISBN: 978-0-12-386944-9. DOI: 10.1016/C2010-0-65874-3.

[38] Mos.ru. *Gagarin April 1961*. Wikimedia Commons. Apr. 1961. URL: https://commons.wikimedia.org/wiki/File:Gagarin_April_1961.jpg.

[39] NASA. *Apollo 11 Command Module being lowered to the deck of the U.S.S. Hornet*. NASA Image ID: S69-21294. July 1969. URL: https://images.nasa.gov/details/S69-21294.

[40] NASA. *Bumper WAC Rocket Second Stage*. Wikimedia Commons. Feb. 1949. URL: https://commons.wikimedia.org/wiki/File:Bumper.jpg.

[41] NASA. *Space Shuttle Discovery landing after its first mission on STS-41D*. https://www.nasa.gov/wp-content/uploads/2019/08/sts_41d_landing_41d-03299.jpg. Public domain NASA image. Sept. 1984. URL: https://www.nasa.gov/wp-content/uploads/2019/08/sts_41d_landing_41d-03299.jpg.

[42] NASA Dryden Flight Research Center. *North American X-15*. Wikimedia Commons. 1960. URL: https://commons.wikimedia.org/wiki/File:North_American_X-15.jpg.

[43] Klaus Oswatitsch. *Gas Dynamics*. Trans. by Gustav Kuerti. New York: Academic Press, 1956, p. 610.

[44] Chul Park. *Assessment of Two-Temperature Kinetic Model for Ionizing Air*. Technical Memorandum 102081. National Aeronautics and Space Administration, 1989. DOI: 10.2514/3.28771.

[45] Chul Park. "On convergence of computation of chemically reacting flows". In: *23rd Aerospace Sciences Meeting*. 1985, p. 247. DOI: 10.2514/6.1985-247.

[46] Chul Park. "Review of Chemical Kinetic Problems of Future NASA Missions". In: *Journal of Thermophysics and Heat Transfer* 7.3 (1993), pp. 385–398. DOI: 10.2514/3.431.

[47] Chul Park, Richard L Jaffe, and Harry Partridge. "Chemical-kinetic parameters of hyperbolic earth entry". In: *Journal of Thermophysics and Heat transfer* 15.1 (2001), pp. 76–90. DOI: 10.2514/2.6582.

[48] Max Planck. "On the Law of the Energy Distribution in the Normal Spectrum". Trans. by Yu V. Kuyanov. In: *Verhandlungen der Deutschen Physikalischen Gesellschaft* 2 (1900), pp. 237–245.

[49] Ludwig Prandtl. "Über Flüssigkeitsbewegung bei sehr kleiner Reibung". In: *Verhandlungen des Internationalen Mathematiker-Kongresses* III (1904), pp. 484–491.

[50] William John Macquorn Rankine. "XV. On the thermodynamic theory of waves of finite longitudinal disturbance". In: *Philosophical Transactions of the Royal Society of London* 160 (1870), pp. 277–288. DOI: 10.1098/rstl.1870.0015.

[51] Philip L Roe. "Approximate Riemann solvers, parameter vectors, and difference schemes". In: *Journal of computational physics* 43.2 (1981), pp. 357–372. DOI: 10.1016/0021-9991(81)90128-5.

[52] Hermann Schlichting and Klaus Gersten. *Boundary-Layer Theory*. Ninth. Springer-Verlag, 2016. ISBN: 978-3-662-52917-1. DOI: 10.1007/978-3-662-52919-5.

[53] Robert Siegel and John R. Howell. *Thermal Radiation Heat Transfer*. Third. Hemisphere Publishing Corporation, 1992.

[54] Philippe Spalart and Steven Allmaras. "A one-equation turbulence model for aerodynamic flows". In: *30th aerospace sciences meeting and exhibit*. 1992, p. 439. DOI: 10.2514/6.1992-439.

[55] S. Srinivasan, J. C. Tannehill, and K. J. Weilmuenster. *Simplified Curve Fits for the Thermodynamic Properties of Equilibrium Air*. Reference Publication 1181. National Aeronautics and Space Administration, 1987. URL: https://ntrs.nasa.gov/api/citations/19870016876/downloads/19870016876.pdf.

[56] Haoyu Sun et al. "Backward scattering characteristics of a reentry vehicle enveloped by a hypersonic flow field". In: *International Journal of Antennas and Propagation* 2018.1 (2018), p. 5478580. DOI: 10.1155/2018/5478580.

[57] S. T. Surzhikov. "Two-Dimensional Numerical Analysis of Flow Ionization in the RAM-C-II Flight Experiment". In: *Russian Journal of Physical Chemistry B* 9.1 (2015), pp. 69–86. ISSN: 1990-7931. DOI: 10.1134/S1990793115010200.

[58] William Sutherland. "The Viscosity of Gases and Molecular Force". In: *Philosophical Magazine and Journal of Science* 36.223 (1893), pp. 507–531. DOI: 10.1080/14786449308620508.

[59] Eleuterio F Toro, Michael Spruce, and William Speares. "Restoration of the contact surface in the HLL-Riemann solver". In: *Shock Waves* 4.1 (1994), pp. 25–34. DOI: 10.1007/BF01414629.

[60] Eleuterio F. Toro. *Riemann Solvers and Numerical Methods for Fluid Dynamics: A Practical Introduction*. Third. Springer-Verlag, 2009. ISBN: 978-3-540-25202-3. DOI: 10.1007/b79761.

[61] C. E. Treanor, J. W. Rich, and R. G. Rehm. "Vibrational Relaxation of Anharmonic Oscillators with Exchange-Dominated Collisions". In: *The Journal of Chemical Physics* 48.4 (1968), pp. 1798–1807. DOI: 10.1063/1.1668914.

[62] Bram Van Leer. "Towards the ultimate conservative difference scheme. V. A second-order sequel to Godunov's method". In: *Journal of computational Physics* 32.1 (1979), pp. 101–136. DOI: 10.1016/0021-9991(79)90145-1.

[63] Walter G. Vincenti and Charles H. Kruger Jr. *Introduction to Physical Gas Dynamics*. Krieger Publishing Company, 1975. ISBN: 978-0-88275-208-2.

[64] Frank M. White and Joseph Majdalani. *Viscous Fluid Flow*. Fourth. McGraw-Hill, 2017. ISBN: 9781260597806.

[65] Charles R. Wilke. "A viscosity equation for gas mixtures". In: *Journal of Chemical physics* 18.4 (1950), pp. 517–519. DOI: 10.1063/1.1747673.

[66] Michael J Wright, Helen H Hwang, and David W Schwenke. "Recommended collision integrals for transport property computations part II: Mars and Venus entries". In: *AIAA journal* 45.1 (2007), pp. 281–288. DOI: 10.2514/1.24523.

[67] Kun Xu and Zuowu Li. "Dissipative mechanism in Godunov-type schemes". In: *International Journal for Numerical Methods in Fluids* 37.1 (2001), pp. 1–22. DOI: 10.1002/fld.160.

[68] H.C Yee, R.F Warming, and A Harten. "Implicit total variation diminishing (TVD) schemes for steady-state calculations". In: *Journal of Computational Physics* 57.3 (1985), pp. 327–360. ISSN: 0021-9991. DOI: 10.1016/0021-9991(85)90183-4.

[69] Y. B. Zeldovich and Y. P. Raizer. "Physics of Shock Waves and High-Temperature Hydrodynamic Phenomena". In: (2002).